Design and Implementation of an Electromagnetic Energy Harvester for Linear and Rotary Motion Applications

by

Alireza Hekmati

B.Sc. (Electrical Engineering), Iran University of Science and Technology, 2009

Thesis Submitted In Partial Fulfillment of the
Requirements for the Degree of
Master of Applied Science

in the
School of Engineering Science
Faculty of Applied Sciences

SIMON FRASER UNIVERSITY

Spring 2013

Approval

Name: **Alireza Hekmati**

Degree: **Master of Applied Science**

Title of Thesis: ***Design and Implementation of an Electromagnetic Energy Harvester for Linear and Rotary Motion Applications***

Examining Committee:

Chair: Dr. Krishna Vijayaraghavan
Assistant Professor of Engineering Science

Dr. Siamak Arzanpour
Senior Supervisor
Assistant Professor

Dr. Carlo Menon
Supervisor
Associate Professor

Dr. Woo Soo Kim
Internal Examiner
Assistant Professor
School of Engineering Science

Date Defended/Approved: 12 December 2013

Partial Copyright Licence

Abstract

This thesis presents a new design for an electromagnetic energy harvester to be used in both linear and rotary motion applications. This electromagnetic energy harvester consists of a moving coil within a fixed magnetic circuit. This magnetic circuit comprises of a permanent magnet (as a magnetic source), a magnetic conductor (such as iron), and an air gap to create a space for coil movement inside energy harvester setup. In the parameter study of this electromagnetic energy harvester, it has been demonstrated that applying design modifications will improve the amount of induced voltage by %50. For linear motion applications, the energy harvester has been mounted on a linear motor and the experimental results indicated that when the coil movements' speed is 70 [mm/s], the maximum harvested power is 5.320 [mW].

For rotary motion applications, first a voice coil speaker has been used as a single degree of freedom system to produce voltage through a rotating beam and hub. Since in lower resonance frequencies, the maximum induced voltage is quite low, thus in next step, the two degrees of freedom energy harvesting system for rotary motion applications has been introduced. This system has been mounted on a car ring and the result illustrated that at the resonance frequency (15 [Hz]), the induced voltage was 0.175 [V] for each coil.

Keywords: Electromagnetic energy harvester; Linear motion; Rotary motion; Permanent magnet; Magnetic conductor

Dedication

I dedicate my thesis to my lovely family, specially my mother, who her support and kindness through all the stages of my life made my goals so much easier to achieve.

Acknowledgements

I would like to thank my supervisor, Dr. Arzanpour, for his great support, useful guidance, and excellent understanding during my graduate study, which made this part of my lifetime so much effective and beneficial. His encouragements helped me a lot through my difficult times during my research. I would also like to thank Dr. Menon and Dr. Kim for kindly reviewing my thesis.

Also, I would like to thank Ehsan Asadi, my colleague and my friend, who has helped me so much during diverse stages of my research and aided me to overcome the obstacles in my research progress more easily.

Finally, I would like to thank all of my friends, specially Ehsan Seyedin, who has always been there for me and supported me through my difficult times.

Table of Contents

List of Tables

List of Figures

1. Introduction

Energy harvesting refers to all the methods which enable us to convert diverse forms of kinetic energy into the storable form of electrical energy to power a standalone sensor and/or actuator system. Energy harvesting is an attractive research subject as inexhaustible replacements for batteries in low-power devices to convert ambient energy into electrical energy and have received growing research interest in recent years.

Ambient energy is the energy which is available in the environment and is not stored explicitly [1]. The most common used ambient energy sources to harvest are essentially of three forms: light (solar power), thermal gradient, and mechanical energy from movement and vibration (motion) [1]–[3]. These sources can be used as either a direct replacement or to augment the battery to increase both the lifetime and capability of the network [4]-[6]. There are other alternative solutions such as micro fuel cells [7] and micro turbine generators [8]. Although these two sources both involve the use of chemical energy and require refuelling when their supplies are exhausted, but such systems are capable of producing high levels of energy and power density and demonstrate good potential to recharge batteries [9].

Solar power, which is used by photovoltaic, is probably the most well known amongst the other sources. The power density of solar cells in direct sunlight is excellent, but it is limited in dim ambient light conditions. Moreover, solar cells are clearly unsuitable in applications where the cells can be obscured by contamination, or simply where no light may be present.

Thermal energy is another source which can be directly converted to electrical energy through thermoelectric effect called the Seebeck effect. early thermoelectric microgenerators produced just a few nanowatts [10], however, the output power has been improved to around 1 microwatt when it is combined with micro-combustion chambers recently [11,12].

Kinetic energy is one of the sources that is typically present in the form of vibrations, rotations, random displacements, or forces. it can potentially be converted into electrical energy using various energy harvesting techniques, such as electromagnetic, piezoelectric, or electrostatic mechanisms.

Electrostatic energy harvesting relies on the relative movement between electrically isolated charged capacitor plates to generate energy based on the changing capacitance of vibration dependant variable capacitor [13]. If the voltage across the capacitor is constrained, charge will move from the capacitor as the capacitance decreases while if the charge on the capacitor is constrained, the voltage will increase as the capacitance decreases [14]. In both cases, mechanical energy is transformed into electrical energy. Generally the voltage constrained method offers more energy than the charge constrained approach, but by incorporating a parallel capacitor to the energy harvesting capacitor, the energy from the charge constrained system can approach that of the voltage constrained system as the parallel capacitance approaches infinity. This parallel capacitor constrains the voltage on the energy harvesting capacitor [15]. However, one of the disadvantages of this method is that it requires an additional voltage source or charge source, which can be a rechargeable battery or pre-charged capacitor, to initiate the conversion process. On the other hand, the significant advantage of using the electrostatic converter is its ability to integrate with microelectronics and it does not need any smart material.

Electrostatic generators can be classified into three types [16]:

1. In-plane overlap varying;
2. In-plane gap closing;
3. Out-of-plane gap closing.

Roundy [17] mentions that in-plane gap closing represents the highest power output with an optimized design harvesting 100 microwatts per cubic centimeter, while out-of-plane gap closing is the next highest followed by in-plane overlap varying.

To illustrate research works which have been conducted in these three types, Meninger *et al* [18] simulated an in-plane overlap varying electrostatic generator and generated 8 microwatts from 2.5 [kHz] input motion.

Despesse [19] describes an electrostatic in-plane gap closing structure with a charge constrained cycle. This device has an 18 cubic centimeters volume and produced 1052 microwatts scavenged power for a 90 micrometers vibration amplitude at 50 [Hz]. This amount of power represents a scavenged efficiency of 60% with the charge/discharge losses and transduction losses being accounted for.

Miyazaki [20] showed an out-of-plane cantilever based generator with a base capacitance of 1 [nF] and a variable capacitance of between 30 [pF] and 350 [pF]. The device resonated at 45 [Hz] and was tested on a wall with a 1 [μm] displacement up to 100 [Hz]. 120 [nW] was harvested from this configuration.

There are some other generator categories which employ charged electrets. Sterken [21,22] presents a concept of an in-plane, overlap varying, voltage constrained, variable capacitor polarized with a SiO2/Si3Ni4 electret; while Arakawa [23] demonstrates another in-plane, overlap varying, voltage constrained, variable capacitor polarized with a fluorocarbon polymer electret offering high dielectric strength. For a 1 [mm] displacement amplitude at 10 [Hz], a 20 mm $\times$ 20 mm $\times$ 2 mm device produces 6 [μW] at 200 [V] into an optimized external resistive load of 10^8 [Ω]. in another study, Peano [24] demonstrates an electret-based in-plane overlap varying surface micromachined structure numerically and illustrates that nonlinear behaviour of the converter is crucial in the generator optimization and has to be taken into account. 50 [μW] power is predicted from a 911 [Hz] vibration source moving 5 [μm], while the same device optimized with a linear model is expected to produce only 5.8 [μW] power.

Piezoelectric energy harvesting converts mechanical energy to electrical by straining a piezoelectric material [25]. When a piezoelectric material is placed under a mechanical stress, a charge separation will occur across the material and will produce voltage, which is proportional to the applied stress. Piezoelectric materials usually show anisotropic characteristics, hence material properties differ depending upon the force direction and orientation of the polarization and electrodes [26]. These piezoelectric materials are available in diverse forms, such as single crystal like quartz, piezoceramic like lead zirconate titanate or PZT, thin film like sputtered zinc oxide, screen printable thick-films based upon piezoceramic powders, and polymeric materials like polyvinylidenefluoride (PVDF) [27]-[29]. The advantage of using piezoelectric converter

is the direct generation of desired voltage since it does not need a separate voltage source and additional components. Moreover, these converters are simple and can be used in force and impact-coupled harvesting applications. Some disadvantages are that piezoelectric materials are brittle in nature and sometimes allow the leakage of charge. Thus the transduction efficiency is limited [30]. Another disadvantage is that the piezoelectric generator should vibrate at its resonant frequency in order to generate maximum power. The resonant frequency is related to elastic constant for the piezoelectric material, the mechanical mass and its shape [31]. However, these parameters cannot be changed after the system is built. Therefore, the piezoelectric generator can only generate the maximum power when the driving frequency is equal to the system's natural frequency.

The earliest example of a piezoelectric kinetic energy harvesting system extracts energy from impacts, therefore it is called an impact coupled device. Initial work demonstrates the feasibility of this approach by dropping a 5.5 [g] steel ball bearing from 20 [mm] onto a piezoelectric transducer [32]. The piezoelectric transducer consists of a 19 [mm] diameter, 0.25 [mm] thick piezoelectric ceramic bond to a bronze disc 0.25 [mm] thick with a diameter of 27 [mm]. This work determines that the optimum efficiency of the impact excitation approach is 9.4% into a resistive load of 10 [kΩ].

The piezoelectric generators have also been used to power human-wearable systems. Human motion is characterized by large amplitude movements at low frequencies. A device has been developed at the Massachusetts Institution of Technology (MIT) in the 1990s [33]. Researchers first mounted an 8 layer stack of PVDF laminated with electrodes either side of a 2 [mm] thick plastic sheet. This stave was used as an insole in a sports training shoe. At a frequency of 0.9 [Hz], this arrangement produced an average power of 1.3 [mW] into a 250 [kΩ] load.

A cantilever structure with piezoelectric material attached to the top and bottom surfaces is an attractive geometry for harvesting energy from vibrations, where these structures are designed to operate in a bending mode. A tapered cantilever beam was developed by Glynne- Jones *et al* [34]–[36]. For a given displacement, the tapered profile ensures a constant strain in the piezoelectric film along its length. The generator was fabricated by screen printing a piezoelectric material onto a 0.1 [mm] thick hardened

AISI 316 stainless steel. The piezoelectric material is based upon PZT-5H powder blended with Corning 7575 glass and a suitable thick-film vehicle to form a screen printable thixotropic paste [37]. The structure operated in its fundamental bending mode at a frequency of 80.1 [Hz] and produced up to 3 [μW] of power into an optimum resistive load of 333 [kΩ]. Recent advances in the film properties can also improve power output [38].

Another type of piezoelectric harvester is a MEMS cantilever device which has been presented by Jeon *et al* [39]. The cantilever was formed from a membrane made from layers of thermally grown silicon oxide, deposited silicon nitride and sol–gel deposited zirconium dioxide which acts as a buffer layer. The novelty of this work was mainly based on the use of a Ti/Pt electrode pattern e-beam evaporated and patterned on top of the PZT later. This generator was found to have a resonant frequency of 13.9 [kHz] at which it produced 1.01 [μW] at 14 [nm] base displacement.

At last, Sodano *et al* also compared macro-fibre composite (MFC) actuators with standard piezoceramics [40, 41]. The MFC structure was developed by NASA [42] and consists of thin PZT fibres embedded in a Kapton film. The MFC was found to supply too little current to charge batteries while the standard PZT piezoceramic was able to charge various capacity nickel metal hydride batteries.

Electromagnetic induction, first discovered by Faraday in 1831, involves the generation of electric current in a conductor located within a magnetic field. The conductor typically takes the form of a coil and the induced voltage is generated by either the relative motion of the magnet and coil, or because of changes in the magnetic field with time. In the former case, the amount of generated induced voltage depends upon the magnetic field intensity, the velocity of the relative motion and the length of the coil [43].Voice coils that are originally designed as loudspeakers are one of the candidates for this application. Unlike electrostatic mechanism, no separate voltage source is needed to get the conversion process started. Moreover, the system can be designed without mechanical contact between any parts, which can be lead to improve reliability and to reduce mechanical damping [44]. Even in the theory, this type of converter could be designed so that the value of mechanical damping is small.

Considering the drawbacks of both electrostatic and piezoelectric mechanisms, the electromagnetic converter has been examined in detail in this thesis.

The vibration sources can be found in diverse applications such as household goods (fridges, washing machines, microwave ovens etc.), industrial plant equipment, moving systems like automobiles and airplanes, and structures such as buildings and bridges [45], thus the advantage of using mechanical vibration to harvest energy is that this type is the most prevalent energy source available in many environments. The generated amount of energy by this approach depends upon the efficiency of the generator and the power conversion electronics and the quantity and form of the kinetic energy available in the environment. Amirtharajah and Chandrakasan [1] has described a self-powered Digital Signal Processing system, which powered by an electromagnetic generator. Their generator consists of a cylindrical housing in which a cylindrical mass is attached to a spring and fixed to one end. Moreover, a permanent magnet is attached to the other end of the housing and a coil attached to the mass, which is free to oscillate vertically within the housing. The resonant frequency of their design was 94 [Hz] and the maximum output voltage was 180 [mV]. The authors simulated the generator output in a human-powered application and predicted that an average of 400 [μW] could be generated from 2 [cm] movement at 2 [Hz].

Glynne-Jones *et al.* [46] has described a cantilever-based prototype with a four magnet and fixed coil arrangement with the overall volume of 3.15 [cm^3] and the resonant frequency of 106 [Hz]. At an acceleration level of 2.6 [$\frac{m}{s^2}$], the generator produced an output voltage of 1 [V]. The generator was mounted on the engine block of a car and the maximum peak power of 4 [mW] was produced, while the average power was 157 [μW] over a journey of 1.24 [km].

Von Buren and Troster [47] have described a linear electromagnetic generator, which is designed to be driven by human motion. The design consists of a tubular translator which contains a number of cylindrical magnets separated by spacers. The translator moves vertically within a series of stator coils. The stator and translator designs were realised with six magnets and five coils, with the total device volume of 30.4 [cm^3]. The fabricated prototype produced an average power output of 35 μW when

located just below a subject's knee. Williams and Yates [48] have developed a micro-electromagnetic converter. They drove this converter with vibration of 50 [μm] magnitude at 330 [Hz] and generated 1 [mW] power from it.Lastly, Hadas *et al.* [49] have developed an electromagnetic vibration powered generator, which is concerned with wireless aircraft-monitoring systems. The presented device is 45 [cm^3] in volume, resonates at 34.5 [Hz] and delivers around 3.5 [mW] from 3.1 [m/s^2] acceleration levels.

Note that there are other methods to harvest energy, such as using magnetostrictive materials which deform when placed in a magnetic field and conversely if strained can induce changes in a magnetic field. These materials can be used independently but typically have been employed in piezoelectric-magnetostrictive composites. Bayrashev *et al* fabricated a diameter of 0.5 [mm] thick PZT disc sandwiched between 1.5 [mm] thick Terfenol discs [50]. When the laminate is exposed to a low frequency varying magnetic field, the PZT layer was strained and a charge generated. Power output was found to be between 10 and 80 [μW] depending upon the distance between the magnet and the composite.

1.1. Thesis Objective and Thesis Outline

Rotary motion is one of the most commonly used forms of mechanical motion and power transmission widely used in various platforms in civil and industrial applications. Wireless communication is used in rotary devices as a reliable technique for sensory data acquisition, which does not have the drawbacks of wired systems such as the need for slip-rings. In those applications, a main problem is providing energy to power sensors and wireless modules. Although new technologies have considerably improved the size and power storage of batteries, they still need to be charged when used continuously. As a result, availability of a power scavenging unit will be a huge advantage in modern wireless systems. The main objective of this thesis is to develop a reliable electromagnetic energy harvester for rotary applications to locally generate the required power for the electronic systems.

chapter 2 illustrates the main governing theory of electromagnetic for electrical part of the energy harvester structure to get basic understanding of the design procedure.

The basic design concept of electromagnetic energy harvester for both linear and rotary motion applications is the same and is based on moving coil within a fixed magnet, where the moving coil cuts the magnetic flux density around the permanent magnet to induce voltage within it.

Basically, the generalized linear electromagnetic energy harvester is inspired by voice coil. The voice coils are originally designed for high frequency applications like laud speakers, and their usage for low frequency applications, like energy harvesting, have not been examined properly. Therefore, investigating the effects of changing some parameters in traditional voice coil structure, such as the length of the device or reshaping some parts of the device, is the main purpose of the third chapter of this thesis. The goal of chapter 3 is to provide a parameter study to improve the power efficiency of the electromagnetic linear harvesters.

Considering the same design concept as linear generator, another electromagnetic energy harvester has been developed and implemented for rotary motion applications. Chapter 4 discusses a rotary power scavenging unit comprised of a rotating flexible cantilever beam with a voice coil as the tip mass for energy harvesting. The gravitational force on the tip mass causes sustained oscillatory motion in the flexible beam as long as there is rotary motion. Note that in this one degree of freedom system and the resonance frequency occurs in relatively high frequencies, which are not achievable in many rotary applications, therefore it has been tried to reduce the resonance frequency of the system. But since in lower resonance frequencies, the maximum induced voltage has decreased dramatically, therefore in chapter 5, the two degrees of freedom energy harvesting system for rotary motion applications has been introduced. In chapter 5, after representing the mathematical modeling of the two degrees of freedom energy harvester system, based on the shaker test results, the characteristics of this generator have been described. Finally, this rotary energy harvester has been mounted on a car’s ring to demonstrate the its power generation capability in practice.

2. The main governing theory of Electromagnetic Generators

Kinetic energy harvesting requires a transduction mechanism to generate electrical energy from motion and the generator will require a mechanical system that couples environmental displacements to the transduction mechanism. Since in this thesis the electromagnetic mechanism has been chosen for generating electrical power, thus in this chapter, the governing equations of electromagnetic theory has been described.

The basic theory of an electromagnetic energy harvester is based on Faraday's law, which relates the electromotive force (ε) to the rate of change of flux linkage (ϕ) as [51],

$$\varepsilon = -\frac{\partial \phi}{\partial t} \qquad (1)$$

The negative sign in the Faraday's law is an assertion that the current induced by electromotive force (emf) will be in a direction to oppose the changes in the linking magnetic flux.

The electromotive force (emf) can be obtained from taking the line integral of electric field (*E*) over contour *C* [52];

$$\varepsilon = \oint_C \vec{E}.d\vec{l} \qquad (2)$$

and the flux linkage can be obtained from taking the surface integral of magnetic flux density (*B*) over surface *S* [53];

$$\phi = \int_S \vec{B}.\hat{n}ds \qquad (3)$$

On the other hand, when a conductor with a velocity of *u*, moves in a static magnetic field with a flux density of *B*, the magnetic force applied on conductor is [54],

$$F_m = qu \times B \qquad (4)$$

This force causes the electrons in the conductor to drift toward one end of the conductor and hence leave the other end charged positively. This separation of charges continues until equilibrium state is reached. At the equilibrium state, the net force on the charges in the moving conductor is equal to zero.

The magnetic force per unit charge can be interpreted as an induced electric field along the conductor that produces a voltage, which can be calculated through the following equation:

$$V = \int (u \times B).dl \qquad (5)$$

This induced voltage is referred to as a flux cutting emf or a motional emf. Equation (5) indicates that to maximize the induced voltage in the circuit, the direction of the moving conductor should be perpendicular to the direction of the magnetic field, and the result vector of $(u \times B)$ should be in the same direction as differential length along the length of the conductor. Therefore, the Faraday's law can be rewritten as [55],

$$\oint_C E.dl = -\int_S \frac{\partial B}{\partial t}.ds + \oint_C (u \times B).dl \qquad (6)$$

According to equation (6), the time variation of magnetic flux density and/or a moving circuit with a velocity *u* in a magnetic field produces electric field that can induce

current in an electrical conductor in a closed circuit configuration. Since there is no time-varying magnetic field in designed electromagnetic energy harvester, the first term on the right hand side of (6) is equal to zero. Therefore, only the second term on the right hand side of (6), which presents a moving conductor in a static magnetic field, induces voltage in the coil.

2.1. Boundary conditions for magnetic field vectors

Prior to solving the magnetic problems, the pattern for how the magnetic flux density (*B*) and magnetic field intensity (*H*) will change when they cross the boundary between the two different media that have different magnetic properties, is needed. The boundary conditions are determined by applying the integral form of Maxwell's equations to a small cylinder and a small closed path at an interface of the two media.

The boundary condition for the normal component of magnetic flux density (*B*) is obtained from divergence equation, which is [55]:

$$\oint_S B.ds = 0 \qquad (7)$$

In general, the application of the integral form of a divergence equation to a shallow cylinder at an interface with top and bottom faces in the two contiguous media yields the boundary condition for the normal component; and the application of the integral form of a curl equation to a flat closed path at a boundary with top and bottom sides in the two touching media gives the boundary condition for the tangential component. From the divergenceless nature of the magnetic flux density (*B*) field, it can be concluded that the normal component of *B* is continuous across an interface [55]:

$$B_{1n} = B_{2n} \qquad (8)$$

where B_{1n} is the normal component of *B* in media 1 (iron), and B_{2n} is the normal component of *B* in media 2 (air), as shown in figure 1.

The magnetic flux density (*B*) quantity is the only vector needed to study magnetostatics *in free space,* but in other materials it is convenient to define another vector field, which is called the magnetic field intensity (*H*). The purpose of defining the magnetic field intensity (*H*) vector is to account for the effect of magnetization, which is a vector to define the macroscopic effect of magnetic materials in a magnetic field. For homogenous media:

$$B = \mu H \qquad (9)$$

where μ is the permeability of media. Therefore (8) becomes [55]:

$$\mu_1 H_{1n} = \mu_2 H_{2n} \qquad (10)$$

The boundary condition for the tangential component of the magnetic field intensity (*H*) can be obtained from [56]:

$$\oint_C H.dl = \int_S (J + \frac{\partial D}{\partial t}).ds \qquad (11)$$

where *J* is the density of free currents, and the term $\partial D / \partial t$ is called displacement current density, which is necessary to make (11) consistent with the principle of conservation of charge.

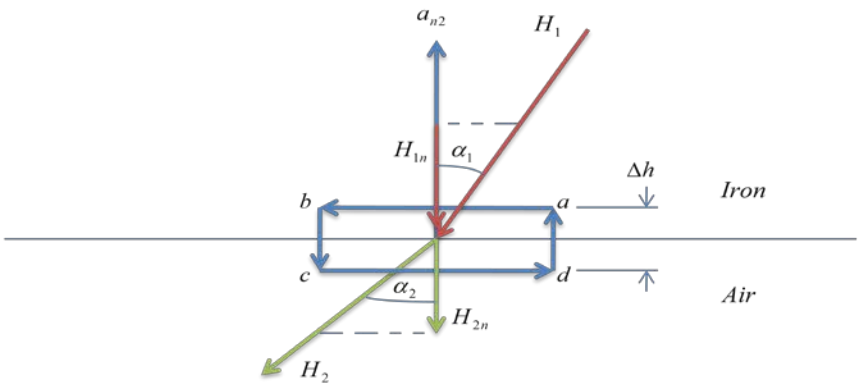

Figure 1. Closed path about the interface of two media to determine the boundary condition

The closed path *abcda* in figure (1) is chosen as the contour *C*. Letting bc = da = Δh approach zero, then,

$$a_{n2} \times (H_1 - H_2) = J_S \qquad (12)$$

where a_{n2} is the outward unit normal from medium 2 (air) at the interface, and J_s is the surface current density on the interface normal to the contour *C*. Thus, the tangential component of the *H* field is discontinuous across an interface where a free surface current exists, and the amount of discontinuity is determined by (12). It should be mentioned that J_s exists only when an interface with an ideal perfect conductor or a superconductor is assumed, otherwise J_s is zero. Therefore, the tangential component of *H* is continuous across the boundary of almost all physical media. Equations (8) and (12) are the boundary conditions which are used in simulation process.

2.2. Calculation of magnetic flux density (*B*) for permanent magnet used in the energy harvesting setup

In order to calculate the magnetic flux density (*B*) of the permanent magnet, some concepts should be defined first. But before proceeding, keep in mind that an exact analysis of magnetic circuits is very difficult to achieve, since:

1. Accounting for leakage fluxes (fluxes which stray or leak from the main flux paths of a magnetic circuit) is really a difficult approach;

2. The fringing effect which causes the magnetic flux lines at the air gap to spread is hard to capture;

3. The permeability (μ) of ferromagnetic materials depends on magnetic field intensity (H); that is, magnetic flux density (*B*) and magnetic field intensity (*H*) have a nonlinear relationship.

2.2.1. Curl of a vector field

In general, there are two kinds of field sources: flow source, and vortex source. The vortex source causes a circulation of a vector field. This circulation of a vector field around a closed path is defined as the scalar line integral of the vector over the path, as shown below [55]:

Circulation of X around contour $C \equiv \oint_C X.dl$ (13)

Equation (13) is a mathematical definition and its physical meaning depends on the type of the field which the vector *X* represents. As an example, if *X* is magnetic field intensity, then the circulation will be a current around the closed path. Since circulation as defined in equation (13) is a line integral of a dot product, thus its value depends on the orientation of the contour *C* relative to the vector *X*. In order to define a point function for measuring the strength of a vortex source, contour *C* should be made very small and its orientation should maximize the circulation. Therefore, the curl of a vector field, denoted by $\nabla \times X$, is defined as follows [55]:

$$\nabla \times X \equiv \lim_{\Delta S \to 0} \frac{1}{\Delta S} [a_n \oint_C X.dl]_{\max} \qquad (14)$$

where area ΔS is bounded by contour C and a_n is the vector normal to that area, which its direction follows the right-hand rule; that is when the fingers of the right hand follow the direction of dl, the thumb points to the a_n direction.

It can be shown that in spherical coordinate system, the curl of a vector field (X) can be calculated through following equation:

$$\nabla \times X = \frac{1}{R^2 \sin\theta} \begin{vmatrix} a_R & a_\theta R & a_\phi R \sin\theta \\ \frac{\partial}{\partial R} & \frac{\partial}{\partial \theta} & \frac{\partial}{\partial \phi} \\ X_R & R X_\theta & R \sin\theta X_\phi \end{vmatrix} \qquad (15)$$

2.2.2. Vector magnetic potential

Since the magnetic flux density (B) is in a solenoid, it can be expressed as the curl of another vector field, like A, as determined below [57]:

$$B = \nabla \times A \qquad (16)$$

where the vector field A is called the vector magnetic potential. It can be proven that this vector magnetic potential (A) of a point at a distance R from a volume current density (J) can be calculated through following equation:

$$A = (\mu_0 / 4\pi) \int_v (J/R) dv \qquad (17)$$

where μ_0 is the permeability of free space, and *v* is the volume where volume current density (*J*) has been distributed on it.

2.2.3. Magnetization and equivalent current densities

As mentioned before, magnetization is a vector to define the macroscopic effect of magnetic materials in a magnetic field. Magnetization is caused by electrons of atoms which are the basic components of all materials. These orbiting electrons cause circulating currents and form microscopic magnetic dipoles. When there is no external magnetic field, the magnetic dipoles of the atoms of most materials (except permanent magnets) have random orientations, which resulting in no magnetic moment in total. But applying an external magnetic field to materials causes the magnetic moments of the spinning electrons to align. Moreover, due to a change in the orbital motion of electrons, magnetic moment is going to induce in the material. To determine the quantitative change in the magnetic flux density caused by magnetic material presence, assume m_k is the magnetic dipole moment of an atom. Suppose there are *n* atoms per unit volume in the material, a magnetization vector (*M*) is defined as [58]:

$$M = \lim_{\Delta v \to 0} \frac{\sum_{k=1}^{n\Delta v} m_k}{\Delta v} \qquad (18)$$

which represents the volume density of the magnetic dipole moment. It can be proven that the effect of the magnetization vector can be interpreted as both a volume current density (J_m) and a surface current density (J_{ms}), as demonstrated in the following equations, respectively.

$$J_m = \nabla \times M \qquad (19)$$

$$J_{ms} = M \times a_n \qquad (20)$$

where a_n is the unit outward normal vector from the surface bounding the volume of the magnetized body.

2.2.4. Magnetic flux density (B) calculation

Now that all necessary concepts have been explained, it is time to calculate the magnetic flux density (*B*) of the permanent magnet which has been used in the energy harvesting setup. The permanent magnet is in the shape of a hollow cylinder with outer radius *b*, inner radius a, and length *L*. Moreover, the permanent magnet has been magnetized axially, as shown in figure below:

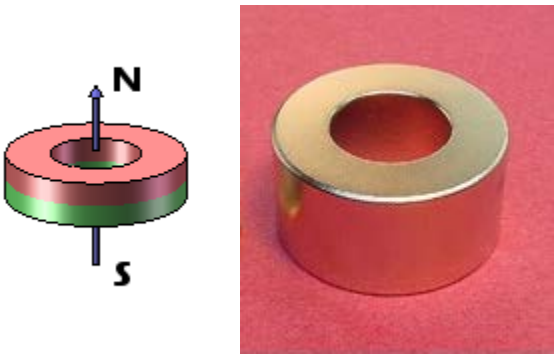

(a) (b)

Figure 2. (a) The magnetization of permanent magnet which has been used in energy harvester setup; (b) the permanent magnet itself

Suppose the axis of the magnetized hollow cylinder coincide with the z-axis of the cylindrical coordinate system, as shown in figure (2).

The total magnetization (*M*) within the whole volume of permanent magnet is constant and equal to:

$$\vec{M} = M_0(\vec{a_z}) \qquad (21)$$

Therefore, $J_m = \nabla \times M = 0$, which means there is no equivalent volume current density. But, the equivalent surface current density on the outer side wall of the hollow cylinder is equal to:

$$\vec{J}_{ms} = \vec{M} \times \vec{a}_n = M_0(\vec{a}_z) \times (\vec{a}_r) = M_0(\vec{a}_\phi) \qquad (22)$$

Similarly, the equivalent surface current density on the inner side wall of the hollow cylinder is equal to:

$$\vec{J}_{ms} = \vec{M} \times \vec{a}_n = M_0(\vec{a}_z) \times (-\vec{a}_r) = M_0(-\vec{a}_\phi) \qquad (23)$$

First, the vector magnetic potential (*A*) is going to be calculated and then from it, the magnetic flux density (*B*) is going to be determined by $\nabla \times A$. For convenience in calculations, it is easier to consider that the surface current density (J_{ms}) flowing on the side wall of the hollow cylinder is the same as a current $I = M_0 L$ flowing on a circular loops of radiuses *b* and *a*, for the outer side wall and inner side wall of the hollow cylinder, respectively. Therefore, considering figure (3), equation (17) can be rewritten as:

$$A = (\mu_0 M_0 L/4\pi)\oint_{C'}(dl'/R') - (\mu_0 M_0 L/4\pi)\oint_{C'}(dl'/R'') \qquad (24)$$

Because of symmetry, the magnetic field is independent of the angle ϕ of the field point (the desired point to calculate magnetic flux density and is demonstrated as *P* in figure (3)). Thus, for convenience, the point *P*(*R*, θ, $\pi/2$) in the *yz*-plane has been chosen for calculation.

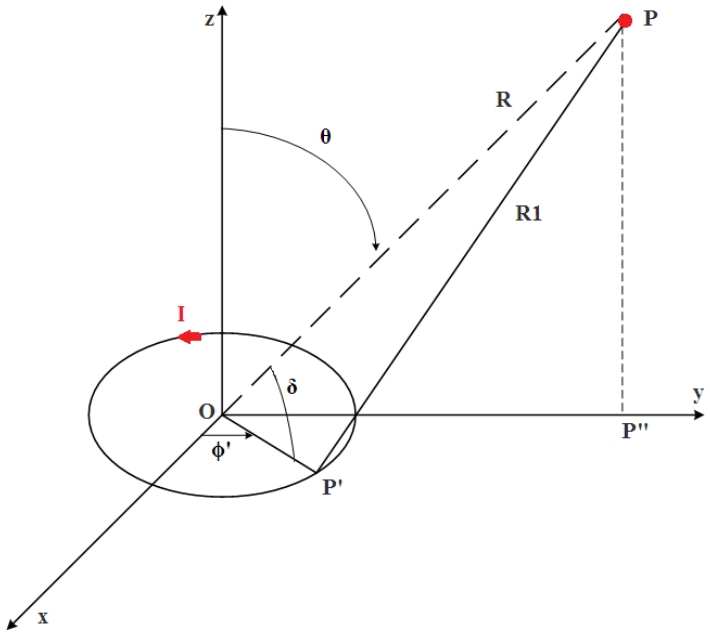

Figure 3. ***A small circular loop carrying current I equivalent to surface current density on the side wall of the permanent magnet***

Note that $\vec{a}_{\phi'}$ at $\vec{dl'}$ is not the same as $\vec{a}_{\phi}$ at point *P*. In fact, $\vec{a}_{\phi}$ at P is $-\vec{a}_x$. Therefore, for outer side wall of the hollow cylinder, the differential length-change is equal to:

$$dl' = (-\vec{a}_x \sin\phi' + \vec{a}_y \cos\phi')b.d\phi' \qquad (25)$$

Similarly, the differential length-change for inner side wall of the hollow cylinder is equal to:

$$dl' = (-\vec{a}_x \sin\phi' + \vec{a}_y \cos\phi')a.d\phi' \qquad (26)$$

Based on symmetry of the equivalent current loop, for every differential current element as $I\,\vec{dl'}$, there is another one located on the other side of the y-axis which will

contribute an equal amount to the vector magnetic potential (A) in the $-\vec{a}_x$ direction, but on the other hand, will cancel its contribution in the $\vec{a}_y$ direction. Consequently, equation (24) is simplified to:

$$A = (-\vec{a}_x)(\mu_0 M_0 L/4\pi)\int_0^{2\pi}(b\sin\phi'/R')d\phi' + (\vec{a}_x)(\mu_0 M_0 L/4\pi)\int_0^{2\pi}(a\sin\phi'/R'')d\phi' \quad (27)$$

or:

$$A = (\vec{a}_\phi)(\mu_0 M_0 Lb/2\pi)\int_{-\pi/2}^{\pi/2}(\sin\phi'/R')d\phi' - (\vec{a}_\phi)(\mu_0 M_0 La/2\pi)\int_{-\pi/2}^{\pi/2}(\sin\phi'/R'')d\phi' \quad (28)$$

Applying the cosines' law to the triangle OPP' will result in the following equations:

$$R'^2 = R^2 + b^2 - 2Rb\cos\delta \quad (29)$$

and:

$$R''^2 = R^2 + a^2 - 2Ra\cos\delta \quad (30)$$

Note that *Rcosδ* is the projection of *R* on both radiuses OP' and OP'', which is the same as the projection of OP_1 on both of them. On the other hand, OP_1 itself is equal to *Rsinθ*. Hence, equations (29) and (30) can be rewritten as:

$$R'^2 = R^2 + b^2 - 2Rb\sin\theta\sin\phi' \qquad (31)$$

and:

$$R''^2 = R^2 + a^2 - 2Ra\sin\theta\sin\phi' \qquad (32)$$

Therefore:

$$\frac{1}{R'} = \frac{1}{R}\left(1+\frac{b^2}{R^2}-\frac{2b}{R}\sin\theta\sin\phi'\right)^{-1/2} \qquad (33)$$

and:

$$\frac{1}{R''} = \frac{1}{R}\left(1+\frac{a^2}{R^2}-\frac{2a}{R}\sin\theta\sin\phi'\right)^{-1/2} \qquad (34)$$

Substituting the above equations into equation (28) yields:

$$A=(\vec{a_\phi})(\mu_0 M_0 Lb/2\pi R)\int_{-\pi/2}^{\pi/2}\left(1+\frac{b^2}{R^2}-\frac{2b}{R}\sin\theta\sin\phi'\right)^{-1/2}\sin\phi' d\phi' \\ -(\vec{a_\phi})(\mu_0 M_0 La/2\pi)\int_{-\pi/2}^{\pi/2}\left(1+\frac{a^2}{R^2}-\frac{2a}{R}\sin\theta\sin\phi'\right)^{-1/2}\sin\phi' d\phi' \quad (35)$$

This integral can be solved only for points whose distances (*R*) from the bottom center of permanent magnet are much greater than the outer radius of permanent magnet (i.e. when *R*>>*b*) to make simplifying approximations; but since in above mentioned case, $R \approx b$, no solution for vector magnetic potential (*A*) could be found and therefore no theoretical model for electromagnetic energy harvester is obtained.

3. THE PARAMETER STUDY OF ELECTROMAGNETIC ENERGY HARVESTER

In this chapter, the structure of the electromagnetic energy harvester for linear applications has been explained and the design procedure through simulation analysis has been described. Then, the experimental analysis on diverse parameters of the setup such as, the length of the iron cylinder, the resistance of the coil and the load, the effect of slope on the iron cylinder, and the effect of the tooth-shape edges on the iron core has been examined. Finally, a conclusion has been made through various experimental results.

3.1. The modified voice coil energy harvester structure and simulation analysis

The configuration of the modified voice coil energy harvester structure is shown in figure (4). The harvester is composed of an iron core with conical end, soft iron cylinder, permanent magnet, and moving coil. The components are connected as shown in figure (4). This energy harvester architecture has a symmetric design configuration about the z-axis, which simplifies its mathematical modeling and finite element analysis (i.e. 2D simulation is possible).

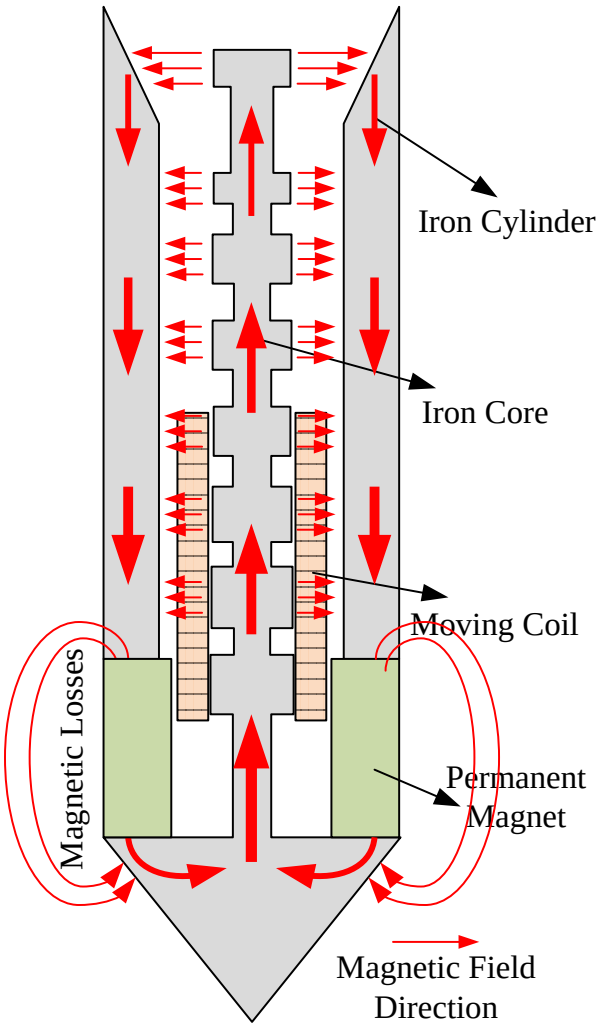

Figure 4. The main parts of the modified voice coil energy harvester

To understand the structure of the design much better, some points need to be discussed further in details.

First, the main reason for the conical end of iron core is to make the magnetic circuit (iron core) as far as possible from permanent magnet to avoid the flux linkages to close themselves through the outside air and hence, to reduce the magnetic losses, which is illustrated in figure (5). As it has been demonstrated, the magnetic flux density (the red streamlines) in figure 5-b (without conical end), outside the energy harvester structure, are denser than the magnetic flux density outside the energy harvester structure in figure 5-a (with conical end). Therefore, the conical end of the iron core is reduced the magnetic losses.

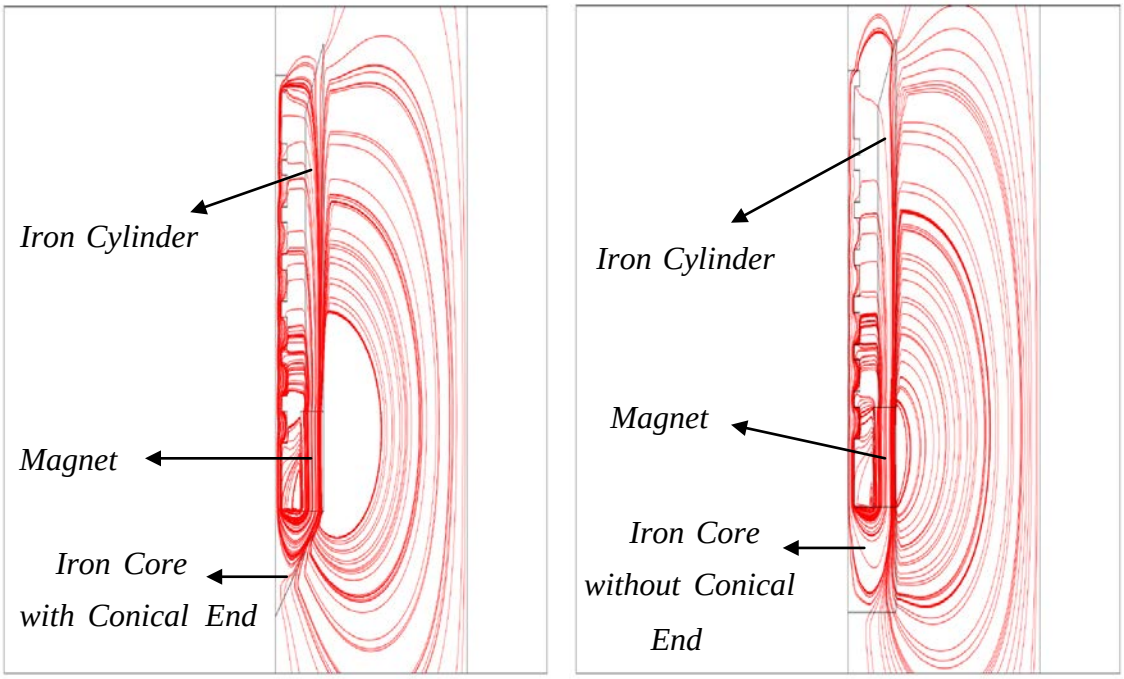

(a) (b)

Figure 5. The effect of conical end of iron core on magnetic losses

Second, the reason for tooth-shape edges on iron core is to increase the magnetic flux density in the air gap between the iron core and the iron cylinder. But, the simulation analysis with the aim of Comsol Multiphysics, which was based on trial and error procedure, indicated that these tooth-shape edges on iron core has not increased the magnetic flux density compare to the case when iron core was completely straight. This phenomenon has been demonstrated in figure (6). Comparing figures (6-a) and (6-b), two points can be concluded. First, the magnetic flux density (the red streamlines) in figure 6-b (straight iron core), outside the energy harvester structure, are much less than the magnetic flux density outside the energy harvester structure in figure 6-a (iron core with tooth-shape edges). Second, the density of these streamlines inside straight iron core is higher than the iron core with tooth-shape edges. Based on two above mentioned points, the magnetic flux density (B) in the air gap between the iron core and the iron cylinder is stronger when the iron core is straight.

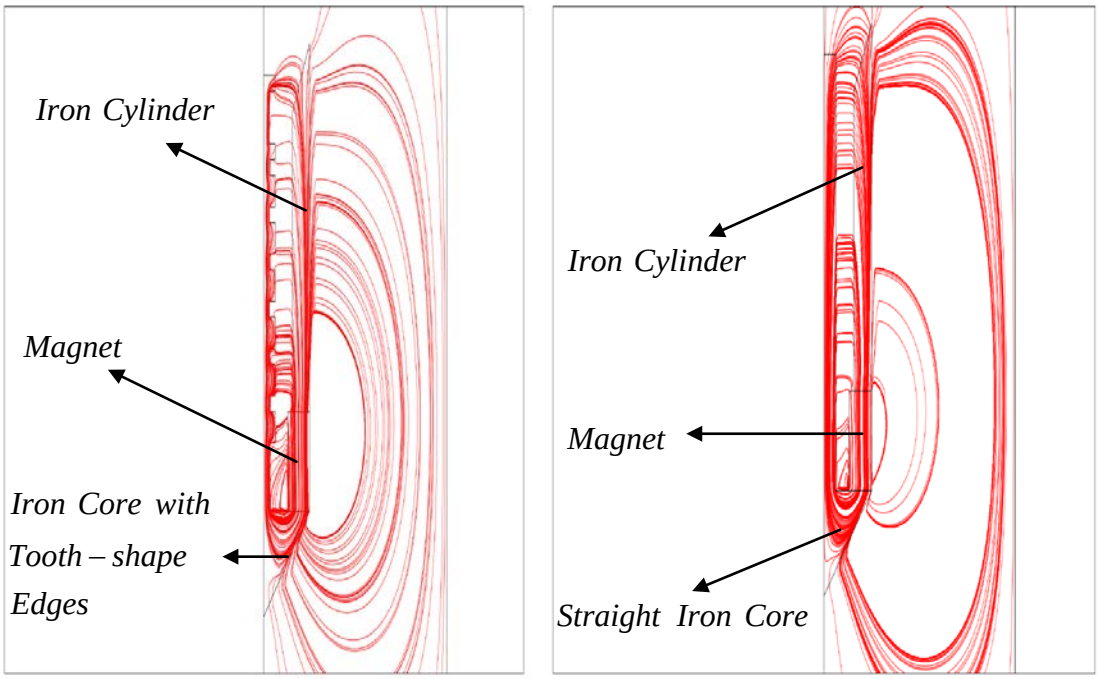

(a) (b)

Figure 6. The effect of tooth-shape edges of iron core on magnetic field in air gap

Finally, the reason for the slope at the end of iron cylinder is to avoid the flux leakages and magnetic losses, and therefore increase the strength of magnetic field on top of the structure. Moreover, when the iron cylinder has slope at its end, the flux lines will emerge into air in a direction almost normal ($\approx 90^\circ$) to the interface on top of the electromagnetic energy harvester structure (figure 7-a). But when the iron cylinder does not have this slope, the flux lines will emerge into air in a direction less than normal ($< 90^\circ$) to the interface on top of the structure (figure 7-b). Since the induced voltage is proportional to the Sine of the angle between velocity (*u*) and magnetic flux density (*B*), where velocity (*u*) is in z-axis direction, therefore decrement in emerge angle of flux lines into air will cause the value of the Sine decreases a little, which will result in smaller induced voltage, as will be verified later with experimental analysis.

To conclude the above discussion, it has been illustrated that creating slope at the end of iron cylinder, plus having a straight iron core with conical end will result in

stronger magnetic field inside the electromagnetic energy harvester structure compare to other geometric designs.

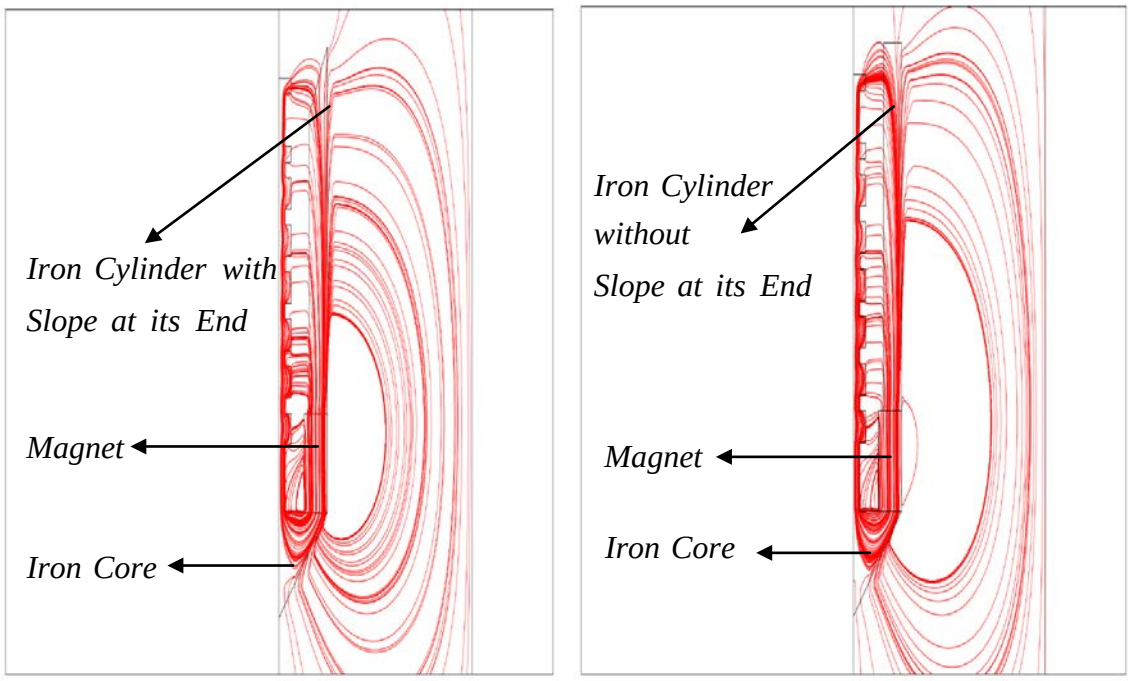

(a) (b)

Figure 7. The effect of slope at the end of iron cylinder on magnetic losses

A finite element analysis (FEA) has been conducted to better realize the flux linkage with the coil, demonstrate the magnetic flux density pattern, and estimate the induced current in the coil. The analysis of the energy harvester structure is done using COMSOL Multiphysics software.

In the simulation process, the magnetization has been chosen to be in z-direction since the magnet is axially magnetized. To calculate the magnetization, the *B-H* curve of the magnet is used in the fallowing relationship [58]:

$$\vec{M} = \frac{1}{\mu_0}\vec{B} - \vec{H} \qquad (36)$$

where *B* is the magnetic field density and H is the magnetic field intensity.

Based on the dimensions of the magnet, the Permeance Coefficient can be extracted from the table which relates the Permeance coefficient of a magnetic media to its dimensions. Therefore, the Permeance coefficient for the used magnet in our setup is 2.211. Therefore, from *B-H* curve of the magnet and with this Permeance Coefficient, the magnetic field density (*B*) is equal to 13000 Gauss or 1.3 [T] and the magnetic field intensity (*H*) is equal to -6000 [Oe] or -477 [kA/m]. Hence, the magnetization's value is equal to 1.5 [MA/m].

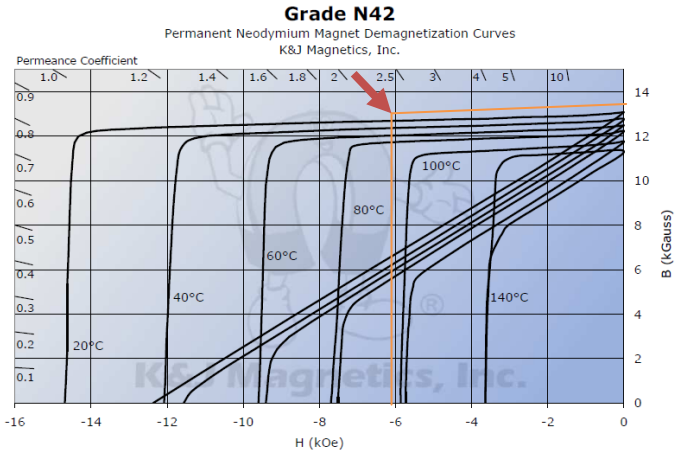

Figure 8. The B-H curve for permanent magnet [59]

In the first step, figure (9) demonstrates the magnetic flux density streamline in the cross sectional area of the energy harvester in 2D axial symmetry cylindrical coordinate. The red lines in this figure indicate the magnetic flux density streamline. Now we have examined that whether the demonstrated pattern for magnetic flux density in simulation analysis matches the theory principles or not. If two magnetic media with permeabilities μ_1 and μ_2 have a common boundary, and the magnetic flux density in medium 1 and 2 makes an angle α_1 and α_2 with the normal vectors on the planes where magnetic medias are in them , respectively, then [55]:

$$\frac{\tan\alpha_2}{\tan\alpha_1} = \frac{\mu_2}{\mu_1} \qquad (37)$$

(37) illustrates that if medium 1 is ferromagnetic (like iron) and medium 2 is air, which means $\mu_1 >> \mu_2$, then α_2 will be nearly zero. In other words, if a magnetic field

originates in a ferromagnetic medium, similar to this energy harvester, the flux lines will emerge into air in a direction almost normal to the interface, as is shown in figure (9). Therefore, the pattern for magnetic field, which is demonstrated by simulation, exactly matches the theory and with the aim of theory and simulation, it is demonstrated that the magnetic flux density streamline inside the setup (between iron core and iron cylinder) is radial.

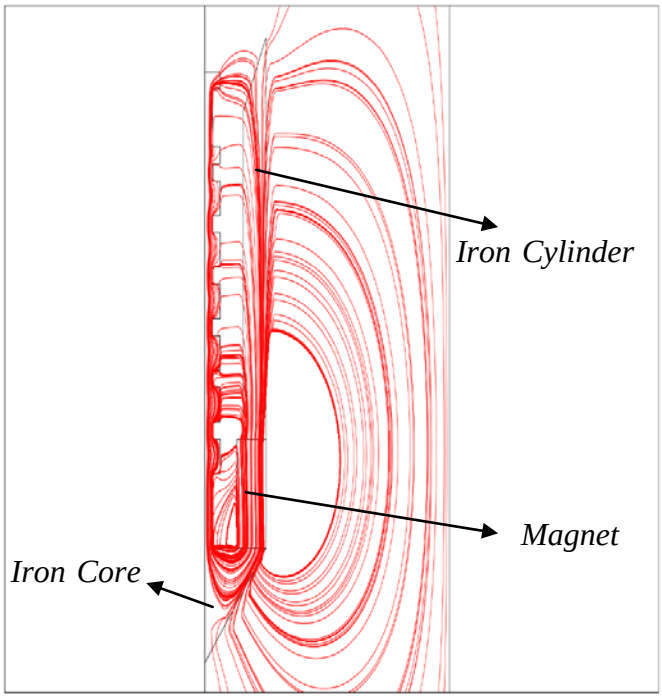

Figure 9. ***Magnetic flux density streamline for primary design of electromagnetic energy harvester when iron core has conical end, has tooth-shape edges on it, and iron cylinder has slope at its end***

3.2. Analyzing the sinusoidal base excitation vibration through shaker setup

3.2.1. Simulation analysis of sinusoidal base excitation vibration

The First question that needs to be answered is that where would be the ideal initial position for the coil to produce maximum induced voltage. Therefore, it has been

examined that how the initial position of the coil will affect on the induced voltage value. To do so, the excitation of the coil is defined as:

$$Z = 0.5 \sin (70.\pi.t) \text{ mm} \quad (38)$$

To conduct the simulation analysis through Comsol Multiphysics, two main steps should be done. First, the excitation equation should be defined through moving meshes, which indicates the pattern for the movement of each part of the setup. Second, the material properties for each part of the setup, such as magnet, iron cylinder, coil, and air gap, in addition to their boundary conditions, which has been discussed earlier, should be identified to be able to plot diverse electromagnetic variables.

During the simulation analysis, the coil has been placed inside the setup completely and then it has been moved toward the top of the setup slowly. 18 different initial positions for the coil have been tested and each time, the induced current in the coil has been recorded. Considering the fact that the resistance of the coil is equal to 20.4 [Ω], with the help of Ohm's law, which is:

$$V = R.I \quad (39)$$

where V is the induced voltage, I is the induced current, and R is the resistance of the coil, the induced voltage within these initial positions has been calculated and the result is demonstrated in figure (10).

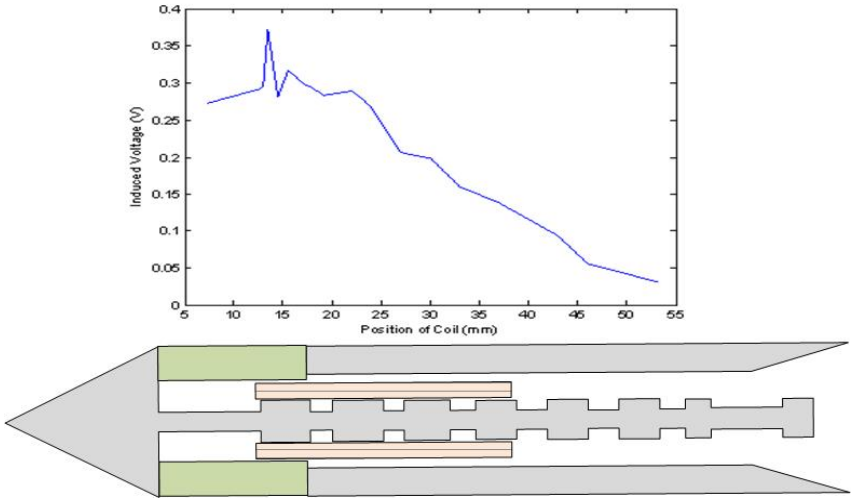

Figure 10. Induced voltage vs. Initial position of the coil: simulation result

Figure (10) indicates that around 13 [mm] on top of the conical end of the structure, where exactly the first tooth-shape edge locates, the maximum voltage would induce on coil.

3.2.2. Experimental analysis of sinusoidal base excitation vibration

The energy harvester structure comprises of one outer metal cylinder with the outer radius of 2 [cm], inner radius of 1.25 [cm], and the height of 7 [cm]; one inner metal cylinder with the radius of 0.25 [cm] and the height of 8.3 [cm], and it has the cone shape at one end. Moreover, this iron core has 8 steps on it, where each step has 0.6 [cm] height and 0.25 [cm] width. One fixed Neodymium ring magnet with the outer radius of 1.9 [cm], inner radius of 0.95 [cm], and the height of 1.9 [cm]. The coil's shape is also cylindrical with the outer radius of 8 [mm], inner radius of 4 [mm], and the height of 33 [mm]. Other than the explained energy harvester structure, the experimental setup comprises of an electromagnetic shaker, miniature accelerometer, and a dynamic signal analyser. Figure 11 demonstrates the complete experimental setup.

Figure 11. The shaker experimental setup

The same procedure with similar 18 different initial positions as simulation process and same sinusoidal vibration has been applied on the experimental setup and the experimental result is shown in figure 12.

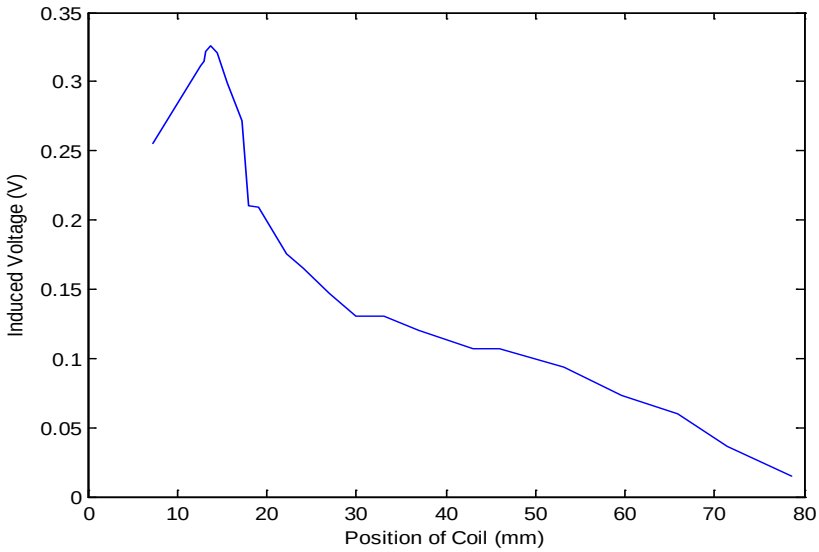

Figure 12. Induced voltage vs. Initial position of the coil: experimental result

Comparing figures (10) and (12), it can be concluded that simulation is in close agreement with the experimental result. The major difference between these two figures

is the peak of induced voltage. The main reasons for this difference are: 1) the flux linkage leakage happens in reality and cannot be captured in the ideal simulation environment, 2) the size of the model navigator that has been selected in the simulation, 3) the property of the iron core and the iron cylinder that is used in the simulation. This also indicates that the losses in reality are more than ideal simulation environment. Moreover, both figures (10) and (12) illustrate that the ideal initial position, where the maximum amount of induced voltage would be captured, is around 13.5 [mm] on top of the cone part of the structure.

3.2.3. Analyzing the effect of design modifications for energy harvester setup through simulation

In subsections 3.2.1. and 3.2.2., it has been demonstrated that the simulation analysis is in close agreement with the experimental result. Therefore, in this subsection, numerous FEA's through COMSOL Multiphysics software have been conducted to demonstrate the design modifications improvements in quantitative manner. The same simulation procedure, as mentioned in subsection 3.2.1., has been conducted here again when only one design parameter has been changed. The following figure illustrates the effect of changing 3 different design parameters on induced voltage of the moving coil.

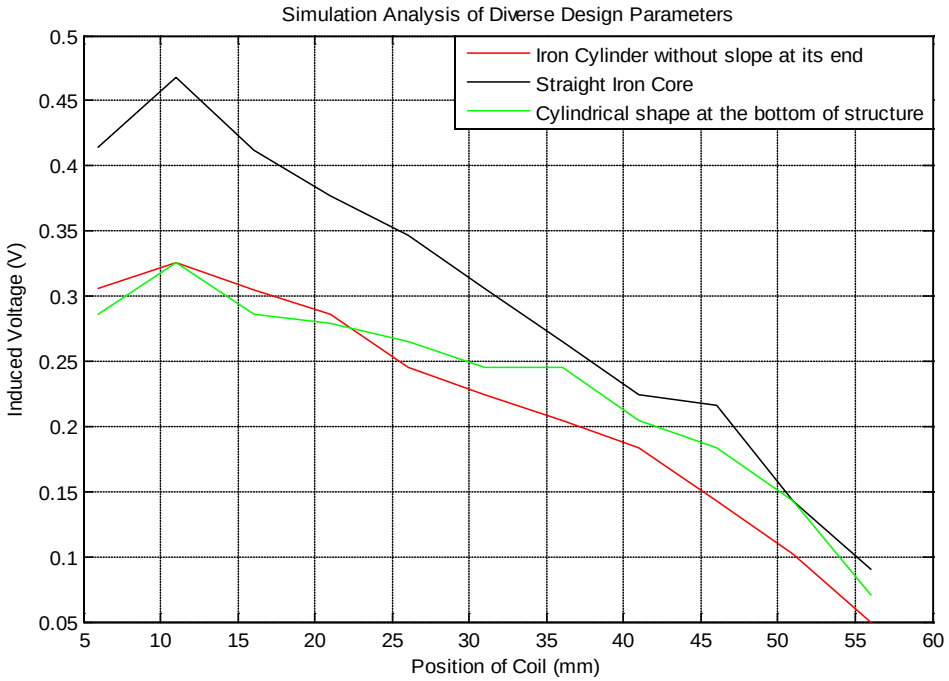

Figure 13. Simulation analysis of three different design parameters

Based on figure (13) and considering figure (10) as the demonstration of induced voltage for original design setup, the improvement percentage of induced voltage in each case can be calculated by definition below:

$$\%\ \ \mathrm{Im}\,provement\ \ Percentage\ \ Factor\ \ (\alpha) = \frac{V_{Ch} - V_{Or}}{V_{Or}} \times 100 \qquad (40)$$

where V_{Ch} is the induced voltage obtained when one design parameter has been changed (demonstrated in figure (13)), and V_{Or} is the induced voltage for original design setup (demonstrated in figure (10)). Based on equation (40), when the slope at the end of iron cylinder has been added, the improvement percentage factor equals:

$$\alpha = \frac{0.373 - 0.326}{0.326} \times 100 = 14.417\% \qquad (41)$$

This positive α indicates that adding the slope at the end of iron cylinder has increased the induced voltage. Therefore, creating the slope at the end of iron cylinder improves the induced voltage by %14.417.

In the next case, when the tooth-shape edges have been removed from the iron core, the improvement percentage factor equals:

$$\alpha = \frac{0.468 - 0.373}{0.373} \times 100 = +25.469\% \qquad (42)$$

This positive α indicates that removing the tooth-shape edges from iron core, and therefore having a straight iron core, increased the induced voltage by %25.469.

Finally, when the bottom of energy harvester structure has a conical shape rather than the cylindrical shape, the improvement percentage factor equals:

$$\alpha = \frac{0.373 - 0.326}{0.326} \times 100 = 14.417\% \qquad (43)$$

Again, this positive α indicates that changing the bottom shape of energy harvester structure from cylindrical to conical has increased the induced voltage. Therefore, the conical shape at the bottom of energy harvester structure improves the induced voltage by %14.417.

3.3. Experimental analysis of linear motion electromagnetic energy harvester with diverse velocities through linear motor setup

3.3.1. Describing the experimental setup for linear motion

The energy harvester has the same structure as described in subsection 3.2.2, but only this time, it has been mounted on a linear motor instead of shaker. A schematic configuration of the experimental setup has been demonstrated in following figure.

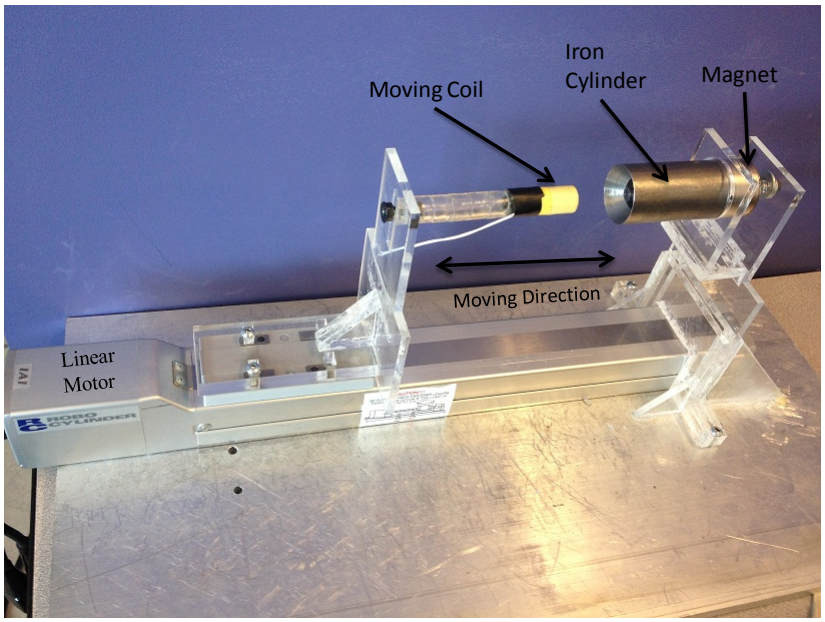

Figure 14. Schematic configuration of the experimental setup for linear motion

In the following subsections, the effects of the length of iron cylinder, the slope at its end, and the resistance of the moving coil have been examined. Moreover, diverse load resistors have been tested at each step to calculate the maximum electrical power extracted from energy harvester. Finally, all of the above mentioned experimental analyses have been repeated when the iron core is straight and does not have any tooth-shape edges to verify the simulation analysis conducted previously. Before starting the experimental analysis, to get a better sense of different lengths of iron cylinder which is going to be discussed later on in this chapter, figure (15) comparing these lengths to each other.

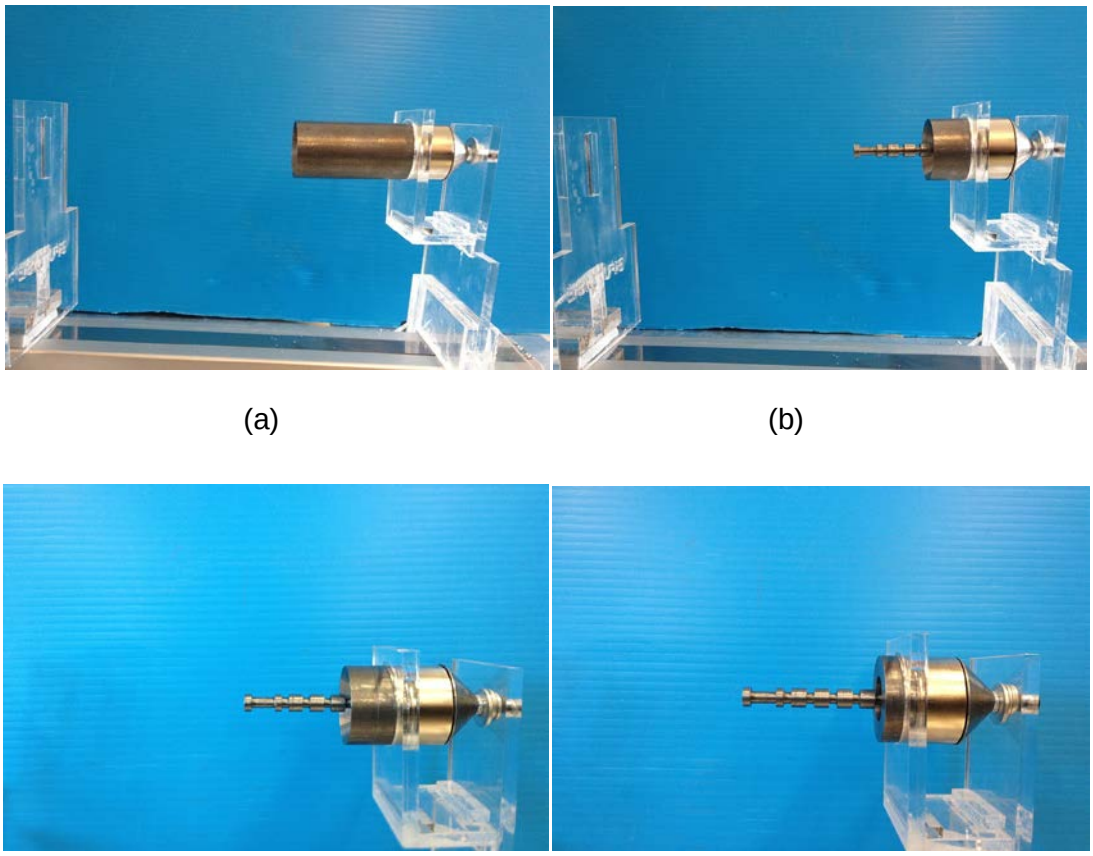

(a) (b)

(c) (d)

Figure 15. Demonstrating diverse lengths of iron cylinder: (a) Original length; (b) Half length; (c) One fifth length; (d) One sixth length

3.3.2. Parameter study of energy harvester when iron cylinder has its primary length

As mentioned before, the primary length of iron cylinder is 70 [mm]. Since the length of the permanent magnet is 20 [mm], therefore the distance from bottom to top of the energy harvester structure is 90 [mm]. First, to examine the coil resistance effect on induced voltage with respect to diverse velocities, the experiment has been done in following two cases:

a) When the iron cylinder has the slope at its end and the coil resistance is equal to 692 [Ω], and;

b) When the iron cylinder has the slope at its end and the coil resistance is equal to 20.4 [Ω]. The following figure represents the results:

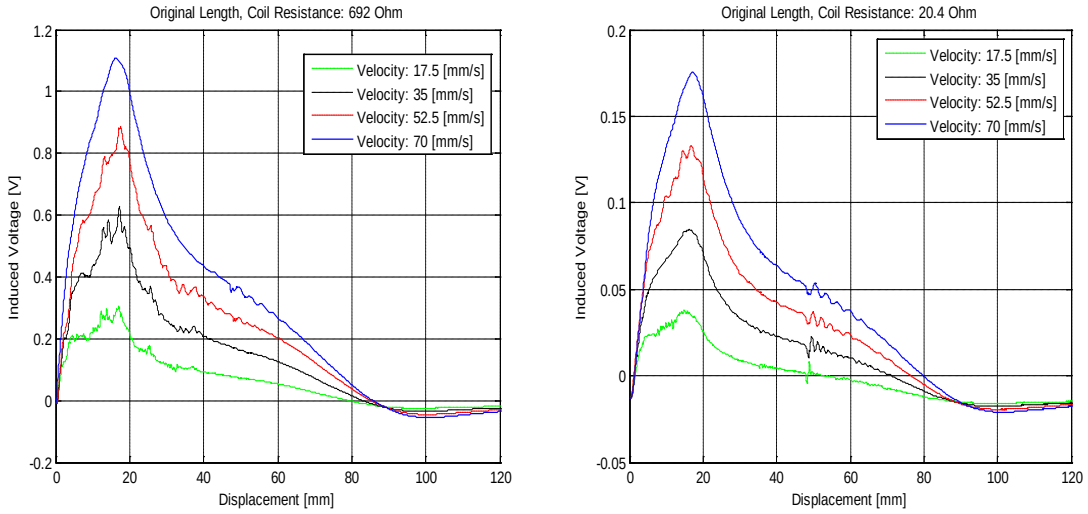

(a) (b)

Figure 16. The coil resistance effect on induced voltage with respect to diverse velocities: (a) coil resistance is 692 [Ω]; (b) coil resistance is 20.4 [Ω]

First of all, it can be concluded that higher velocities will result in higher voltages. Another point which can be interpreted from above figure is that the position of maximum induced voltage is dependent on the velocity of coil's movement slightly. The above figure illustrates that when the velocity of coil's movement varies from 17.5 [mm/s] to 70 [mm/s], then the position of induced voltage's peak changes slightly from 15 [mm] to 20 [mm].

This figure also demonstrates that the relationship between velocity and induced voltage is almost linear, since when the velocity is doubled (from 35 [mm/s] to 70 [mm/s]), then the induced voltage is almost doubled too (from 0.57 [V] to 1.1 [V] in figure 16-a). Moreover, From this figure, it can be seen that when the velocity has been increased, on the other hand, the bandwidth of the maximum induced voltage has been decreased. Comparing two induced voltages when the velocities are 17.5 [mm/s] and 70 [mm/s], although the peak is much higher in case of 70 [mm/s], but the region in which this peak exists is too narrow. On the other hand, in case of 17.5 [mm/s], although the value of voltage's peak is low, but the region in which this peak exists is quite wide.

Therefore, in case of lower velocities, it is possible to cover more distances while still producing the maximum voltage which can be reached.

Finally, it can be seen that when the coil resistance is higher, the induced voltage in the coil is significantly higher with respect to coils with lower resistance. But does this higher voltage result in higher harvested power? The next experiment will help to address this question. Note that since the effect of different velocities has been examined in this case, later on the experimental tests has been conducted only when the velocity of moving coil is 70 [mm/s].

Therefore, the next step of experimental analysis has been conducted to examine the coil resistance effect on harvested power with respect to diverse load resistors. This step has been done again for both cases when the coil resistance is 692 [Ω] and the other one when the coil resistance is 20.4 [Ω]. The results are demonstrated below:

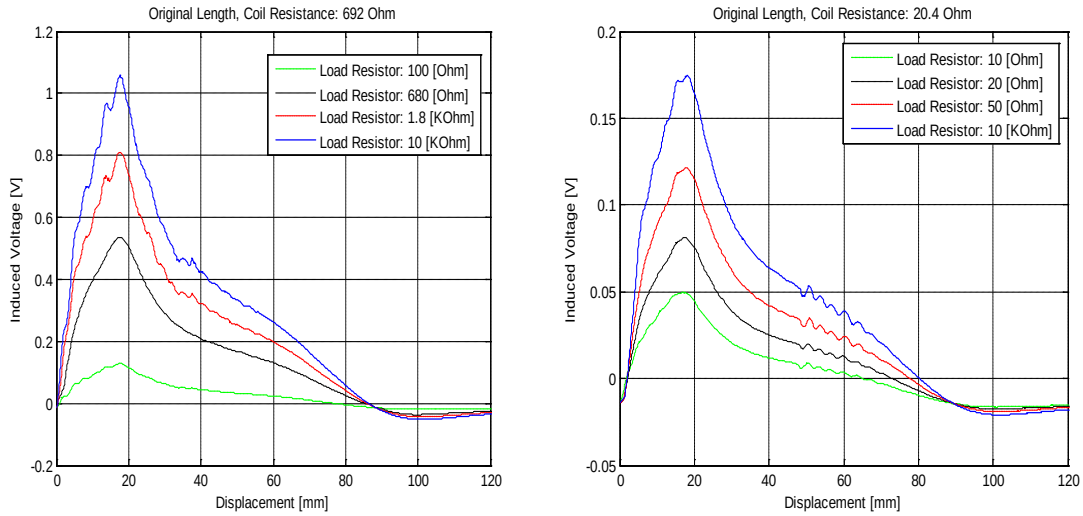

(a) (b)

Figure 17. The coil resistance effect on harvested power with respect to diverse load resistors: (a) coil resistance is 692 [Ω]; (b) coil resistance is 20.4 [Ω]

Based on the impedance matching, the maximum power occurs when the load resistor is equal to the coil resistance. In the case when coil resistance is 692 [Ω], based on the power equation ($P = \frac{V^2}{R}$), the maximum power is equal to:

$P_{\max} = \frac{(0.535)^2}{680} = 0.421[mW]$. The voltage's peaks in figure (17) determine the maximum electrical power which is extracted from energy harvester based on various load resistors that have been tested. Figure (19) compares these powers which have been calculated experimentally to the power versus load resistor graph which has been obtained numerically. To obtain the numerical equation, the whole energy harvester setup has been considered as a voltage source with internal resistor equal to coil resistance. This voltage source is able to produce the maximum voltage V_S which is equal to voltage's peak at speed of 70 [mm/s] when there is no load resistor. The equivalent circuit is illustrated below:

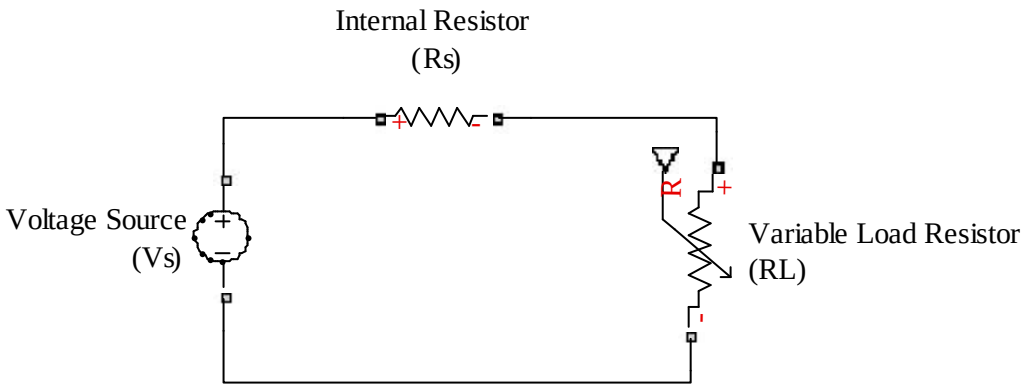

Figure 18. The equivalent electrical circuit for energy harvester setup with variable load resistors

To obtain the numerical graph, the following two equations have been used simultaneously:

$$\begin{cases} V_L = \dfrac{R_L}{R_S + R_L} V_S \\ P_L = \dfrac{{V_L}^2}{R_L} \end{cases} \qquad (44)$$

The result is demonstrated in figure (19).

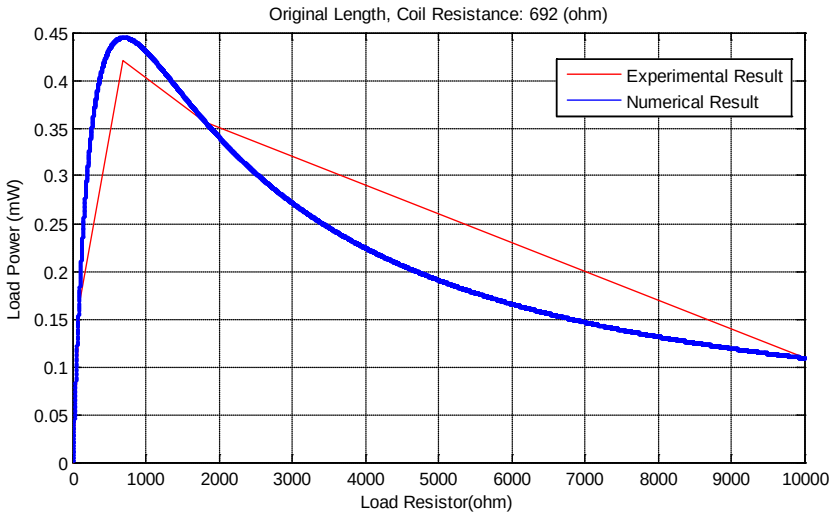

Figure 19. Comparison between numerical analysis and experimental result for load powers with respect to variable load resistors

At last, based on the impedance matching again, the maximum power in the case when coil resistance is 20.4 [Ω], is equal to:

$$P_{\max} = \frac{(0.0815)^2}{20} = 0.3321[mW].$$

Comparing the maximum harvested power in both cases, it can be concluded that although when the induced voltage (or coil resistance) is higher, the harvested power is slightly higher too, but this significantly higher voltage has not resulted in significantly higher power, as the difference in harvested powers between these two cases is less than 0.1 [mW]. Again note that since the effect of different load resistors has been demonstrated in this case, later on the experimental tests has been conducted only with the optimum load resistor which can harvest the maximum power from linear motion.

3.3.3. Parameter study of energy harvester when iron cylinder has half of its primary length

As mentioned before, since the primary length of iron cylinder is 70 [mm], therefore half of its length is 35 [mm]. In this section, all the experiments which have been done in previous section are going to be performed one more time. Additionally,

the effect of slope at the end of iron cylinder on induced voltage with respect to diverse velocities has been examined in this section. To analyze the slope effect, and to keep only one variable parameter in experimental procedure, for only this part it has been chosen to conduct the experiment on the coil with 692 [Ω] internal resistance. The following figure demonstrates the effect of slope at the end of iron cylinder on induced voltage:

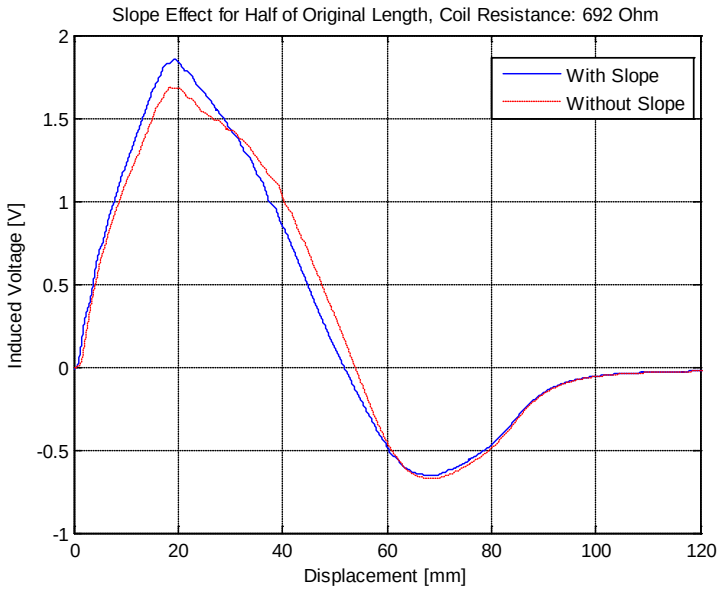

Figure 20. Effect of slope at the end of iron cylinder on induced voltage when iron cylinder has the half of its primary length

This figure illustrates that creating a slope at the end of iron cylinder will improve the amount of induced voltage about 0.2 [V]. Moreover, these two graphs can be used to verify the simulation analysis on improvement percentage factor, which has been conducted in subsection 3.2.3, with experimental results. Since the only parameter which has been changed in this part is the slope at the end of iron cylinder, therefore the improvement percentage factor equals:

$$\alpha = \frac{1.8 - 1.6}{1.6} \times 100 = 12.5\% \qquad (45)$$

which is in close agreement with simulation analysis when the slope at the end of iron cylinder has been added (%14.417).

Now to conduct the experiments which have been done in previous section, first the effect of coil resistance on induced voltage with respect to diverse velocities has been demonstrated.

Since in the previous experiment, it has been concluded that the slope at the end of iron cylinder will cause higher induced voltage, Therefore this part of experiment has been done when the iron cylinder has the slope at its end. Again, the experimental results for both coils are as follows:

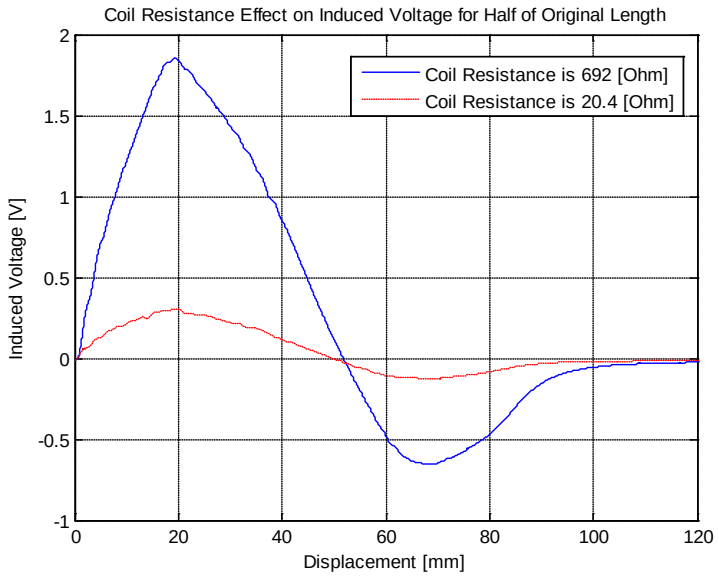

Figure 21. The coil resistance effect on induced voltage when iron cylinder has half of its primary length

When the coil resistance is 20.4 [Ω], the maximum induced voltage which has been reached when the iron cylinder has the half length of its primary length is 0.3 [V], while in similar case when the iron cylinder has its primary length, this maximum induced voltage was around 0.17 [V]. These measurements indicate that when the iron cylinder has been cut to its half length, the induced voltage has increased by the factor 1.76. Similarly, when the coil resistance is 692 [Ω], the maximum induced voltage which has been reached when the iron cylinder has the half length of its primary length is 1.85 [V], while in similar case when the iron cylinder has its primary length, this maximum induced voltage was around 1.1 [V]. Again, these measurements indicate that when the iron

cylinder has been cut to its half length, the induced voltage has increased by the factor 1.68, which is in close agreement when the coil resistance is 20.4 [Ω].

What can be discussed more on figure (21)? Perhaps the most interesting phenomenon which has been illustrated in this figure is that there are two voltage peaks; one is positive, and the other one is negative. This means that there is a point in the structure where the induced voltage in the moving coil equals zero. The position of this point among the structure depends on the length of the iron cylinder. In fact, the length of iron cylinder is equal to the position of the point where the induced voltage is zero. This phenomenon is interesting because the magnetic flux density (*B*) becomes zero with the use of only one permanent magnet and the special design and configuration of the energy harvester setup. To interpret this phenomenon, from induced voltage formulation, since the length of the moving coil is always constant and the velocity of coil's movement is set to a constant value before each experiment, therefore the magnetic flux density (*B*) is the only parameter which is variable. Hence, at this position, the magnetic flux density (*B*) should be zero. The next step is to answer how the magnetic flux density (*B*) becomes zero at this point? Since the magnetic flux density (*B*) is a vector, therefore it becomes zero either when its magnitude becomes zero or when the total resultant of this vector in different directions at that point is zero. In this configuration, the latter case is true since at the end of iron cylinder, some of the magnetic field lines close themselves through the iron core, but the rest of them, which are the magnetic losses, are closing themselves in opposite direction through air. Thus, these two opposite magnetic flux densities cancel out each other and the resultant magnetic flux density (*B*) at the end of iron cylinder becomes zero.

Finally, the effect of coil resistance on harvested power with respect to diverse load resistors for both coils has been determined in following figure:

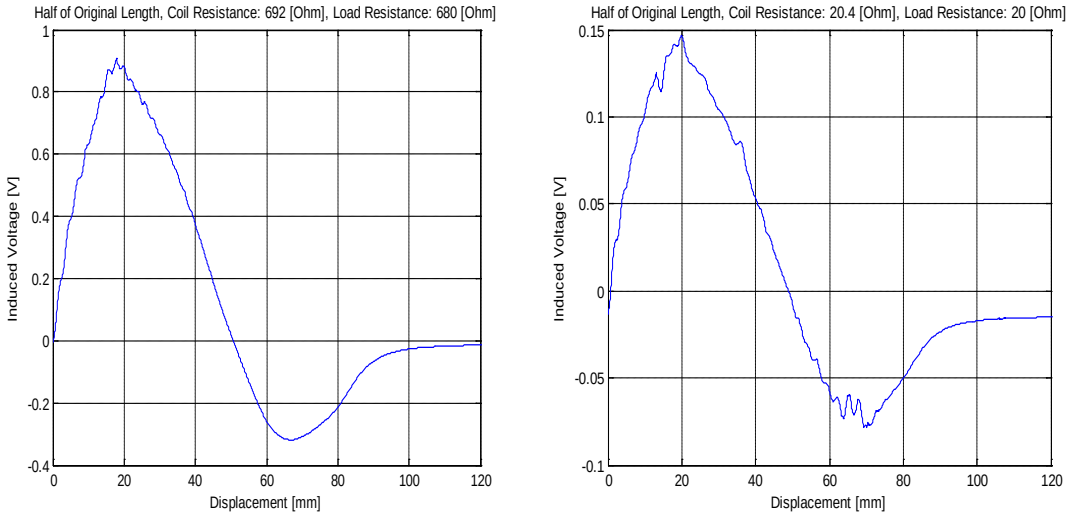

(a) (b)

Figure 22. The coil resistance effect on harvested power when iron cylinder has half of its primary length: (a) coil resistance is 692 [Ω]; (b) coil resistance is 20.4 [Ω]

Based on the impedance matching, the maximum power occurs when the load resistor is equal to the coil resistance. In the case when coil resistance is 692 [Ω], based on the power equation ($P = \frac{V^2}{R}$), the maximum power is equal to:

$$P_{\max} = \frac{(0.900)^2}{680} = 1.191[mW].$$

Again, figure (23) compares both powers which have been calculated experimentally and the power versus load resistor graph which has been obtained numerically for this case.

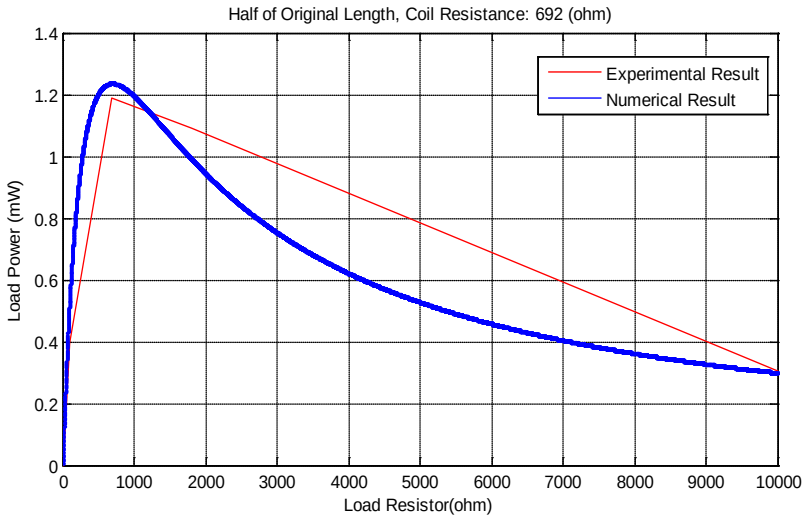

Figure 23. Comparison between numerical analysis and experimental result for load powers with respect to variable load resistors when iron cylinder has half of its primary length

At last, based on the impedance matching again, the maximum power in the case when coil resistance is 20.4 [Ω] is equal to:

$$P_{\max} = \frac{(0.146)^2}{20} = 1.066[mW].$$

Comparing these results to the case when the iron cylinder had its primary length, it can be shown that when the coil resistance is 692 [Ω], the maximum harvested power has increased by the factor 2.829, which is equal to square of the factor that induced voltage has been increased $(1.68)^2$, while when the coil resistance is 20.4 [Ω], the maximum harvested power has increased by the factor 3.21, which is almost equal to square of the factor that induced voltage has been increased $(1.76)^2$.

3.3.4. Parameter study of energy harvester when iron cylinder has one third of its primary length

As discussed earlier, since the primary length of iron cylinder is 70 [mm], therefore one third of its length is 23.33 [mm]. In this section, all the experimental steps which have been done in previous section (3.3.3) are going to be repeated here again.

The following figure illustrates the effect of slope at the end of iron cylinder on induced voltage when the coil resistance is 692 [Ω]:

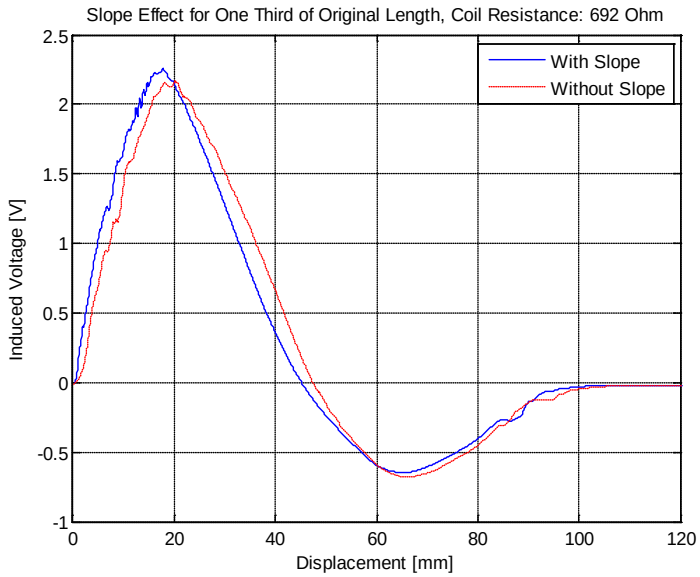

Figure 24. Effect of slope at the end of iron cylinder on induced voltage when iron cylinder has the one third of its primary length

This time, based on figure above, creating a slope at the end of iron cylinder will improve the amount of induced voltage about 0.1 [V].

Second, the effect of coil resistance on induced voltage with respect to diverse velocities has been demonstrated below for both coils:

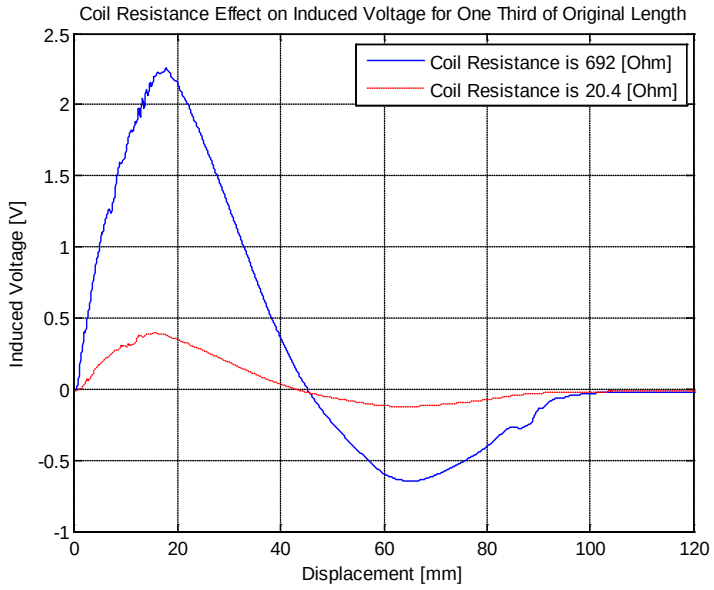

Figure 25. The coil resistance effect on induced voltage when iron cylinder has one third of its primary length

When the coil resistance is 20.4 [Ω], the maximum induced voltage which has been reached when the iron cylinder has the one third length of its primary length is 0.39 [V], while in similar case when the iron cylinder has its primary length, this maximum induced voltage was around 0.17 [V]. These measurements indicate that when the iron cylinder has been cut to its one third length, the induced voltage has increased by the factor 2.3. Similarly, when the coil resistance is 692 [Ω], the maximum induced voltage which has been reached when the iron cylinder has the one third length of its primary length is 2.3 [V], while in similar case when the iron cylinder has its primary length, this maximum induced voltage was around 1.1 [V]. Again, these measurements indicate that when the iron cylinder has been cut to its one third length, the induced voltage has increased by the factor 2.1, which is in close agreement when the coil resistance is 20.4 [Ω].

Third, the effect of coil resistance on harvested power with respect to diverse load resistors for both coils has been determined in following figure:

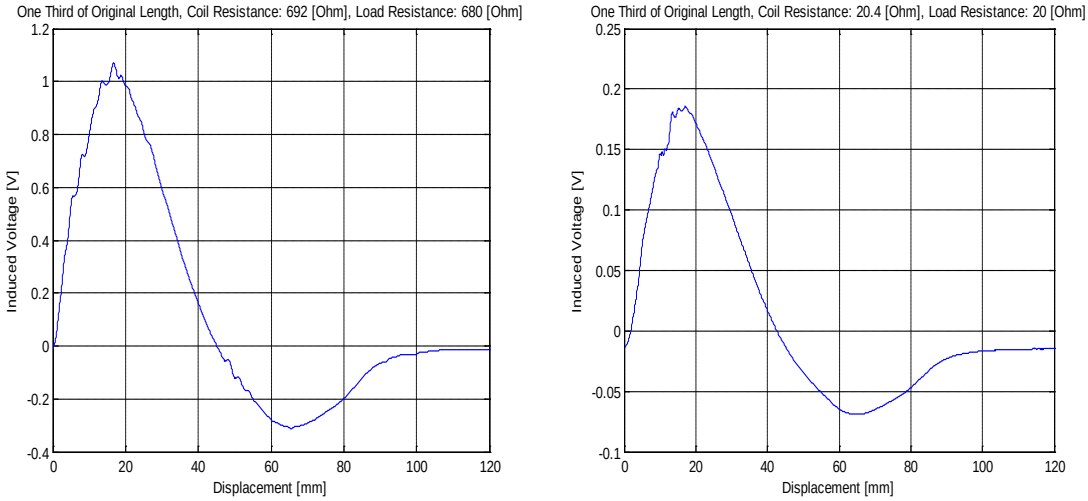

(a) (b)

Figure 26. The coil resistance effect on harvested power when iron cylinder has one third of its primary length: (a) coil resistance is 692 [Ω]; (b) coil resistance is 20.4 [Ω].

Based on the impedance matching and the power equation, the maximum power when coil resistance equals 692 [Ω] is equal to: $P_{\max} = \frac{(1.070)^2}{680} = 1.684[mW]$.

Again, figure (27) compares both powers which have been calculated experimentally and the power versus load resistor graph which has been obtained numerically when the coil resistance is 692 [Ω].

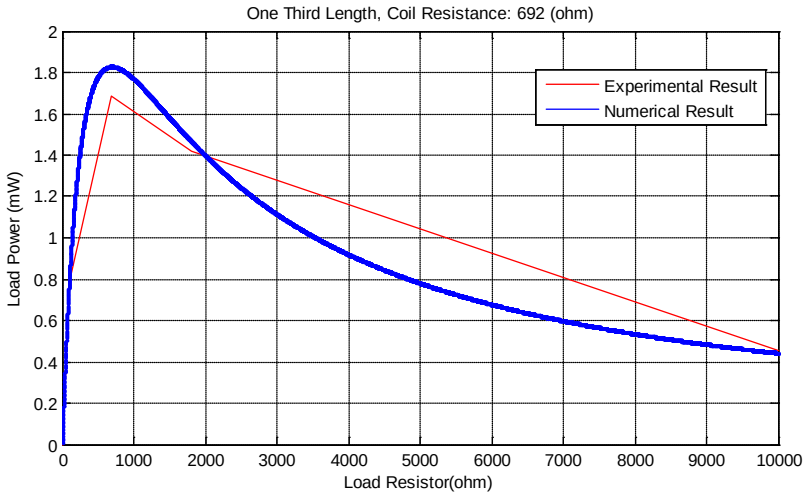

Figure 27. Comparison between numerical analysis and experimental result for load powers with respect to variable load resistors when iron cylinder has one third of its primary length

Finally, based on the impedance matching again, the maximum power in the case when coil resistance is 20.4 [Ω] is equal to:

$$P_{\max} = \frac{(0.185)^2}{20} = 1.711[mW].$$

Comparing these results to the case when the iron cylinder had its primary length, it can be shown that when the coil resistance is 692 [Ω], the maximum harvested power has increased by the factor 4, which is almost equal to square of the factor that induced voltage has been increased $(2.1)^2$, while when the coil resistance is 20.4 [Ω], the maximum harvested power has increased by the factor 5.15, which is almost equal to square of the factor that induced voltage has been increased $(2.3)^2$.

3.3.5. Parameter study of energy harvester when iron cylinder has quarter of its primary length

Same as previous sections, since the primary length of iron cylinder is 70 [mm], therefore quarter of its length is 17.5 [mm]. In this section, all the experimental steps which have been done in previous sections are going to be repeated here again. The

following figure illustrates the effect of slope at the end of iron cylinder on induced voltage when the coil resistance is 692 [Ω]:

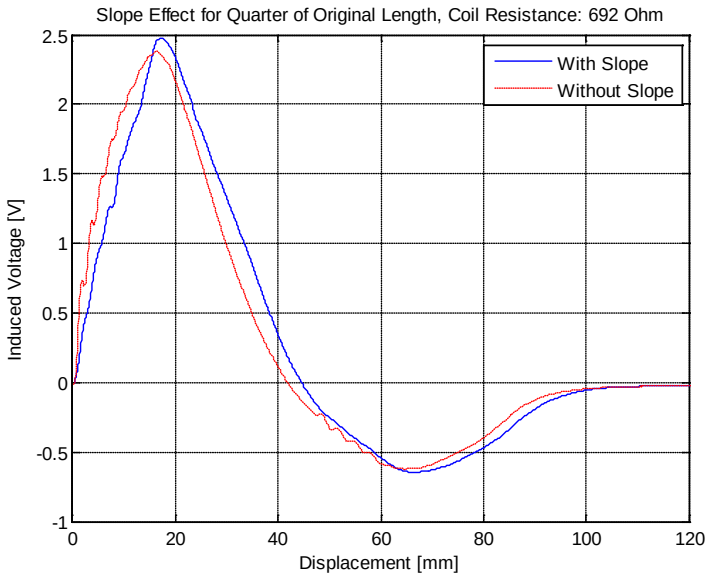

Figure 28. Effect of slope at the end of iron cylinder on induced voltage when iron cylinder has the quarter of its primary length

Again, based on figure above, creating a slope at the end of iron cylinder will improve the amount of induced voltage about 0.1 [V].

Then, the effect of coil resistance on induced voltage with respect to diverse velocities has been demonstrated below for both coils:

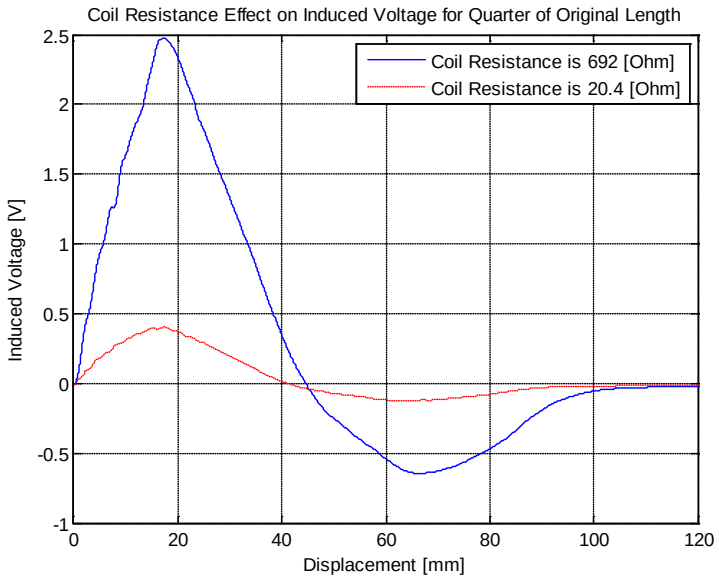

Figure 29. The coil resistance effect on induced voltage when iron cylinder has quarter of its primary length

When the coil resistance is 20.4 [Ω], the maximum induced voltage which has been reached when the iron cylinder has the quarter length of its primary length is 0.4 [V], while in similar case when the iron cylinder has its primary length, this maximum induced voltage was around 0.17 [V]. These measurements indicate that when the iron cylinder has been cut to its quarter length, the induced voltage has increased by the factor 2.35. Similarly, when the coil resistance is 692 [Ω], the maximum induced voltage which has been reached when the iron cylinder has the quarter length of its primary length is 2.45 [V], while in similar case when the iron cylinder has its primary length, this maximum induced voltage was around 1.1 [V]. Again, these measurements indicate that when the iron cylinder has been cut to its quarter length, the induced voltage has increased by the factor 2.23, which is in close agreement when the coil resistance is 20.4 [Ω].

Lastly, the effect of coil resistance on harvested power with respect to diverse load resistors for both coils has been determined in following figure:

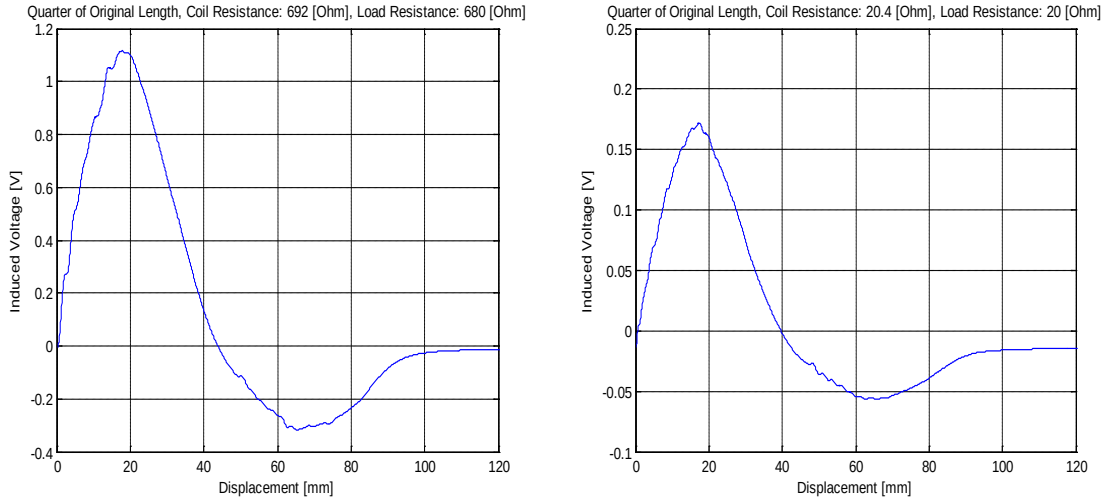

(a) (b)

Figure 30. The coil resistance effect on harvested power when iron cylinder has quarter of its primary length: (a) coil resistance is 692 [Ω]; (b) coil resistance is 20.4 [Ω]

Again, based on the impedance matching, and the power equation, when the coil resistance is 692 [Ω], the maximum power is equal to:

$$P_{\max} = \frac{(1.115)^2}{680} = 1.828[mW].$$

One more time, figure (31) compares both powers which have been calculated experimentally and the power versus load resistor graph which has been obtained numerically.

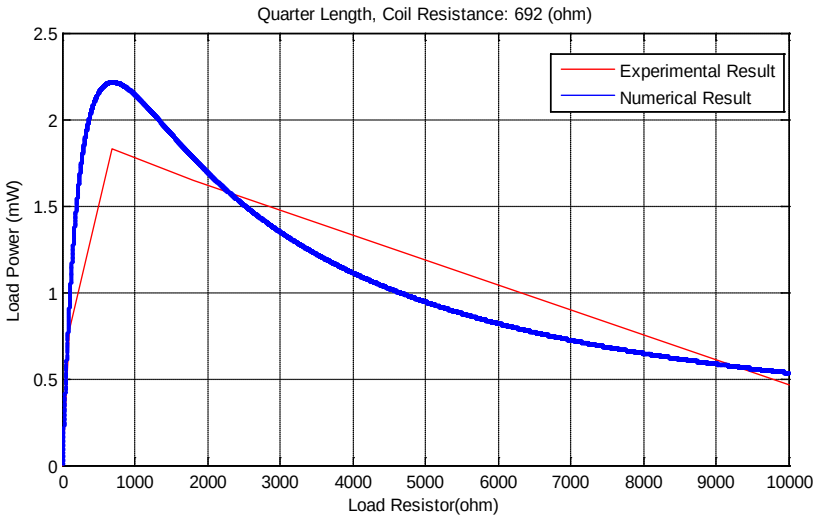

Figure 31. Comparison between numerical analysis and experimental result for load powers with respect to variable load resistors when iron cylinder has quarter of its primary length

Finally, based on the impedance matching, the maximum power in the case when coil resistance is 20.4 [Ω] is equal to:

$$P_{\max} = \frac{(0.182)^2}{20} = 1.656[mW].$$

Comparing these results to the case when the iron cylinder had its primary length, it can be concluded that when the coil resistance is 692 [Ω], the maximum harvested power has increased by the factor 4.342, which is almost equal to square of the factor that induced voltage has been increased $(2.23)^2$, while when the coil resistance is 20.4 [Ω], the maximum harvested power has increased by the factor 4.988, which is almost equal to square of the factor that induced voltage has been increased $(2.35)^2$.

3.3.6. Parameter study of energy harvester when iron cylinder has one fifth of its primary length

Same as before, since the primary length of iron cylinder is 70 [mm], therefore one fifth of its length is 14 [mm]. In this section, again all the experimental steps which have been done in previous sections are going to be repeated. The following figure

illustrates the effect of slope at the end of iron cylinder on induced voltage when the coil resistance is 692 [Ω]:

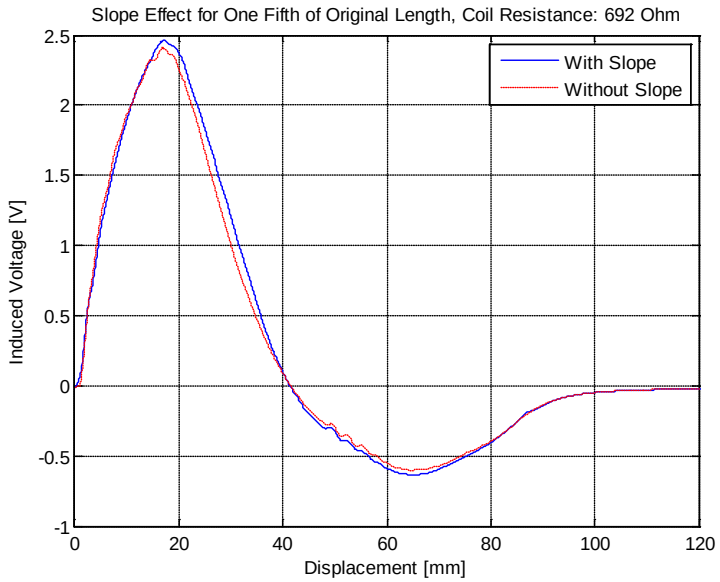

Figure 32. Effect of slope at the end of iron cylinder on induced voltage when iron cylinder has the one fifth of its primary length

Again, based on figure above, creating a slope at the end of iron cylinder will improve the amount of induced voltage about 0.1 [V].

Another interesting phenomenon which can be pointed out is the negative voltage's peak. This peak indicates that even when the direction of magnetic field is changed due to the design configuration, there is still another point on this area with opposite direction of magnetic field which has the strongest magnetic field intensity relative to its neighboring points. Although the intensity of this magnetic field is relatively low since this point is almost too far from the magnetic source.

In next step, the effect of coil resistance on induced voltage with respect to diverse velocities has been demonstrated below for both coils:

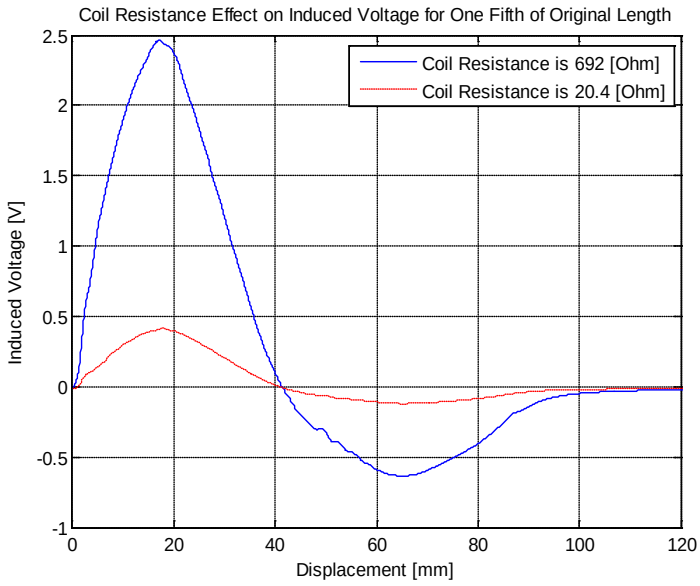

Figure 33. The coil resistance effect on induced voltage when iron cylinder has one fifth of its primary length

When the coil resistance is 20.4 [Ω], the maximum induced voltage which has been reached when the iron cylinder has the one fifth length of its primary length is 0.42 [V], while in similar case when the iron cylinder has its primary length, this maximum induced voltage was around 0.17 [V]. These measurements indicate that when the iron cylinder has been cut to its one fifth length, the induced voltage has increased by the factor 2.47. Similarly, when the coil resistance is 692 [Ω], the maximum induced voltage which has been reached when the iron cylinder has the one fifth length of its primary length is 2.45 [V], while in similar case when the iron cylinder has its primary length, this maximum induced voltage was around 1.1 [V]. Again, these measurements indicate that when the iron cylinder has been cut to its one fifth length, the induced voltage has increased by the factor 2.23, which is in close agreement when the coil resistance is 20.4 [Ω].

In last step, the effect of coil resistance on harvested power with respect to diverse load resistors for both coils has been determined in following figure:

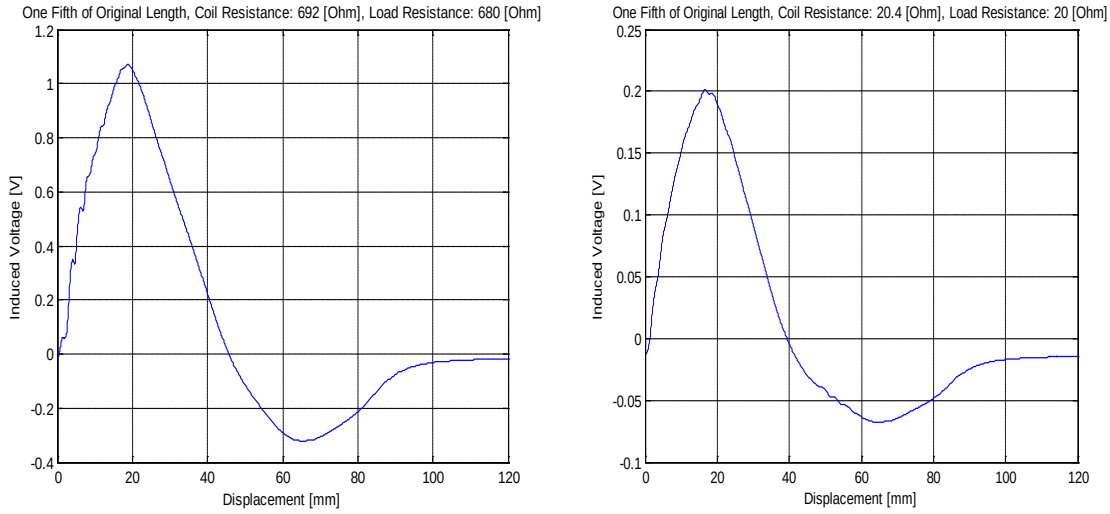

(a) (b)

Figure 34. The coil resistance effect on harvested power when iron cylinder has one fifth of its primary length: (a) coil resistance is 692 [Ω]; (b) coil resistance is 20.4 [Ω]

As the same procedure as previous sections, the maximum power when the coil resistance is 692 [Ω] is equal to: $P_{\max} = \frac{(1.120)^2}{680} = 1.845[mW]$.

Same as before, the following figure compares both powers which have been calculated experimentally and the power versus load resistor graph which has been obtained numerically.

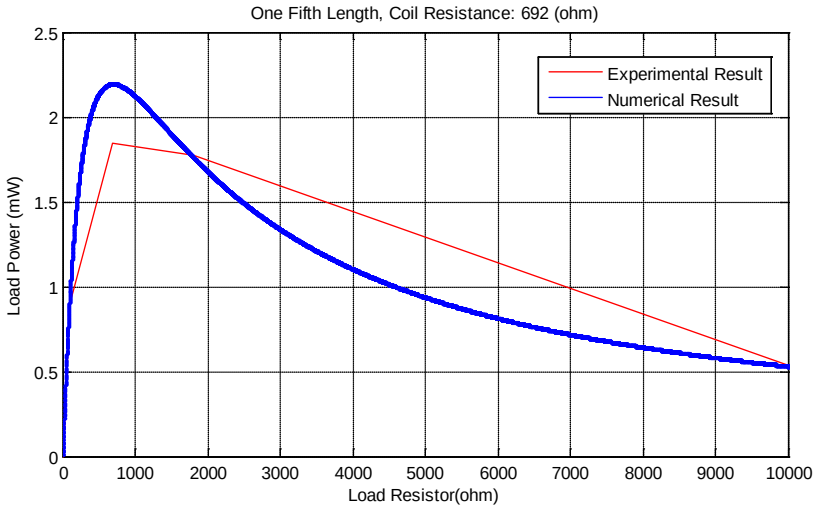

Figure 35. Comparison between numerical analysis and experimental result for load powers with respect to variable load resistors when iron cylinder has one fifth of its primary length

In other coil (coil resistance is 20.4 [Ω]), the maximum power is equal to:

$$P_{\max} = \frac{(0.200)^2}{20} = 2.000[mW].$$

Comparing these results to the case when the iron cylinder had its primary length, it can be concluded that when the coil resistance is 692 [Ω], the maximum harvested power has increased by the factor 4.382, which is almost equal to square of the factor that induced voltage has been increased $(2.23)^2$, while when the coil resistance is 20.4 [Ω], the maximum harvested power has increased by the factor 6.024, which is almost equal to square of the factor that induced voltage has been increased $(2.47)^2$.

3.3.7. Parameter study of energy harvester when iron cylinder has one sixth of its primary length

As the final length to be tested (11.67 [mm]), again all the experimental steps which have been done in previous sections are going to be repeated. The following

figure illustrates the effect of slope at the end of iron cylinder on induced voltage when the coil resistance is 692 [Ω]:

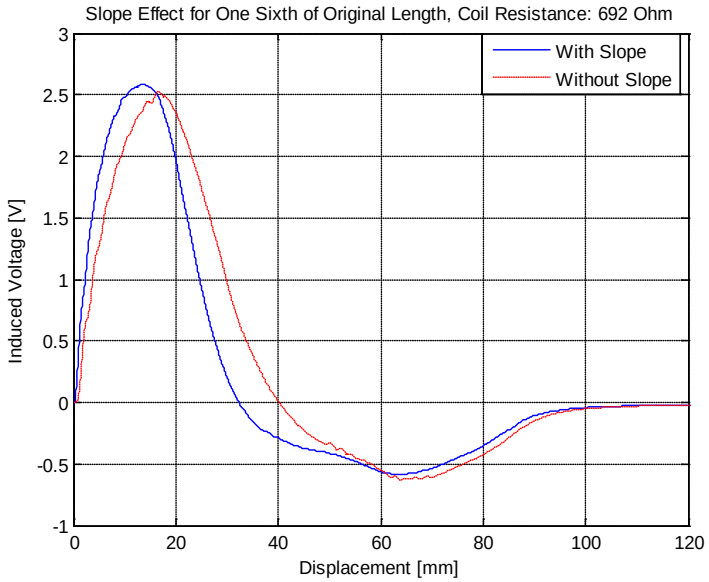

Figure 36. Effect of slope at the end of iron cylinder on induced voltage when iron cylinder has the one sixth of its primary length

Same as before and based on above figure, creating a slope at the end of iron cylinder will improve the amount of induced voltage about 0.1 [V].

In next level, the effect of coil resistance on induced voltage with respect to diverse velocities has been demonstrated below for both coils:

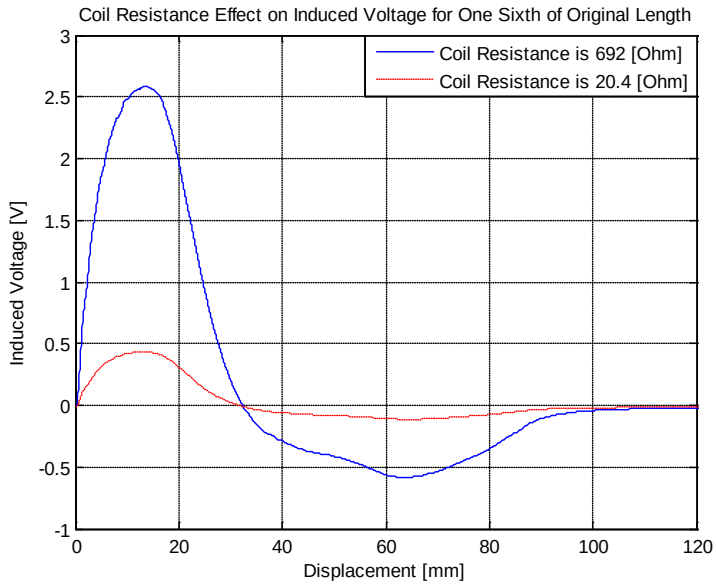

Figure 37. The coil resistance effect on induced voltage when iron cylinder has one sixth of its primary length

When the coil resistance is 20.4 [Ω], the maximum induced voltage which has been reached when the iron cylinder has the one sixth length of its primary length is 0.43 [V], while in similar case when the iron cylinder has its primary length, this maximum induced voltage was around 0.17 [V]. These measurements indicate that when the iron cylinder has been cut to its one sixth length, the induced voltage has increased by the factor 2.53. Similarly, when the coil resistance is 692 [Ω], the maximum induced voltage which has been reached when the iron cylinder has the one sixth length of its primary length is 2.6 [V], while in similar case when the iron cylinder has its primary length, this maximum induced voltage was around 1.1 [V]. Again, these measurements indicate that when the iron cylinder has been cut to its one sixth length, the induced voltage has increased by the factor 2.36, which is in close agreement when the coil resistance is 20.4 [Ω].

In last part, the effect of coil resistance on harvested power with respect to diverse load resistors for both coils has been determined in following figure:

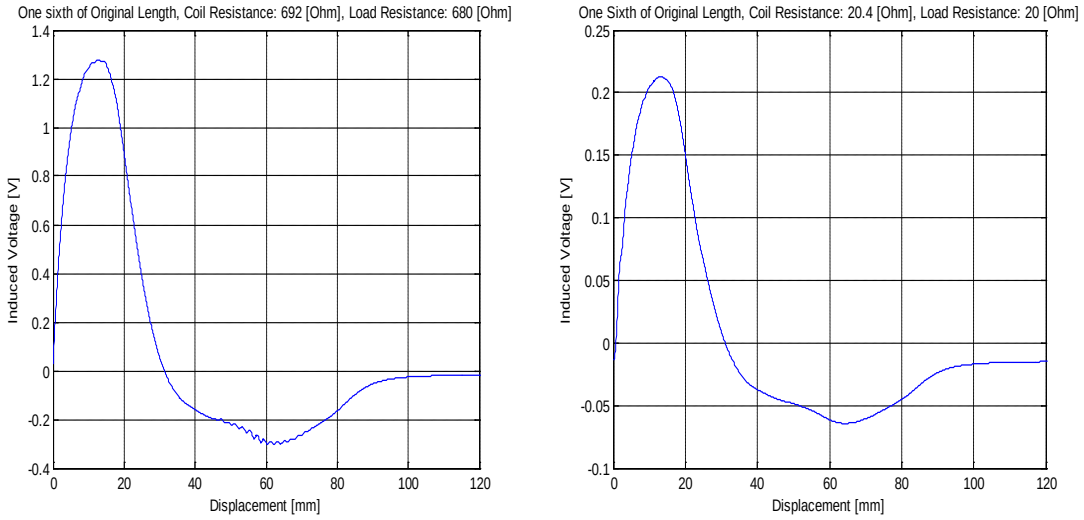

Figure 38. The coil resistance effect on harvested power when iron cylinder has one sixth of its primary length: (a) coil resistance is 692 [Ω]; (b) coil resistance is 20.4 [Ω]

In the case when coil resistance is 692 [Ω], the maximum power is equal to:

$$P_{\max} = \frac{(1.275)^2}{680} = 2.391[mW].$$

Same as previous sections, figure (39) compares both powers which have been calculated experimentally and the power versus load resistor graph which has been obtained numerically.

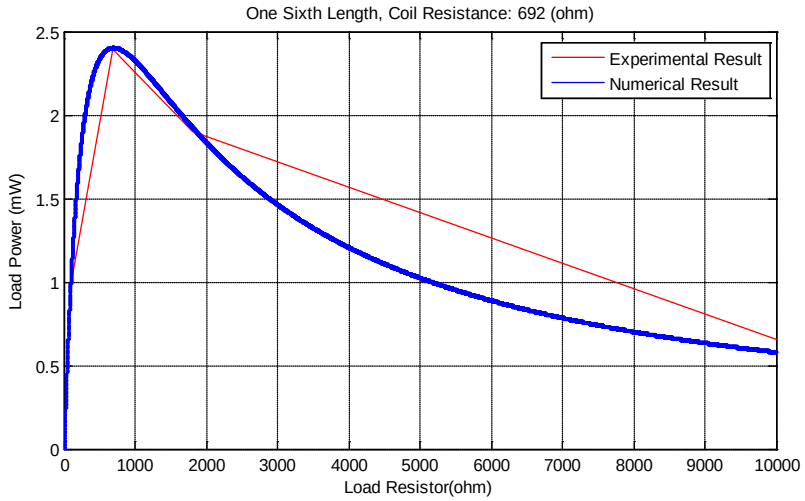

Figure 39. Comparison between numerical analysis and experimental result for load powers with respect to variable load resistors when iron cylinder has one sixth of its primary length

Finally when the coil resistance is 20.4 [Ω], the maximum power in this case is equal to:

$$P_{\max} = \frac{(0.212)^2}{20} = 2.247[mW].$$

Comparing these results to the case when the iron cylinder had its primary length, it can be concluded that when the coil resistance is 692 [Ω], the maximum harvested power has increased by the factor 5.679, which is almost equal to square of the factor that induced voltage has been increased $(2.36)^2$, while when the coil resistance is 20.4 [Ω], the maximum harvested power has increased by the factor 6.768, which is almost equal to square of the factor that induced voltage has been increased $(2.53)^2$.

3.3.8. Parameter study of energy harvester when there is no iron cylinder

To complete the discussion about the length effect of iron cylinder on induced voltage and harvested power, it is needed to test the setup without iron cylinder (the

length is zero in this case). First of all, the coil resistance effect on induced voltage with respect to diverse velocities has been examined for both coils:

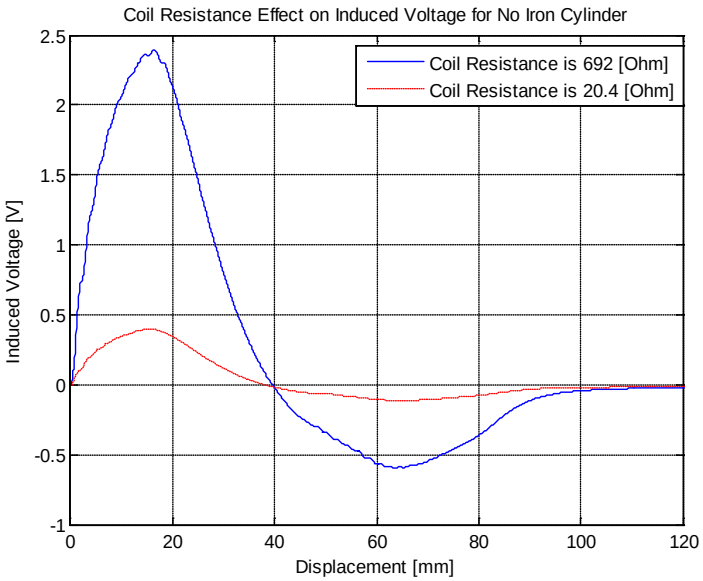

Figure 40. The coil resistance effect on induced voltage when there is no iron cylinder

When the coil resistance is 20.4 [Ω], the maximum induced voltage which has been reached when there is no iron cylinder is 0.39 [V], while in similar case when the iron cylinder has its primary length, this maximum induced voltage was around 0.17 [V]. These measurements indicate that when there is no iron cylinder, the induced voltage has increased by the factor 2.29. Similarly, when the coil resistance is 692 [Ω], the maximum induced voltage which has been reached when there is no iron cylinder is 2.35 [V], while in similar case when the iron cylinder has its primary length, this maximum induced voltage was around 1.1 [V]. Again, these measurements indicate that when there is no iron cylinder, the induced voltage has increased by the factor 2.14, which is in close agreement when the coil resistance is 20.4 [Ω].

The final step of experimental analysis in this section has been conducted to examine the coil resistance effect on harvested power with respect to diverse load resistors for both coils:

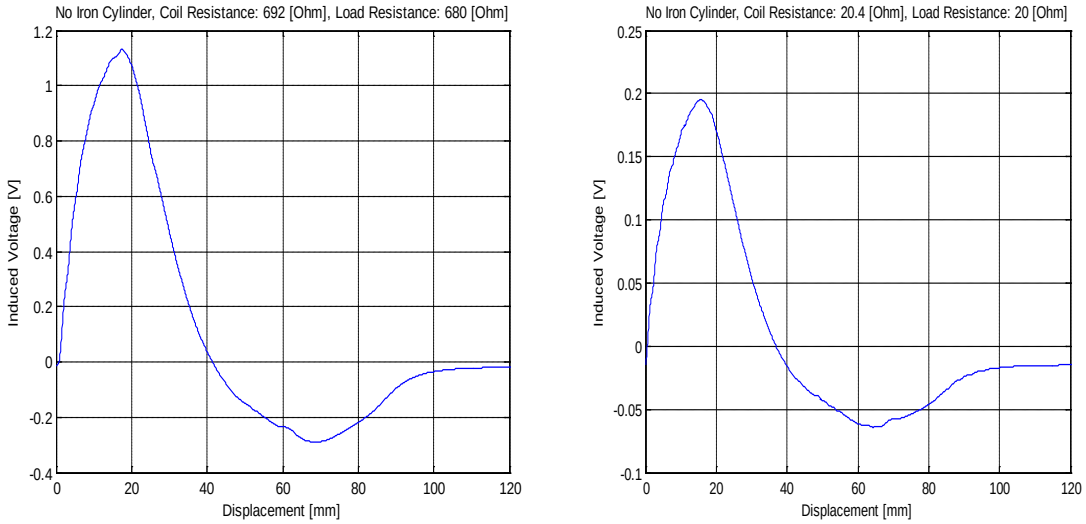

Figure 41. The coil resistance effect on harvested power when there is no iron cylinder: (a) coil resistance is 692 [Ω]; (b) coil resistance is 20.4 [Ω]

When coil resistance is 692 [Ω], based on above figure, the maximum power is equal to: $P_{\max} = \frac{(1.130)^2}{680} = 1.878[mW]$.

Now, just like every other sections in this chapter, figure (42) compares both powers which have been calculated experimentally and the power versus load resistor graph which has been obtained numerically.

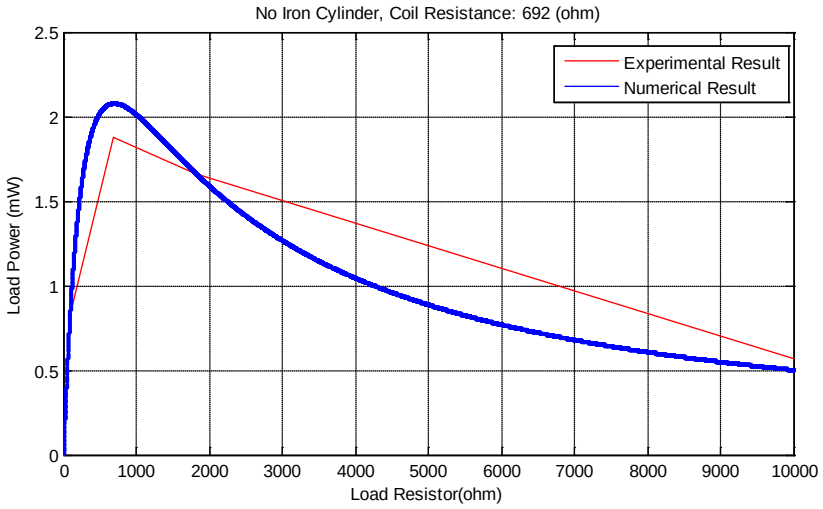

Figure 42. Comparison between numerical analysis and experimental result for load powers with respect to variable load resistors when there is no iron cylinder

When the coil resistance is 20.4 [Ω], based on figure (41), the maximum power in this case is equal to:

$$P_{\max} = \frac{(0.198)^2}{20} = 1.960[mW].$$

Comparing these results to the case when the iron cylinder had its primary length, it can be concluded that when the coil resistance is 692 [Ω], the maximum harvested power has increased by the factor 4.461, which is almost equal to square of the factor that induced voltage has been increased $(2.14)^2$, while when the coil resistance is 20.4 [Ω], the maximum harvested power has increased by the factor 5.904, which is almost equal to square of the factor that induced voltage has been increased $(2.29)^2$.

3.3.9. Conclusion

Based on all the steps which have been conducted so far in this chapter, the following graphs demonstrate the maximum voltage and maximum power versus the diverse lengths of iron cylinder which have been tested to determine the optimum length

for the energy harvesting setup. (For illustrating the following graphs, the speed of moving coil is considered to be 70 [mm/s]).

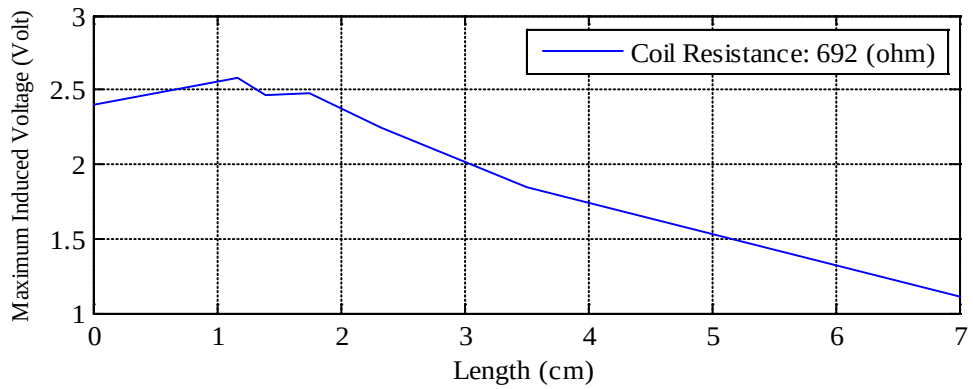

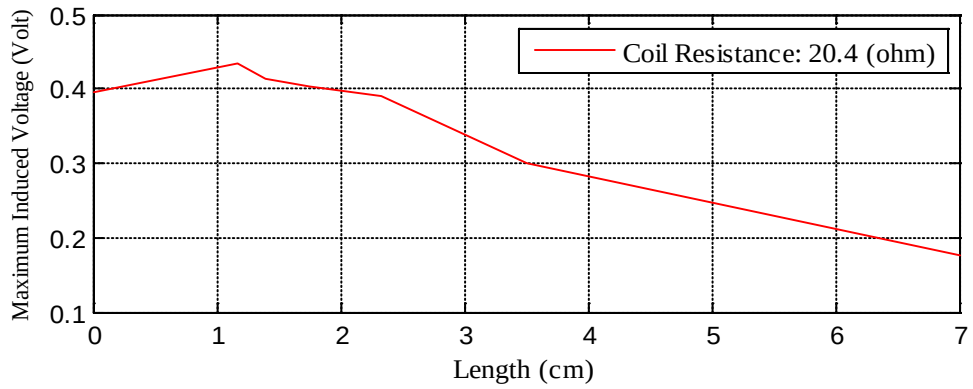

(a)

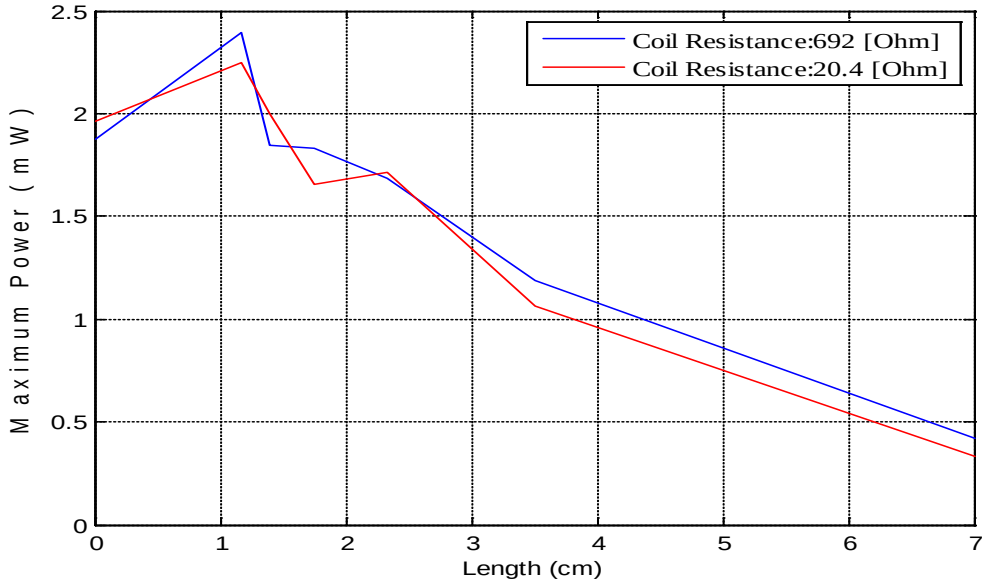

(b)

Figure 43. The induced voltage and harvested power based on diverse lengths of iron cylinder: (a) induced voltage for both coils; (b) harvested power for both coils

Based on this figure, the optimum length for iron cylinder in respect to inducing maximum voltage and retrieving maximum power from electromagnetic energy harvester is about 1.167 [cm]. Moreover, it can be seen that the general behavior of both coils are in close agreement with each other. Although the coil with higher resistance produces much more voltage comparing to the coil with lower resistance, but the harvested power on load resistors for both coils are almost the same as each other and generally the coil with higher resistance harvests power slightly more than the coil with lower resistance.

3.4. Experimental analysis when the iron core has no tooth-shape edges

As discussed earlier in simulation analysis, when the iron core has no tooth-shape edges, the magnetic flux density (*B*) losses outside the energy harvester setup are low and the density of magnetic fluxes inside iron core is high compare to when the iron core has the tooth-shape edges. Therefore, the magnetic field in air gap between iron core and iron cylinder is stronger when the iron core has no tooth-shape edges. This concept has been tested experimentally for verification in following subsections.

3.4.1. Parameter study of energy harvester when iron cylinder has its primary length (iron core has no tooth-shape edges)

In this subsection, all of the experimental steps which have been conducted in subsection (3.3.2) have been repeated again to demonstrate the effect of removing tooth-shape edges from iron core experimentally. First, the coil resistance effect on induced voltage with respect to diverse velocities has been examined for both coils:

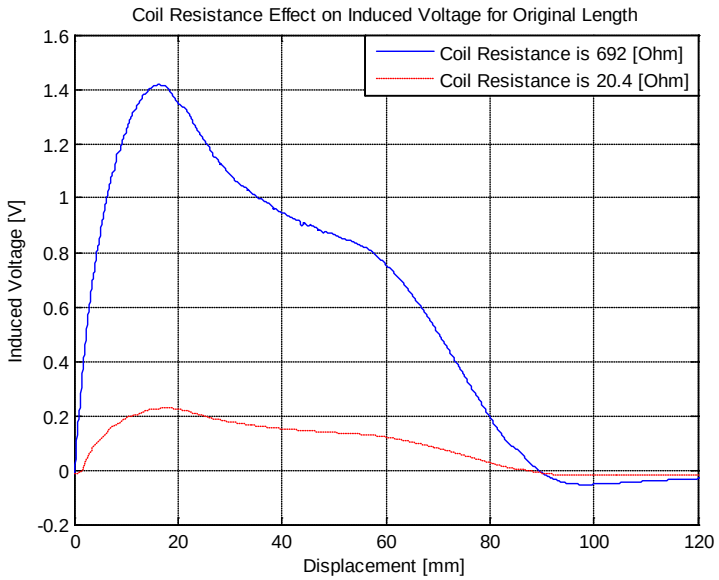

Figure 44. The coil resistance effect on induced voltage when iron core has no tooth-shape edges

This figure along with figure (16) can be used to verify the simulation analysis on improvement percentage factor, which has been conducted in subsection 3.2.3, with experimental results. Since the only parameter which has been changed in this part is the tooth-shape edges of iron core, and considering the case when velocity of the moving coil is 70 [mm/s] and the coil resistance is 20.4 [Ω], therefore the improvement percentage factor equals:

$$\alpha = \frac{0.21 - 0.17}{0.17} \times 100 = +23.53\% \qquad (46)$$

which is in close agreement with simulation analysis, when the tooth-shape edges have been removed from iron core (%25.469).

Moreover, compare to the same iron cylinder length but when iron core had the tooth-shape edges, in the case when the coil resistance is 20.4 [Ω], the maximum induced voltage which has been reached was 0.17 [V], while in this case the maximum induced voltage is around 0.21 [V]. These measurements indicate that with removing the tooth-shape edges, the induced voltage has increased by the factor 1.23. Similarly, in the case of coil resistance is 692 [Ω], the maximum induced voltage which has been

reached when iron cylinder had the same length but the iron core had the tooth-shape edges was 1.1 [V], while in the case in this subsection, this maximum induced voltage is around 1.42 [V]. Again, these measurements indicate that with removing the tooth-shape edges, the induced voltage has increased by the factor of 1.29, which is in close agreement with the case when the coil resistance is 20.4 [Ω].

Then, the coil resistance effect on harvested power with respect to diverse load resistors for both coils has been examined:

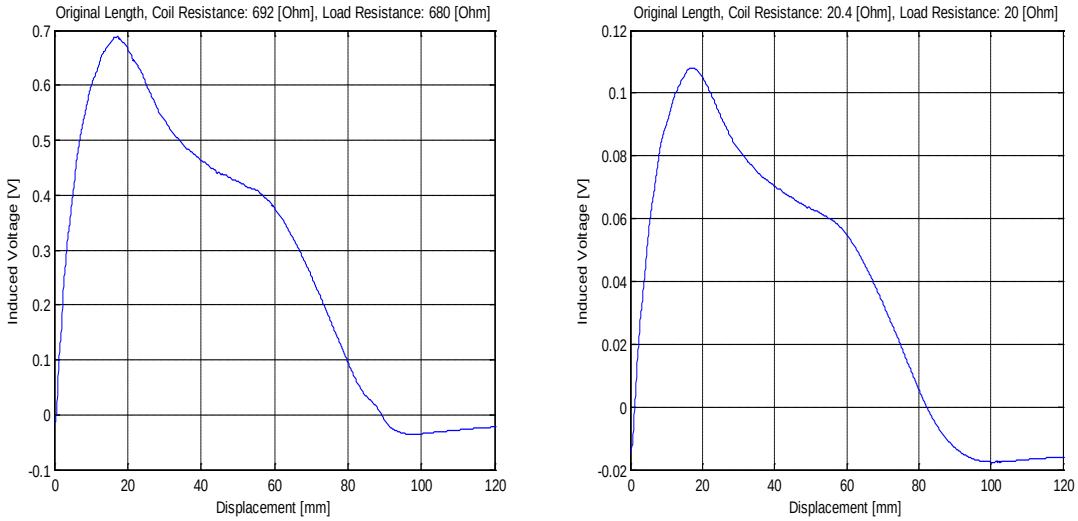

Figure 45. The coil resistance effect on harvested power when iron core has no tooth-shape edges: (a) coil resistance is 692 [Ω]; (b) coil resistance is 20.4 [Ω]

When the coil resistance is 692 [Ω], the maximum power is equal to:

$$P_{\max}=\frac{(0.685)^2}{680}=0.690[mW].$$

Same as before, figure (46) compares both powers which have been calculated experimentally and the power versus load resistor graph which has been obtained numerically.

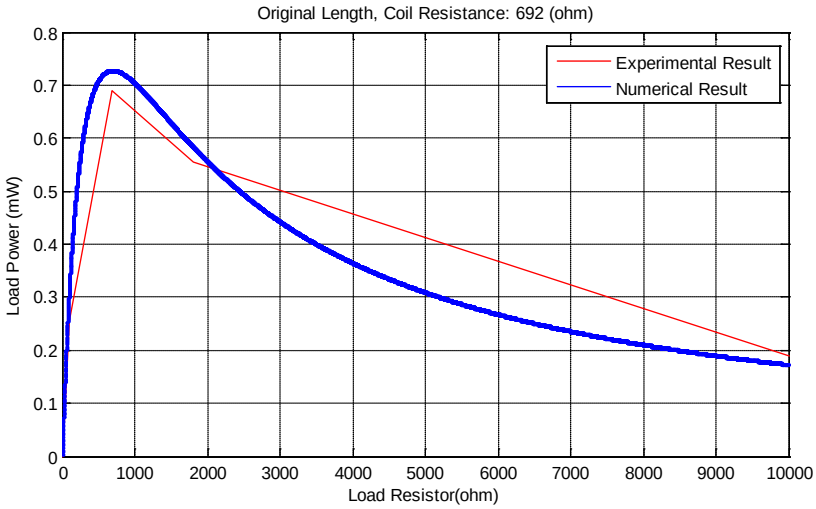

Figure 46. Comparison between numerical analysis and experimental result for load powers with respect to variable load resistors when iron core has no tooth-shape edges

But when the coil resistance is 20.4 [Ω], the maximum power in this case is equal to:

$$P_{\max}=\frac{(0.108)^2}{20}=0.583[mW].$$

Comparing these results to the case when the iron cylinder had the same length but the iron core had the tooth-shape edges, it can be concluded that when the coil resistance is 692 [Ω], the maximum harvested power has increased by the factor 1.639, which is almost equal to square of the factor that induced voltage has been increased $(1.29)^2$, while when the coil resistance is 20.4 [Ω], the maximum harvested power has increased by the factor 1.756, which is also almost equal to square of the factor that induced voltage has been increased in that case $(1.23)^2$.

3.4.2. Parameter study of energy harvester when iron cylinder has one sixth length of its primary length (iron core has no tooth-shape edges)

This time, all of the experimental steps which have been conducted in subsection (3.3.7) have been repeated here again to demonstrate the effect of removing tooth-

shape edges from iron core experimentally. First of all, the effect of slope at the end of iron cylinder on induced voltage when the coil resistance is 692 [Ω] has been illustrated in following figure:

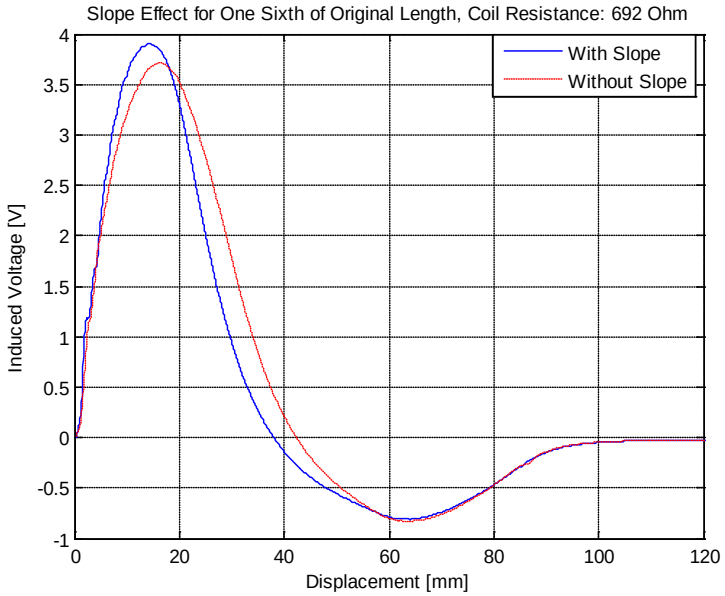

Figure 47. Effect of slope at the end of iron cylinder on induced voltage when iron cylinder has the one sixth of its primary length and iron core has no tooth-shape edges

In this case, when iron core has no tooth-shape edges and based on above figure, creating a slope at the end of iron cylinder will improve the amount of induced voltage about 0.2 [V]. This indicates that when the magnetic flux density (*B*) is stronger in the air gap between iron core and iron cylinder, then creating the slope at the end of iron cylinder will have more impact on induced voltage.

In the second part, the effect of coil resistance on induced voltage with respect to diverse velocities has been demonstrated below for both coils:

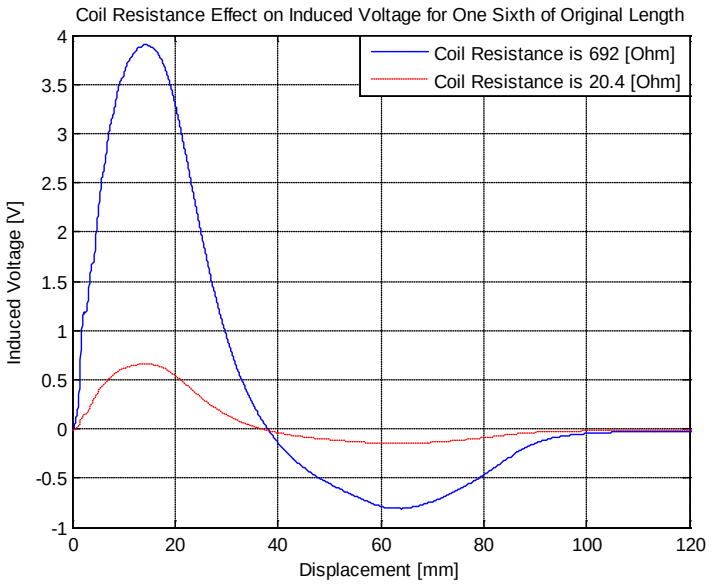

Figure 48. The coil resistance effect on induced voltage when iron core has no tooth-shape edges and iron cylinder has one sixth of its primary length

Comparing the same iron cylinder length (11.67 [mm]) but when iron core had the tooth-shape edges, in the case when the coil resistance is 20.4 [Ω], the maximum induced voltage which has been reached was 0.43 [V], while in this case the maximum induced voltage is around 0.66 [V]. These measurements indicate that with removing the tooth-shape edges, the induced voltage has increased by the factor 1.53. Similarly, in the case of coil resistance is 692 [Ω], the maximum induced voltage which has been reached when iron cylinder had the same length but the iron core had the tooth-shape edges was 2.6 [V], while in the case in this subsection, this maximum induced voltage is around 3.85 [V]. Again, these measurements indicate that with removing the tooth-shape edges, the induced voltage has increased by the factor of 1.48, which is in close agreement with the case when the coil resistance is 20.4 [Ω].

Lastly, the coil resistance effect on harvested power with respect to diverse load resistors for both coils has been examined:

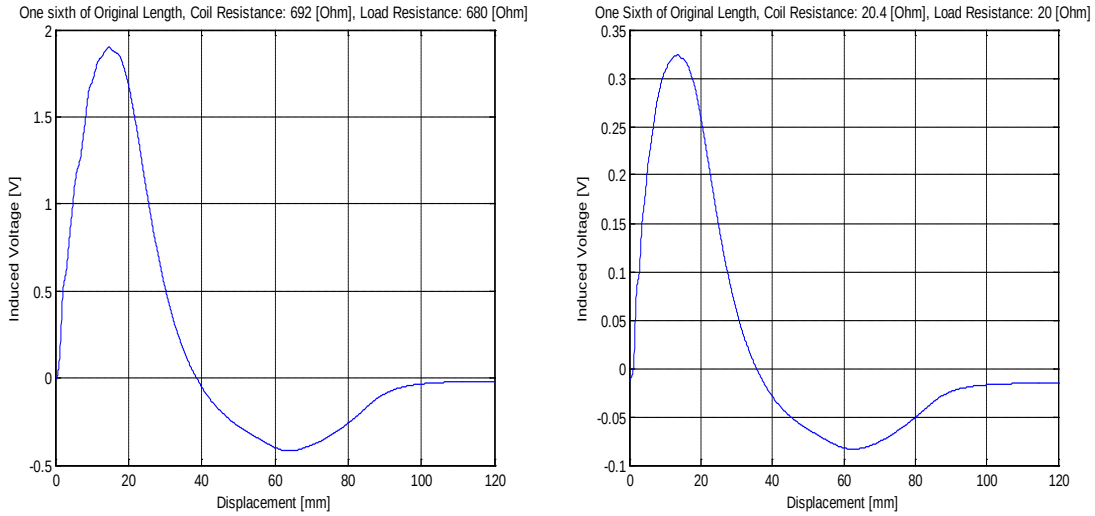

Figure 49. The coil resistance effect on harvested power when iron core has no tooth-shape edges and iron cylinder has one sixth of its primary length: (a) coil resistance is 692 [Ω]; (b) coil resistance is 20.4 [Ω]

When the coil resistance is 692 [Ω], the maximum power is equal to:

$$P_{\max} = \frac{(1.902)^2}{680} = 5.320[mW].$$

Moreover, figure (50) compares both powers which have been calculated experimentally and the power versus load resistor graph which has been obtained numerically.

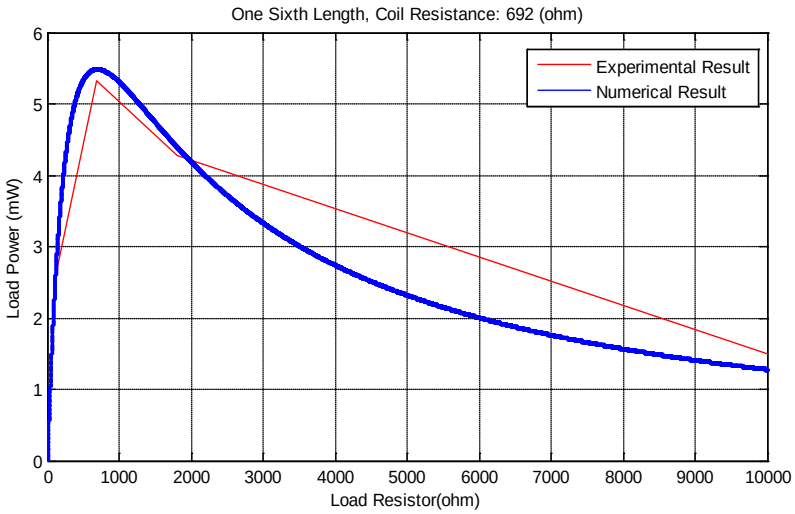

Figure 50. Comparison between numerical analysis and experimental result for load powers with respect to variable load resistors when iron core has no tooth-shape edges and iron cylinder has one sixth of its primary length

Finally, when the coil resistance is 20.4 [Ω], the maximum power in this case is equal to:

$$P_{\max} = \frac{(0.323)^2}{20} = 5.216[mW].$$

Comparing these results to the case when the iron cylinder had the same length but the iron core had the tooth-shape edges, it can be concluded that when the coil resistance is 692 [Ω], the maximum harvested power has increased by the factor 2.225, which is almost equal to square of the factor that induced voltage has been increased $(1.48)^2$, while when the coil resistance is 20.4 [Ω], the maximum harvested power has increased by the factor 2.321, which is also almost equal to square of the factor that induced voltage has been increased in that case $(1.53)^2$.

3.4.3. Parameter study of energy harvester when there is no iron cylinder (iron core has no tooth-shape edges)

As the final experimental subsection, all of the experimental steps which have been conducted in subsection (3.3.8) have been repeated again to demonstrate the

effect of removing tooth-shape edges from iron core experimentally. First, the coil resistance effect on induced voltage with respect to diverse velocities has been examined for both coils:.

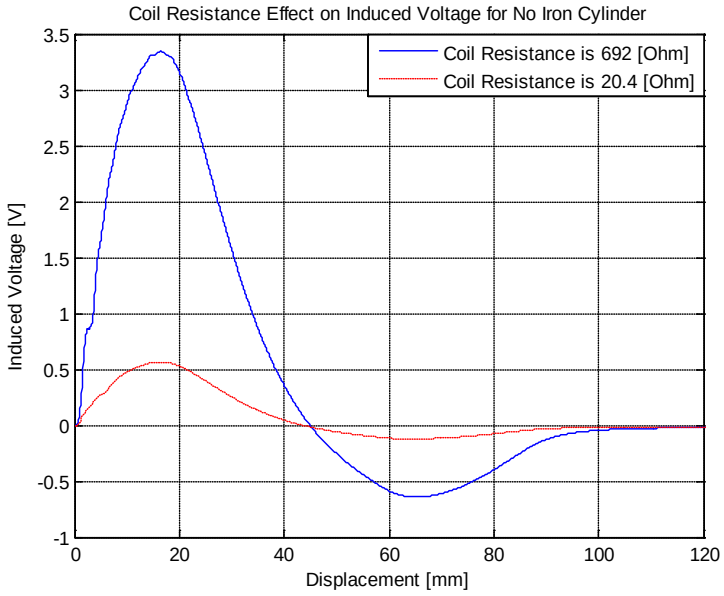

Figure 51. The coil resistance effect on induced voltage when iron core has no tooth-shape edges and there is no iron cylinder

Again, compare to the no iron cylinder case but when iron core had the tooth-shape edges, in the case when the coil resistance is 20.4 [Ω], the maximum induced voltage which has been reached was 0.39 [V], while in this case the maximum induced voltage is around 0.56 [V]. These measurements indicate that with removing the tooth-shape edges, the induced voltage has increased by the factor 1.44. Similarly, in the case of coil resistance is 692 [Ω], the maximum induced voltage which has been reached when iron cylinder had the same length but the iron core had the tooth-shape edges was 2.35 [V], while in the case in this subsection, this maximum induced voltage is around 3.35 [V]. Again, these measurements indicate that with removing the tooth-shape edges, the induced voltage has increased by the factor of 1.42, which is in close agreement with the case when the coil resistance is 20.4 [Ω].

Then, the coil resistance effect on harvested power with respect to diverse load resistors for both coils has been examined:

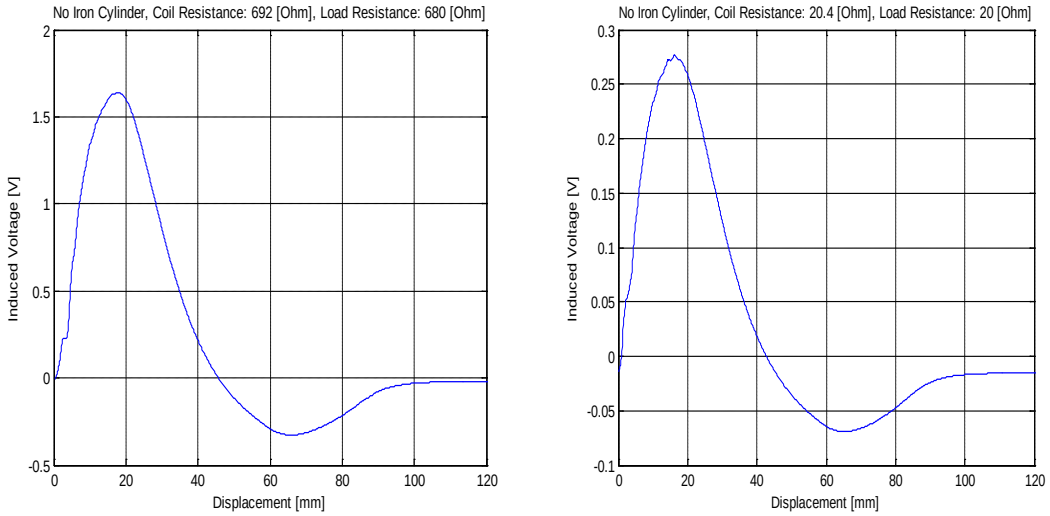

Figure 52. The coil resistance effect on harvested power when iron core has no tooth-shape edges and there is no iron cylinder: (a) coil resistance is 692 [Ω]; (b) coil resistance is 20.4 [Ω]

Based on the impedance matching, when the coil resistance is 692 [Ω], the maximum power is equal to: $P_{\max} = \frac{(1.640)^2}{680} = 3.955[mW]$.

Same as before, figure (53) compares both powers which have been calculated experimentally and the power versus load resistor graph which has been obtained numerically.

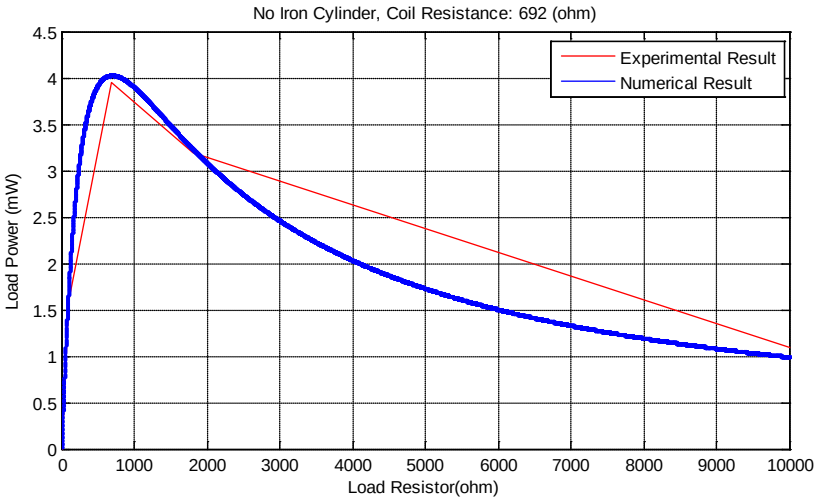

Figure 53. Comparison between numerical analysis and experimental result for load powers with respect to variable load resistors when iron core has no tooth-shape edges and there is no iron cylinder

At last, when the coil resistance is 20.4 [Ω], the maximum power in this case is equal to:

$$P_{\max} = \frac{(0.275)^2}{20} = 3.781[mW].$$

Comparing these results to the case when there was no iron cylinder and the iron core had the tooth-shape edges, it can be concluded that when the coil resistance is 692 [Ω], the maximum harvested power has increased by the factor 2.106, which is almost equal to square of the factor that induced voltage has been increased $(1.42)^2$, while when the coil resistance is 20.4 [Ω], the maximum harvested power has increased by the factor 1.929, which is also almost equal to square of the factor that induced voltage has been increased in that case $(1.44)^2$.

3.4.4. Conclusion

Based on all the steps which have been taken in this section, the following graphs demonstrate the maximum voltage and maximum power versus the diverse lengths of iron cylinder to determine the optimum length for the energy harvesting setup.

(For illustrating the following graphs, the speed of moving coil is considered to be 70 [mm/s]).

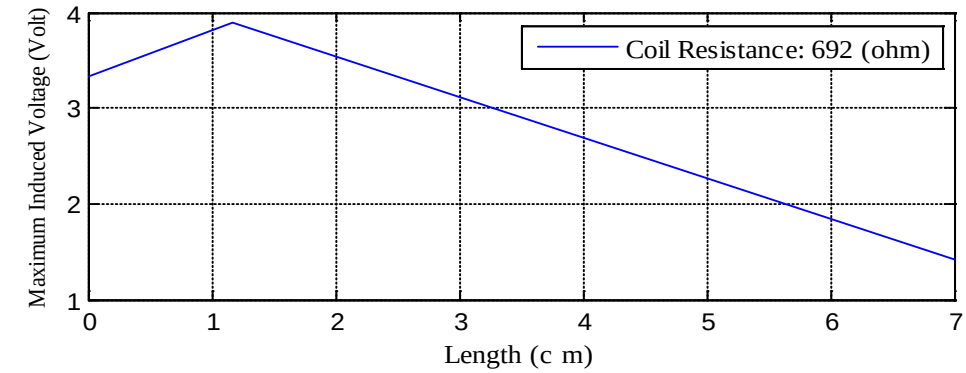

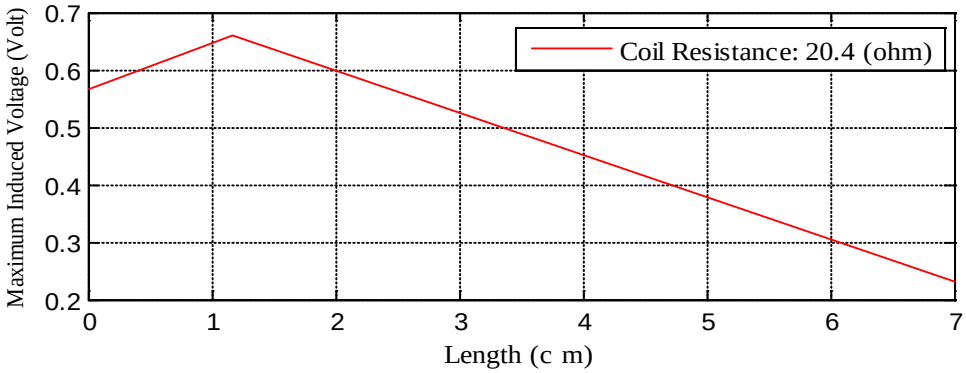

(a)

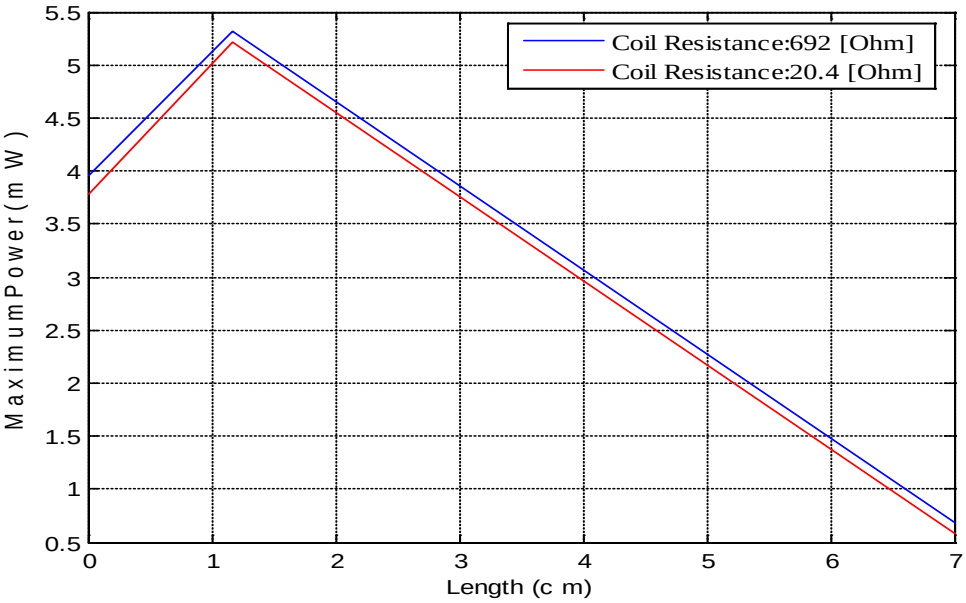

(b)

Figure 54. The induced voltage and harvested power based on diverse lengths of iron cylinder when iron core has no tooth-shape edges: (a) induced voltage for both coils; (b) harvested power for both coils

Again, based on above figure, the optimum length for iron cylinder in respect to inducing maximum voltage and retrieving maximum power from electromagnetic energy harvester is about 1.167 (cm), which verifies the other set of experimental tests that have been conducted in section three of this chapter. Moreover, it can be seen that the general behavior of both coils are in close agreement with each other. Although the coil with higher resistance produces much more voltage comparing to the coil with lower resistance, but the harvested power on load resistors for both coils are almost the same as each other and generally the coil with higher resistance harvests power slightly more than the coil with lower resistance. Finally, comparing this figure to figure (43), it can be concluded that the maximum harvested power without tooth-shape edges on iron core is 5.320 [mW], which is enough amount to power sensors in condition monitoring for rotary applications, while this maximum harvested power when the iron core has the tooth-shape edges was 2.391 [mW]. Therefore, removing the tooth-shape edges from iron core has increased the harvested power by the factor of 2.225.

Analyzing the three design modifications through experimental tests which has been explained in sections 3.3 and 3.4 has been summarized in following tables:

Table 1. The effect of slope at the end of iron cylinder on induced voltage

The length of iron cylinder [mm]	*Induced voltage with slope [V]*	*Induced voltage without slope [V]*
	Iron core has tooth-shape edges	
35	1.8	1.6
23.33	2.2	2.1
17.5	2.45	2.35
14	2.45	2.35
11.67	2.6	2.5
	Iron core doesn't have tooth-shape edges	
11.67	3.9	3.7

Table 2. The effect of internal coil resistance on induced voltage

The length of iron cylinder [mm]	*Induced voltage when coil resistance is 692 ohm [V]*	*Induced voltage when coil resistance is 20.4 ohm [V]*
	Iron core has tooth-shape edges	
70	1.1	0.17
35	1.8	0.3
23.33	2.2	0.39
17.5	2.45	0.4
14	2.45	0.41
11.67	2.6	0.43
0	2.4	0.4
	Iron core doesn't have tooth-shape edges	
70	1.41	0.23
11.67	3.9	0.66
0	3.35	0.56

Table 3. The maximum harvested power for both coils

The length of iron cylinder [mm]	*Harvested power through optimum load resistor when coil resistance is 692 ohm [mW]*	*Harvested power through optimum load resistor when coil resistance is 20.4 ohm [mW]*
	Iron core has tooth-shape edges	
70	0.421	0.332
35	1.191	1.066
23.33	1.684	1.711
17.5	1.828	1.656
14	1.845	2.000
11.67	2.391	2.247
0	1.878	1.960
	Iron core doesn't have tooth-shape edges	
70	0.690	0.583
11.67	5.320	5.216
0	3.955	3.781

4. One Degree of Freedom Electromagnetic Energy Harvester System for Rotary Motion

This chapter presents modeling and analysis of a voice coil energy harvester, which is mounted on a rotary flexible beam that can be used as an energy scavenger for rotary motion applications. The energy harvester system consists of a bimorph cantilever beam with a voice coil as the tip mass mounted on a rotating hub. Assuming Euler–Bernoulli beam equations and considering the effect of an electromagnetic transducer, equations of motion are derived using the Lagrangian approach followed by relationships describing the induced voltage. The equations provide a quantitative description of how the hub acceleration and gravity due to the tip mass contribute power to the energy harvester. Numerical simulations are performed to illustrate the performance of the harvester by obtaining tip velocities and amplitudes for a range of rotational speeds and to examine the effects of effective parameters on resonance frequency and induced voltage, such as the spring constant and the load mass. Finally, the experimental test has been done to demonstrate how much voltage can be collected by this method.

4.1. Mathematical Model of One Degree of Freedom Rotating Harvester

The electromagnetic energy harvester is the voice coil in the form of a speaker, which comprise of permanent magnet, spring, and magnetic coil. The speaker is mounted on one end of a cantilever beam. The other end of this cantilever beam is connected to a rotating hub. The hub rotates with a constant speed. The general schematic of the system is illustrated in following figure. To derive the mathematical model, the energy harvester system has been divided into two subsystems: mechanical subsystem and electrical subsystem. The main reason to create this division is that kinetic energy harvesters, such as this one degree of freedom voice coil speaker rotating harvester, require a transduction mechanism to generate electrical energy from motion

and the generator will require a mechanical system which couples environmental displacements to the transduction mechanism. Based on this explanation, the mechanical subsystem model relates the cantilever beam deflection to the relative displacement between magnetic coil and permanent magnet. The electrical subsystem model indicates the amount of induced voltage and harvested power in the moving coil. First, the coupled dynamic equations of the rotating flexible beam have been derived and then, the equation of generated electric voltage is derived.

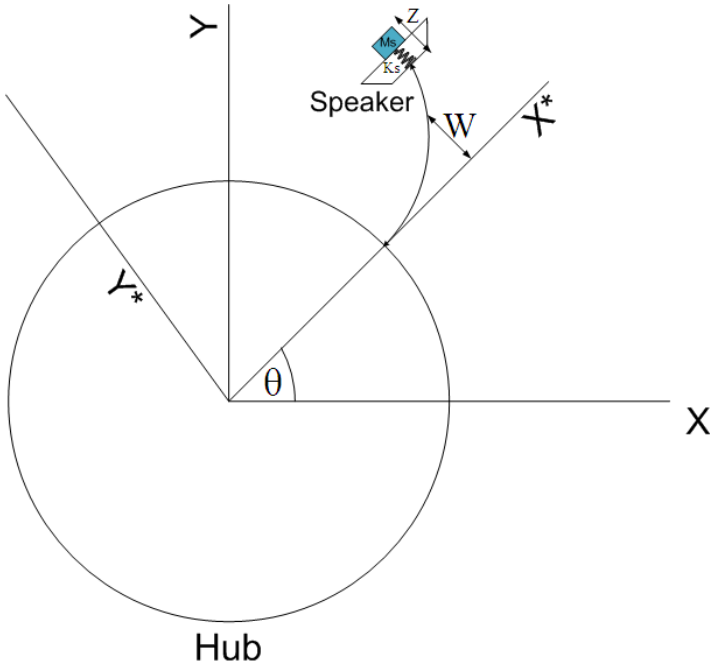

Figure 55. One degree of freedom system for harvesting energy from rotary motion application

4.1.1. Mechanical Subsystem Model

In the energy harvester system, the gravity force on electromagnetic part of the system (the speaker) and acceleration of the hub provide base excitation vibration for the beam. The Euler-Bernoulli beam equation describes the partial differential equation of vibrating beam as follows [60]:

$$EI\frac{\partial^4 w(\zeta,t)}{\partial\zeta^4}+\rho AL^4\frac{\partial^2 w(\zeta,t)}{\partial t^2}=0 \qquad (47)$$

where *w* is the deflection of the beam, ζ is the normalized position along the length of the beam, which means $\zeta = x/L$, *E* is the Young's modulus, *I* is the area moment of inertia, ρ is the mass density, and *A* is the cross sectional area of the beam.

Using the method of separation of variables, *w* can be solved as

$$w(\zeta,t) = f(\zeta).q(t) \qquad (48)$$

where $f(\zeta)$ and q(t) are the spatial and temporal coordinate systems. On the other hand,

$$f_i(\zeta) = a_1 \sin\beta\zeta + a_2 \cos\beta\zeta + a_3 \sinh\beta\zeta + a_4 \cosh\beta\zeta \qquad (49)$$

Equation (49) identifies the *ith* mode shape of the beam. The following boundary conditions of equation (47) can be considered for a clamped-free beam to determine the coefficients and β in equation (49):

$$f_i(\zeta)\Big|_{\zeta=0} = 0, \qquad \frac{df_i(\zeta)}{d\zeta}\Big|_{\zeta=0} = 0 \qquad (50)$$

$$\frac{d^2 f_i(\zeta)}{d\zeta^2}\Big|_{\zeta=1} = \frac{J_L\beta^4}{\rho AL^3}\frac{df_i(\zeta)}{d\zeta}\Big|_{\zeta=1} \qquad (51)$$

$$\frac{d^3 f_i(\zeta)}{d\zeta^3}\Big|_{\zeta=1} = -\frac{M_L\beta^4}{\rho AL} f_i(\zeta)\Big|_{\zeta=1} \qquad (52)$$

where M_L and J_L are the mass and inertia of the speaker, respectively. Using the above boundary conditions, the relation between the coefficients of equation (49) is as follows:

$$a_1 = -a_3, \quad a_2 = -a_4 \tag{53}$$

Moreover, the value of β can be obtained by solving the following equation:

$$\begin{aligned}&(1+\cos\beta\ \cosh\beta) - \mathrm{M}\beta(\sin\beta\cos\beta - \cos\beta\ \sinh\beta) - \\ &\mathrm{J}\beta^3(\sin\beta\ \cosh\beta + \cos\beta\sinh\beta) + \mathrm{MJ}\beta^4(1 - \cos\beta\cosh\beta) = 0\end{aligned} \tag{54}$$

where $M = M_L / \rho AL$ and $J = J_L / \rho AL^3$.

To derive a mathematical model that describes the energy harvester system, the Lagrangian formulation has been used:

$$\frac{d}{dt}\left(\frac{\partial T}{\partial \dot{p}_i}\right) - \frac{\partial T}{\partial p_i} + \frac{\partial U}{\partial p_i} = F_i \tag{55}$$

where *T* is the total kinetic energy, *U* is the total potential energy, F_i is the *ith* generalized force, and p_i is the *ith* generalized coordinate. The generalized force vector is given by $\mathrm{F} = \begin{bmatrix}0 & 0\end{bmatrix}^T$ and the generalized coordinate vector is chosen as $\mathrm{p} = \begin{bmatrix}\mathrm{q} & \mathrm{z}\end{bmatrix}^T$, where *z* is the relative displacement between magnetic coil and permanent magnet.

To obtain the total kinetic energy of the energy harvester system, first we need to calculate the kinetic energy of different components of the system. The kinetic energy of the beam is given by:

$$T_{beam} = \frac{1}{2} J_b \dot{\theta}^2 + \frac{1}{2}\int_{beam} (\dot{w}^2 + 2\dot{w}x\dot{\theta}) dm \tag{56}$$

where J_b is the beam inertia.

For the electromagnetic part (the speaker), x = L, w(x,t) = w(L,t), and $\dot{w}(x,t) = \dot{w}(L,t)$. Since for the electromagnetic part, the kinetic energy is comprised of translational and rotational components, therefore:

$$T_{Translational} = \frac{1}{2}M[\dot{\theta}^2 {w_e}^2 + (\dot{w}_e + L\dot{\theta})^2] + \frac{1}{2}m[\dot{\theta}^2(w_e + z)^2 + (\dot{w}_e + \dot{z} + L\dot{\theta})^2] \quad (57)$$

$$T_{rotational} = \frac{1}{2}J_l(\dot{\theta} + \frac{\partial \dot{w}_e}{\partial x})^2 \quad (58)$$

The total kinetic energy of the harvester system is equal to the summation of all three above kinetic energies, which means:

$$T_{Total} = T_{beam} + T_{Translational} + T_{rotational} \quad (59)$$

The expression for the total potential energy (*U*) is as follows:

$$\begin{aligned} U = {} & \int_0^L \frac{EI}{2}(\frac{\partial^2 w}{\partial x^2})^2 dx + g\rho A\int_0^L (\frac{w}{\cos\theta} + (x - w\tan\theta)\sin\theta)dx + \\ & Mg(\frac{w_e}{\cos\theta} + L\sin\theta - w\tan\theta\sin\theta) + \\ & mg(\frac{w_e}{\cos\theta} + \frac{z}{\cos\theta} + L\sin\theta - w\tan\theta\sin\theta - z\tan\theta\sin\theta) + \frac{1}{2}k_s(w+z)^2 \end{aligned} \quad (60)$$

Finally, the dynamic equations of the beam can be presented in matrix form as follows:

$$M\begin{bmatrix}\ddot{q}\\ \ddot{z}\end{bmatrix} + C\begin{bmatrix}\dot{q}\\ \dot{z}\end{bmatrix} + K\begin{bmatrix}q\\ z\end{bmatrix} + S = \begin{bmatrix}0\\ 0\end{bmatrix} \quad (61)$$

where:

$$M = \begin{bmatrix} \rho AL\int_0^1 f^2(\xi)d\xi + M_L f^2 + \frac{J_L}{L^2} f'^2 & mf \\ mf & m \end{bmatrix} \qquad (62)$$

$$C = \begin{bmatrix} (c_b + c_m) f^2 & c_m f \\ c_m f & c_m \end{bmatrix} \qquad (63)$$

$$K = \begin{bmatrix} \frac{EI}{L^3}\int_0^1 f''^2(\xi)d\xi - M_L\dot{\theta}^2 f^2 + k_s f^2 & -m\dot{\theta}^2 f + k_s f \\ -m\dot{\theta}^2 f + k_s f & -m\dot{\theta}^2 + k_s \end{bmatrix} \qquad (64)$$

$$S = \begin{bmatrix} M_L gf\cos\theta + g\rho AL\cos\theta\int_0^1 f(\xi)d\xi \\ mg\cos\theta \end{bmatrix} \qquad (65)$$

In the above equations, *m* is the mass of the voice coil, k_s is the spring constant, and c_b and c_m are the damping coefficients for the beam and for the voice coil, respectively.

4.1.2. Electrical Subsystem Model

The equation of motion for base excitation of second-order mass-spring-damper system is:

$$m\ddot{z}(t) + c_T\dot{z}(t) + kz(t) = -m\ddot{y}(t) \qquad (66)$$

where *y* is the base displacement, *z* is the relative displacement between permanent magnet and magnetic coil, *k* is the spring stiffness, *m* is the voice coil mass, and c_T is the total amount of damping. On the other hand, it has been discussed in chapter 2 that when a magnetic source, like permanent magnet, and a conductor, like coil, has a relative displacement with respect to each other, then based on Faraday's

law, there would be an induced voltage in conductor which can be calculated through following equation:

$$V = \int (u \times B).dl \qquad (67)$$

Suppose the magnetic flux density (*B*) is uniformed radial in the area of moving coil, and the coil moves perpendicular to the magnetic flux density (*B*) direction. Therefore, equation (67) can be rewritten as:

$$V = B.l.u \qquad (68)$$

where *l* and *u* are the length and velocity of the coil, respectively.

4.2. Numerical analysis of one degree of freedom rotating harvester

This section presents numerical results to evaluate the feasibility of the energy harvesting system for the rotary motion applications. By solving equations (61) and (68) simultaneously for variable *z*, the simulation result is as follows:

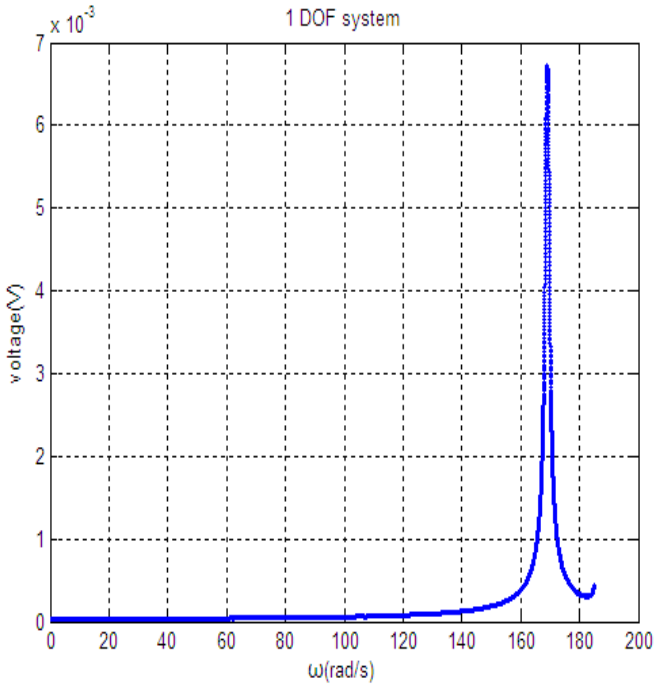

Figure 56. Frequency response of induced voltage which caused by relative displacement between permanent magnet and magnetic coil of voice coil speaker

Based on figure (56), the resonance frequency of voice coil speaker occurs at 170 [rad/s] and the maximum induced voltage is around 6.75 [mV], which is considerably low to harvest power from it.

Now, the effect of some effective parameters on frequency response has been examined. First of all, the effect of spring constant of the voice coil speaker on frequency response for three different spring constants has been simulated and the result is demonstrated in following figure:

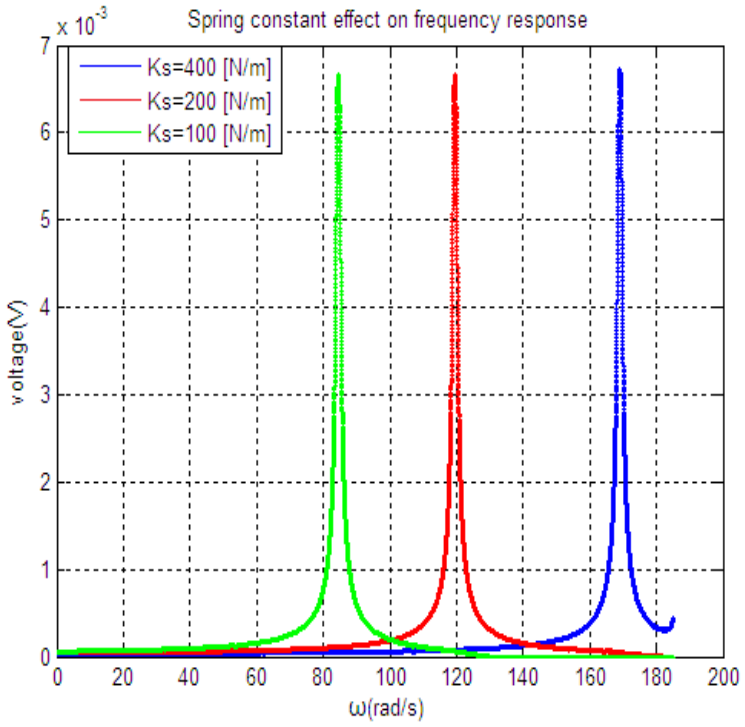

Figure 57. Spring constant effect on frequency response for one degree of freedom system

As it can be seen, softer springs will result in lower resonance frequencies as it expected. Moreover, it should be mention that the total load mass (voice coil speaker) comprises of the mass of the moving coil and spring inside speaker (M_s) and the mass of fixed magnet and the body of the speaker (M_r). The weight distribution between these two parts of the total mass will affect the frequency response of this one degree of freedom rotary electromagnetic energy harvester. The simulation result to analyze the effect of this mass distribution is demonstrated below:

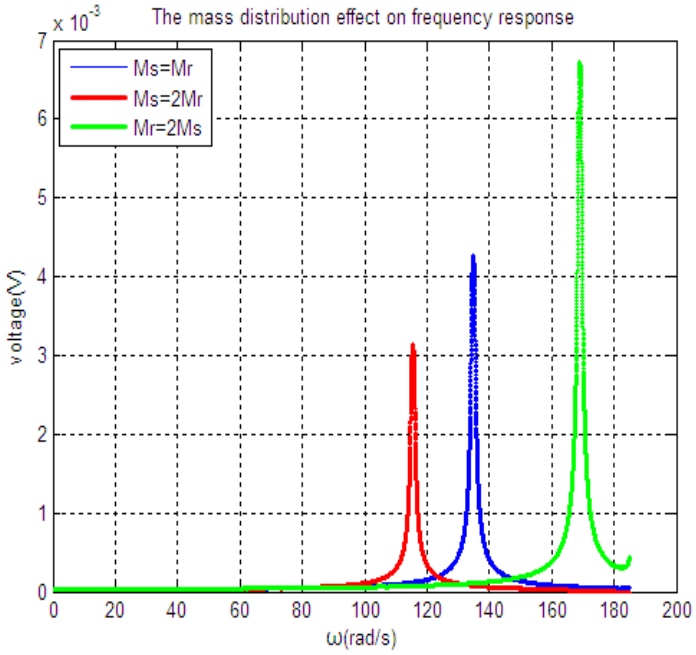

Figure 58. The effect of load mass distribution on frequency response of one degree of freedom electromagnetic rotary energy harvester

Above figure illustrates that increasing the mass distribution on fixed magnet and the body part of the speaker (M_r) will result in both higher resonant frequency and higher voltage peak.

4.3. Experimental test of one degree of freedom rotating harvester

To demonstrate how much voltage can be collected by this one degree of freedom system, the experimental setup was going to be tested with the geometric and material parameters of the bimorph cantilever which are given in the following table.

Table 4. Characteristics of the experimental beam-mass system

Parameters	Beam
Material	Spring steel
Young's modulus, E (GN/m2)	210
Length, L (mm)	61
Width, b (mm)	38.1

Thickness, t (mm)	0.5
Mass density, ρ (kg/m^3)	7850
Load mass, M_L (kg)	0.022

To explain the experiment procedure, the experimental setup should be tested in diverse angular velocities. Since the induced voltage through voice coil is sinusoidal, to obtain its Fourier transform, the maximum induced voltage in each frequency should be identified to obtain a point in frequency domain. Then with repeating this procedure for all frequencies, the frequency response of induced voltage within the voice coil will obtain by the curve fitting through all these points.

First, to identify the characteristics of this one degree of freedom system, the voice coil speaker has been placed on shaker and the base excitation response of this speaker is demonstrated in following figure:

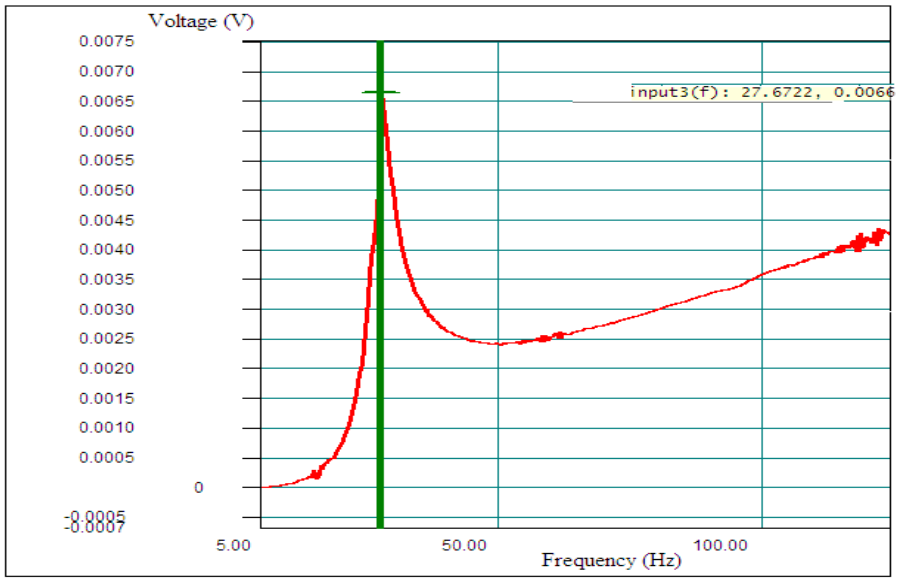

Figure 59. Frequency response of induced voltage - Experimental result for one degree of freedom system

Figure (59) illustrates that the resonance frequency of voice coil energy harvester occurs at 27.67 [Hz], but the maximum induced voltage is equal to 0.0066 [V], which is really negligible amount to harvest power on loads. Hence, on the next chapter, the two degrees of freedom system which comprises of linear voice coil motors are going to be

introduced since these linear voice coil motors are able to produce much higher voltages than voice coil speakers even in low frequencies.

4.4. Conclusion

The design of an electromagnetic energy harvester for rotary motion applications is discussed in this chapter. The electromagnetic energy harvester consists of a cantilever beam carrying a voice coil as tip mass, with the whole system mounted on a rotating horizontal hub. The proposed energy harvester has an inherent source of harmonic force due to the gravitational force of the tip mass. When the hub rotates with a constant angular speed, the gravity force on the tip and its coupling with rotational motion causes the mass-beam system to vibrate. A multimode mathematical model for the coupled electromechanical system is derived by using the method of assumed modes. Then the experimental analysis has been conducted to demonstrate how much voltage can be collected by this one degree of freedom system. Since the maximum induced voltage was really low (around 0.0066 [V]), thus the amount of harvesting power on loads is negligible. Therefore, in the next step, the two degrees of freedom system which comprises of linear voice coil motors are going to be introduced since these linear voice coil motors are able to produce much higher voltages than voice coil speakers even in low frequencies.

5. Two Degree of Freedom Electromagnetic Energy Harvester System for Rotary Motion

In this chapter, based on the design concepts of previous chapters, a system with two degree of freedom has been introduced. Then, this system has been placed on shaker to identify its characteristics to use it in rotary motion applications. Finally, this system has been mounted on a car ring to demonstrate the results experimentally.

5.1. Describing the Two Degree of Freedom Rotating Harvester System

The two degrees of freedom system is comprised of two linear voice coil motors which are connected to each other through a spring, called the connecting spring. As will be presented later in system identification, the stiffness of this connecting spring will determine the bandwidth of the frequency response of the system. Moreover, a small spring has been placed inside each of linear voice coil motors to make each voice coil to resonate. The schematic of the described system has been demonstrated in following figure. One of the most significant advantages of the two degrees of freedom system over one degree of freedom system is that the bandwidth of two degrees of freedom system, which can capture relatively high voltage, is much broader than one degree of freedom system. This important advantage enables us to harvest electrical power not only at a specific frequency, but also at wide range of car ring's speeds, which is going to be more practical in real world. In other words, adding one more degree of freedom to the electromagnetic rotary harvester will result in a generator which is less sensitive to a specific frequency.

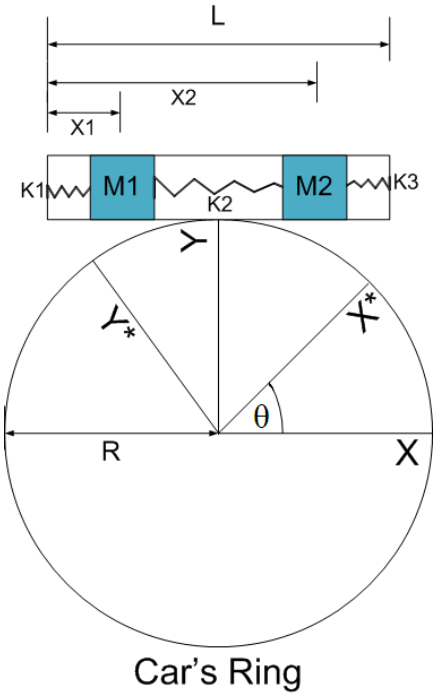

Figure 60. Two degrees of freedom system for harvesting energy from rotary motion application

5.2. System Identification of the Two Degree of Freedom Rotating Harvester

5.2.1. Governing Equations on Base Excitation Case

For system identification, it would be a good idea to analyze the system on base excitation case first. To do so, the general system has been considered based on Mass-Spring model and it has been excited from its base. The excitation equation is as follows:

$$Y = A \sin(\omega t) \tag{69}$$

where *A* and *ω* are the amplitude and angular frequency of the sinusoidal excitation, respectively. The base excitation equations are:

$$\begin{bmatrix} M_1 & 0 \\ 0 & M_2 \end{bmatrix}\begin{bmatrix} \ddot{X}_1 \\ \ddot{X}_2 \end{bmatrix}+\begin{bmatrix} (K_1+K_2) & -K_2 \\ -K_2 & (K_2+K_3) \end{bmatrix}\begin{bmatrix} X_1 \\ X_2 \end{bmatrix}=\begin{bmatrix} K_1.Y \\ 0 \end{bmatrix} \qquad (70)$$

where M_1 is the total mass of first coil (10.4 [gr]), M_2 is the total mass of second coil (9.9 [gr]), K_1 and K_3 are the spring constants of the small springs inside the linear voice coil motors, and K_2 is the spring constant of the connecting spring. At the next step, the experimental results for base excitation test among the effect of connecting spring stiffness on frequency response have been examined.

5.2.1.1. Examining the Two Degree of Freedom Rotating Harvester when the Connecting Spring is Soft

The setup has been placed on shaker to determine the frequency response of both coils. The shaker excitation was sinusoidal with 0.4 [mm] amplitude and the frequency sweeps from 5 to 300 [Hz]. The results are demonstrated below:

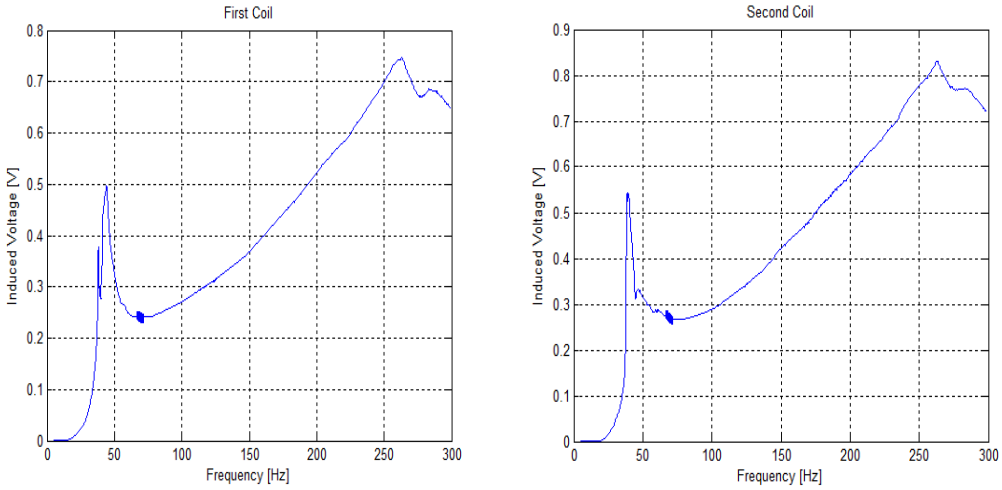

(a) (b)

Figure 61. The frequency responses of: (a) first linear voice coil motor, and (b) second linear voice coil motor; when the connecting spring is soft

For the first coil, the first peak happens at 42 [Hz] with 0.496 [V] amplitude and the second peak places at 263 [Hz] with 0.748 [V] amplitude, while for the second coil, the first peak happens at 42 [Hz] with 0.543[V] amplitude and the second peak occurs at

263 [Hz] with 0.832 [V] amplitude. Therefore, the bandwidth of the frequency response in this case is equal to 263-42 = 221 [Hz].

5.2.1.2. Examining the Two Degree of Freedom Rotating Harvester when the Connecting Spring is Stiff

The setup has been placed on shaker to determine the frequency response of both coils. The shaker excitation was sinusoidal with 0.4 [mm] amplitude and the frequency sweeps from 5 to 600 [Hz]. The results are demonstrated below:

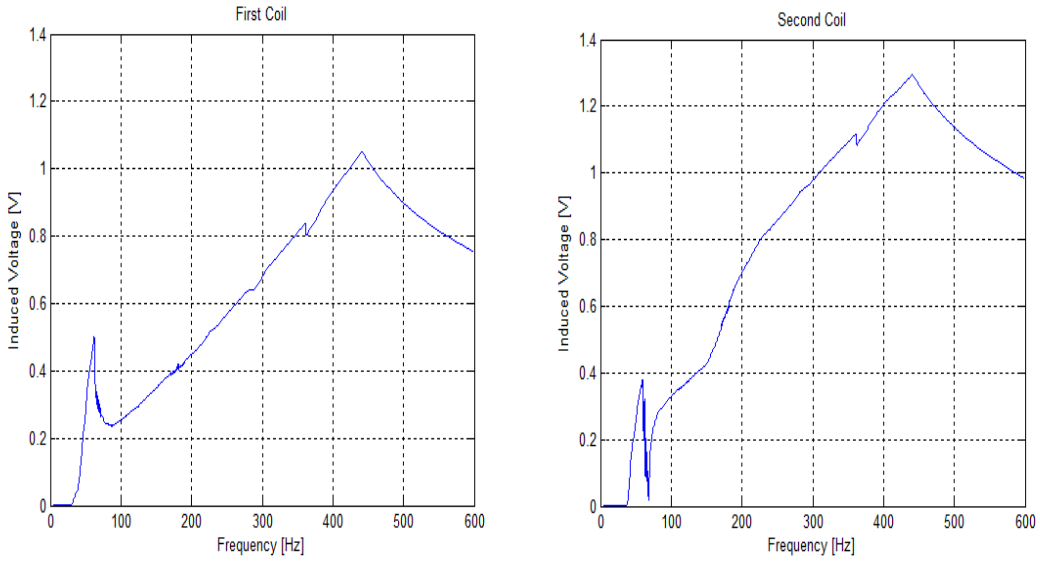

(a) (b)

Figure 62. The frequency responses of: (a) first linear voice coil motor, and (b) second linear voice coil motor; when the connecting spring is stiff

Again, for the first coil, the first peak happens at 58 [Hz] with 0.5 [V] amplitude and the second peak places at 445 [Hz] with 1.07 [V] amplitude, while for the second coil, the first peak happens at 58 [Hz] with 0.39[V] amplitude and the second peak occurs at 445 [Hz] with 1.3 [V] amplitude. This time, in this case, the bandwidth of the frequency response is equal to 445-58 = 387 [Hz], which is 166 [Hz] more than the previous case when connecting spring was softer. Thus, it can be concluded that the bandwidth can be increased by stiffer connecting spring.

5.3. Testing the two degree of freedom energy harvesting system on rotary application

5.3.1. The governing equations on rotary motion case

This section presents mathematical modeling of the two degrees of freedom energy harvester system which has been mounted on a rotary ring and consists of linear voice coil motors and springs. The ring rotates with a constant speed. Considering the effect of an electromagnetic induction, equations of motion are derived using the Lagrangian approach followed by relationships describing the harvested power. The equations provide a quantitative description of how the ring acceleration, gravity force, and relative displacement between permanent magnet and coil contribute power to the energy harvester. To derive the mathematical model, the energy harvester system has been analyzed from two different perspectives: mechanical perspective and electrical perspective. The mechanical perspective relates the ring's rotation to the relative displacement between coil and permanent magnet. The electrical perspective indicates the amount of induced voltage and harvested power in the moving coil. Since in the electrical perspective, the same governing equations as the electrical subsystem model of one degree of freedom system rule, thus in this section, only the coupled dynamic equations of the rotating ring have been derived and equation (68) can also be used for calculating the amount of induced voltage across moving coils in this two degrees of freedom system. To derive a mathematical model that describes the energy harvester system, the Lagrangian formulation has been used, which has been mentioned here again for the convenience:

$$\frac{d}{dt}\left(\frac{\partial T}{\partial \dot{p}_i}\right) - \frac{\partial T}{\partial p_i} + \frac{\partial U}{\partial p_i} = F_i \qquad (71)$$

where *T* is the total kinetic energy, *U* is the total potential energy, F_i is the *ith* generalized force, and p_i is the *ith* generalized coordinate. The generalized force vector is given by $\mathrm{F} = \begin{bmatrix} 0 & 0 & 0 \end{bmatrix}^T$ and the generalized coordinate vector is chosen as $\mathrm{p} = \begin{bmatrix} \theta & X_1 & X_2 \end{bmatrix}^T$, where θ is the angular displacement of car's ring, X_1 is the

displacement for the spring inside the first linear voice coil motor with the constant K_1 ,and X_2 is the displacement for the spring inside the second linear voice coil motor with the constant K_2.

To obtain the total kinetic energy of the energy harvester system, first we need to calculate the kinetic energy of different components of the system. For the electromagnetic part, which consists of two linear voice coil motors, the kinetic energy is comprised of translational and rotational components, therefore:

$$T_{Translational} = \frac{1}{2} m_1 \left[\left(\dot{X}_1 + R\dot{\theta} \right)^2 + \left(X_1 - \frac{L}{2} \right)^2 \dot{\theta}^2 \right] + \frac{1}{2} m_2 \left[\left(\dot{X}_2 + R\dot{\theta} \right)^2 + \left(X_2 - \frac{L}{2} \right)^2 \dot{\theta}^2 \right] \quad (72)$$

$$T_{rotational} = \frac{1}{2} \left(J_1 + J_2 \right) \dot{\theta}^2 \quad (73)$$

where *R* is the car's ring radius, *L* is the total length of the energy harvester setup, which is equal to 12 [cm], m_1 and m_2 are the total masses of the first coil and the second coil, respectively, and finally J_1 and J_2 are the inertia of the first coil and the second coil, respectively. The total kinetic energy of the harvester system is equal to the summation of these two kinetic energies, which means:

$$T_{Total} = T_{Translational} + T_{rotational} \quad (74)$$

The expression for the total potential energy (*U*) is as follows:

$$U = m_1 g \left[R\sin\theta - \left(\frac{L}{2} - X_1 \right) \cos\theta \right] + m_2 g \left[R\sin\theta - \left(\frac{L}{2} - X_2 \right) \cos\theta \right] + \frac{1}{2} K_1 X_1^{\,2} + \frac{1}{2} K_2 (X_2 - X_1)^2 + \frac{1}{2} K_3 X_2^{\,2} \quad (75)$$

5.3.2. *Numerical analysis of two degree of freedom rotating harvester*

This section presents numerical results to evaluate again the feasibility of the two degrees of freedom energy harvesting system for the rotary motion applications. By solving equations (74), (75), and (68) from last chapter simultaneously for variable X_1, the simulation result is as follows:

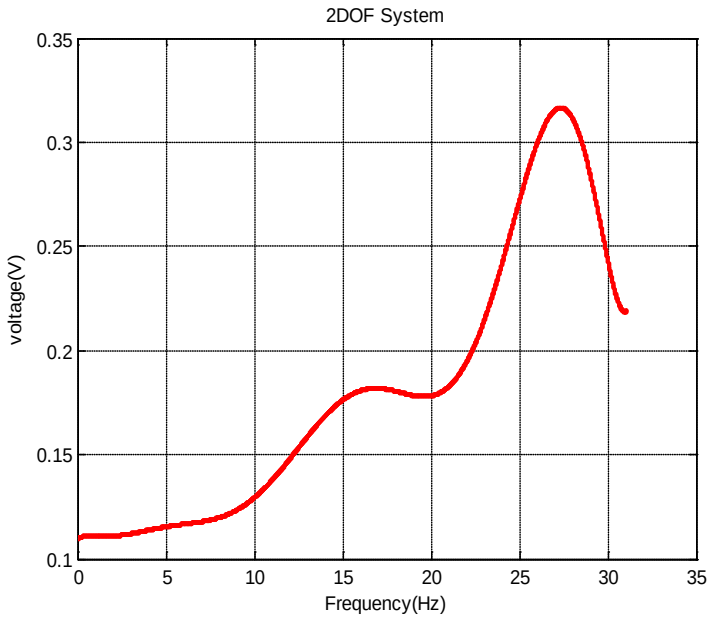

Figure 63. Simulation result for two degrees of freedom system

This figure illustrates that the two degrees of freedom system has two peaks; the first one occurs at 16 [Hz] with the amplitude 0.18 [V] and the second one is at 27 [Hz] with the amplitude 0.315 [V].

Then to obtain the numerical graph of harvested power through this two degree of freedom system, again equation (44) has been used and the result is as follows:

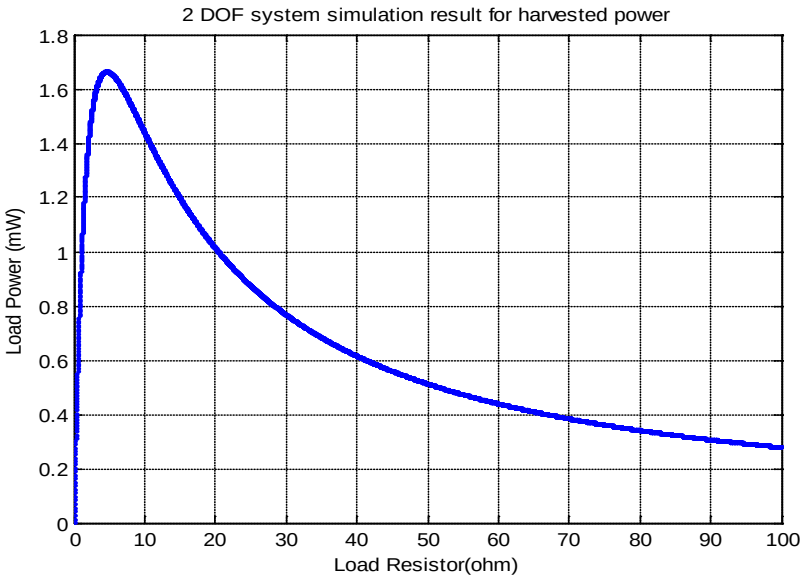

Figure 64. Simulation result of harvested power for two degrees of freedom system

Based on figure (64), the maximum expected harvested power from this two degree of freedom system is around 1.66 [mW] when the load resistor is equal to 4.6 [Ω].

Now, it is time to put the energy harvester setup on the car's ring and run the experimental test.

5.3.3. Experimental result of two degree of freedom rotating harvester

The two degrees of freedom system, which has been explained in section 5.1, has been placed on a car's ring to experiment the energy harvesting system on a rotary application. The general schematic of this experimental setup has been illustrated in figure (65). Due to limitations of electric motor which rotates the ring, rotary speeds more than 120 (rad/s) or 19 (Hz) cannot be reached. Therefore, to decrease the resonance frequency of linear voice coil motors, a longer and softer spring has been used inside the linear voice coil motors. On the other hand, since these springs are longer than the ones used before, the distance between the coil and the magnet is increased. Thus, the maximum induced voltage in former case was higher than the recent one. To describe

the experiment procedure, the experimental setup has been tested on diverse angular velocities. Since the induced voltage through energy harvesting system is sinusoidal, to obtain its Fourier transform, the maximum induced voltage in each frequency has been identified to obtain a point in frequency domain. Then the best curve is fitted through these points to indicate the frequency response of induced voltage within voice coil.

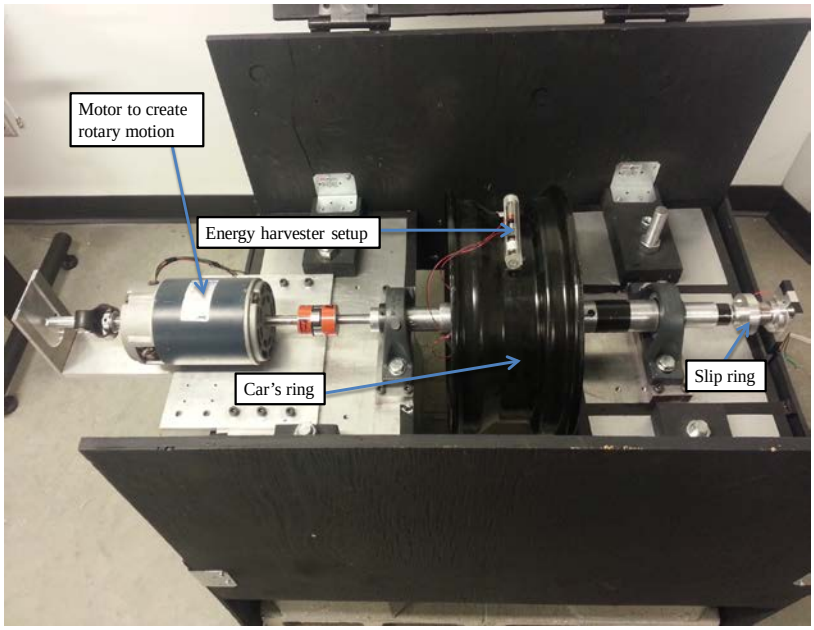

(a)

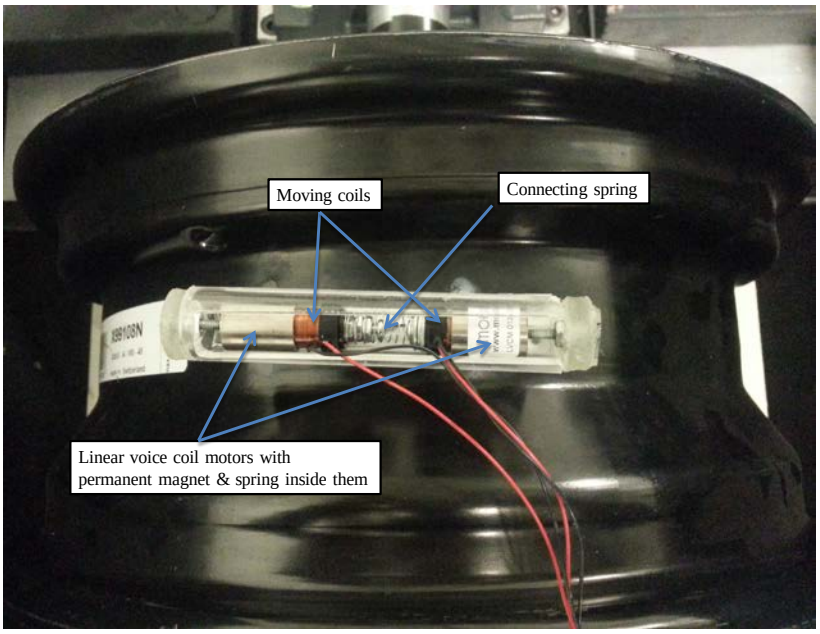

(b)

Figure 65. The schematic of the experimental setup for two degrees of freedom system: (a) the general setup; (b) details of energy harvester components

Repeating this procedure for all frequencies, the frequency response of induced voltage is obtained as follows:

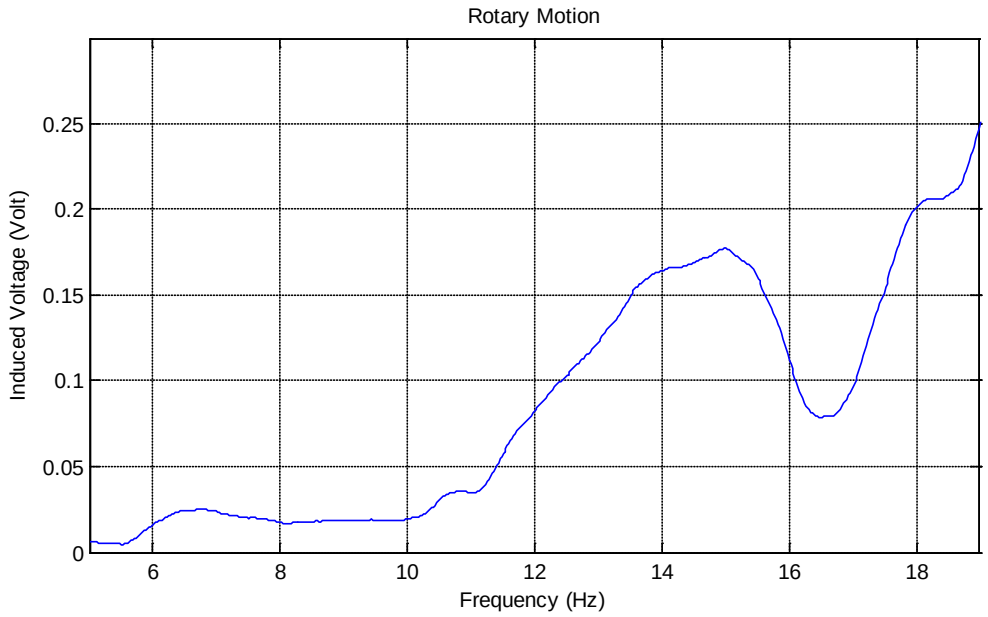

Figure 66. Frequency response of induced voltage - Experimental result

Figure (66) illustrates that the resonance frequency of energy harvester occurs at 15 (Hz), and the induced voltage's peak is equal to 0.175 Volt. Again it should be mentioned that the second voltage peak which occurs at higher rotational speeds cannot be reached due to limitations of experimental setup.

6. Conclusion

Energy harvesting converts the unused ambient energy in the environment into electricity. Numerous potential sources for power harvesting exist such as light, thermal gradient, and vibration (motion). In this thesis, both linear and rotary motions are used as a power source. Three types of vibration motion to electricity converters have been considered so far: electromagnetic, piezoelectric, and electrostatic. After a preliminary investigation and comparison, electromagnetic method was chosen to be applied as an energy harvester for both linear and rotary motion applications.

In the electromagnetic converter, the relative motion between a coil and magnetic field causes an induced voltage in the coil. After deriving the governing equations on the modified voice coil electromagnetic energy harvester, the new design has been introduced and the parameter study on diverse components of energy harvester setup has been conducted. In this parameter study, the effects of three design modifications on induced voltage and harvested power have been examined through simulation analysis and it has been demonstrated that applying those three design modifications will improve the amount of induced voltage by %50. In this simulation analysis, a pattern for the magnetic flux density lines has been illustrated and the result indicates that the magnetic field is well concentrated on the coil area, thus this setup is able to capture and convert most of the available kinetic energy into electricity. After simulation analysis, this newly designed energy harvester setup has been fabricated to verify simulation results experimentally. For linear motion application, the experimental results indicate that when the coil movements' speed is 70 [mm/s], the maximum harvested power through impedance matching with coil's internal resistance is 5.320 [mW]. The next step in this research area is to use a spring in the electromagnetic energy harvester for linear motions to make the system resonate and tune the resonance frequency of energy harvester system to the natural frequency of vibration source to maximize the harvesting power.

For rotary motion application, when one degree of freedom system such as voice coil speaker is used, the resonance frequency occurs in relatively high frequencies, which are not achievable in many rotary applications, therefore it has been tried to reduce the resonance frequency of the speaker. But since in lower resonance frequencies, the maximum induced voltage has decreased dramatically, thus in next step, the two degrees of freedom energy harvesting system for rotary motion applications has been introduced. Although the resonance frequency of the two degrees of freedom system was still relatively high, but since the induced voltage across the moving coils in this system was relatively higher than one degree of freedom system, hence when the resonance frequency has been reduced by adding additional masses and decreasing the stiffness of springs, this two degrees of freedom system still has produced reasonable amount of voltage in low frequencies. This two degrees of freedom system is comprised of two linear voice coil motors which are connected to each other through a spring, called the connecting spring. The stiffness of this connecting spring will determine the bandwidth of the frequency response of the system. Moreover, a small spring has been placed inside each of linear voice coil motors to make each voice coil to resonate. This system has been mounted on a car ring to demonstrate the amount of reachable induced voltage by this system experimentally. The result illustrated that at the resonant frequency (15 [Hz]), the induced voltage was 0.175 [V] for each coil. Therefore, if these two coils have been connected to each other as series voltage sources, the total induced voltage across two degrees of freedom system is 0.35 [V]. Note that since in this two degree of freedom system, the second voltage peak which occurs at higher rotational speeds cannot be reached due to limitations of experimental setup, therefore the next step in this research area could be to decrease the resonance frequencies of the system more than the current implemented setup in order to use both voltage peaks and hence more bandwidth of the two degree of freedom electromagnetic rotating harvester.

References

[1] Amirtharajah, R., and Chandrakasan, A. P., 1998, “Self-powered signal processing using vibration-based power generation”, IEEE J. Solid State Circuits 33, pp. 687-695.

[2] Koeneman P B, Busche-Vishniac I J, Wood K L, 1997, “Feasibility of micro power supplies for MEMS”, *IEEE J.* Microelectomechanical Systems 6, 355-362.

[3] Jacobson S A, Epstein A H, 2003, “An informal survey of power MEMS”, Proc. The Int. Symp. on Micro-Mechanical Engineering (ISMME), Japan, K18.

[4] Koeneman P B, Busche-Vishniac I J and Wood K L 1997, Feasibility of micro power supplies for MEMS *IEEE J. Microelectomech. Syst.* **6** 355–62

[5] G¨orge G, Kirstein M and Erbel R 2001, Microgenerators for energy autarkic pacemakers and defibrillators: fact or fiction *Herz* **26** 64–8

[6] Jacobson S A and Epstein A H 2003, An informal survey of power MEMS *Proc. Int. Symp. on Micro-Mechanical Engineering ISMME (Japan)* p K18

[7] Banazwski B and Shah R K 2003, The role of fuel cells for consumer electronic products and toys *Proc. 1st Int. Conf. on Fuel Cell Science, Engineering and Technology (Rochester, NY, USA)* pp 149–55

[8] Epstein A H 2004, Millimeter-scale, micro-electro-mechanical systems gas turbine engines *J. Eng. Gas Turbines Power* **126** 205–26

[9] Tanaka S, Changa K-S, Mina K-B, Satoh D, Yoshida K and Esashi M 2004, MEMS-based components of a miniature fuel cell/fuel reformer system *Chem. Eng. J.* **101** 143–9

[10] Kiely J J, Morgan D V and Rowe D M 1991, Low cost miniature thermoelectric generator *Electron. Lett.* **27** 2332–4

[11] Schaevitz S B, Franz A J, Jensen K F and Schmidt M A 2001, A combustion-based MEMS thermoelectric power generator *Proc. 11th Int. Conf. on Solid-State Sensors and Actuators, Transducers 01 (Munich, Germany)* p 1A3-02

[12] Zhang C, Najafi K, Bernal L P and Washabaugh P D 2001, An integrated combustor-thermoelectric micro power generator *Proc. 11th Int. Conf. on Solid-State Sensors and Actuators, Transducers 01 (Munich, Germany)* p 1A3–03

[13] Erick O. Torres and Gabriel A. Rincon-Mora, Harvesting ambient energy, http://users.ece.gatech.edu/rincon-mora/publicat/trade_jrnls/ee_times_0805_harvest.pdf

[14] Shad Roudy, Paul K. Wright and Kristofer Pister, Micro-electrostatic vibration-to-electricity converters, Proceedings of IMECE2002,ASME International Mechanical Engineering Congress & Exposition, November 17-22, 2002

[15] Meninger S 1999, A low power controller for a MEMS based energy converter, *MSc* Massachusetts Institute of Technology

[16] Roundy S, Wright P and Pister K 2002, Micro-electrostatic vibration-to-electricity converters, *Proc. IMECE 2002* pp 1–10

[17] Roundy S 2003, Energy scavenging for wireless sensor nodes with a focus on vibration to electricity conversion, *PhD Thesis* University of California, Berkeley

[18] Meninger S, Mur-Miranda J, Lang J, Chandrakasan A, Slocum A, Schmidt M and Amirtharajah R 2001, Vibration to electric energy conversion, *IEEE Trans Very Large Scale Integration (VLSI) Syst.* **9** 64–76

[19] Despesse G, Jager T, Chaillout J, Leger J, Vassilev A, Basrour S and Chalot B 2005, Fabrication and characterisation of high damping electrostatic micro devices for vibration energy scavenging, *Proc. Design, Test, Integration and Packaging of MEMS and MOEMS* pp 386–90

[20] Miyazaki M, Tanaka H, Ono G, Nagano T, Ohkubo N, Kawahara T and Yano K 2003, Electric-energy generation using variable-capacitive resonator for power-free LSI: efficiency analysis and fundamental experiment, *ISLPED '03* pp 193–8

[21] Sterken T, Baert K, Puers R and Borghs S, Power extraction from ambient vibration, *Proc. 3rd Workshop on Semiconductor Sensors and Actuators* pp 680–3

[22] Sterken T, Fiorini P, Baert K, Borghs G and Puers R 2004, Novel design and fabrication of a MEMS electrostatic vibration scavenger, *Power MEMS Conference (Kyoto Japan)* pp 18–21

[23] Arakawa Y, Suzuki Y and Kasagi N 2004, Micro seismic power generator using electret polymer film, *Power MEMS Conference (Kyoto, Japan)* pp 187–90

[24] Peano F and Tambosso T 2005, Design and optimisation of a MEMS electret-based capacitive energy scavenger, *J. Microelectromech. Syst.* **14** 435–529

[25] Erick O. Torres and Gabriel A. Rincon-Mora, Harvesting ambient energy will make embedded devices autonomous, http://www.embedded.com/showArticle.jhtml?articleID=170102227

[26] Nye J F 1957, *Physical Properties of Crystals* (Oxford: Oxford University Press)

[27] Baudry H 1987, Screen-printing piezoelectric devices, *Proc. 6th European Microelectronics Conference (London, UK),* pp 456–63

[28] White N M and Turner J D 1997, Thick-film sensors: past, present and future, *Meas. Sci. Technol.* **8** 1–20

[29] Lovinger A J 1983, Ferroelectric polymers, *Science* **220** 1115–21

[30] S P Beeby, M J Tudor, and N M White 2006, Energy harvesting vibration sources for microsystems applications, Measurement Science and Technology.17, R175-R195

[31] Shad Roudy and Paul Wright, 2002, A piezoelectric vibration based generator for wireless electronics, Smart Materials and Structures, Volume 13, pp.1131-1144

[32] Umeda M, Nakamura K and Ueha S 1996, Analysis of the transformation of mechanical impact energy to electric energy using piezoelectric vibrator, *Japan. J. Appl. Phys.* **35** 3267–73

[33] Kymissis J, Kendall C, Paradiso J and Gershenfeld N 1998, Parasitic power harvesting in shoes, *Proc. 2nd IEEE Int. Conf. Wearable Computing (California)* pp 132–9

[34] White N M, Glynne-Jones P and Beeby S P 2001, A novel thick-film piezoelectric micro-generator, *Smart Mater. Struct.* **10** 850–2

[35] Glynne-Jones P, Beeby S P and White N M 2001, Towards a piezoelectric vibration powered microgenerator, *IEE Proc.—Sci. Meas. Technol.* **148** 68–72

[36] Glynne-Jones P, Beeby S P and White N M 2001, The modelling of a piezoelectric vibration powered generator for Microsystems, *Proc. 11th Int. Conf. on Solid-State Sensors and Actuators, Transducers 01 (Munich, Germany)* pp 46–9

[37] Beeby S P, Blackburn A and White N M 1999, Processing of PZT piezoelectric thick films on silicon for microelectromechanical systems, *J. Micromech. Microeng.* **9** 218–29

[38] Torah R, Beeby S and White N 2005, An improved thick-film piezoelectric material by powder blending and enhanced processing parameters, *IEEE Trans. UFFC* **52** 10–16

[39] Jeon Y B, Sood R, Jeong J-h and Kim S G 2005, MEMS power generator with transverse mode thin film PZT, *Sensors Actuators* A **122** 16–22

[40] Sodano H A, Park G, Leo D J and Inman D J 2003, Use of piezoelectric energy harvesting devices for charging batteries, *Proc. SPIE 10th Annual Int. Symp. on Smart Structures and Materials (San Diego, CA, USA)* pp 101–8

[41] Sodano H A, Park G and Inman D J 2003, An investigation into the performance of macro-fiber composites for sensing and structural vibration application, *Mech. Syst. Signal Process.* **18** 683–97

[42] Wilkie W K, Bryant R G, High J W, Fox R L, Hellbaum R F, Jalink A, Little B D and Mirick P H 2000, Low cost piezocomposite actuator for structural control applications, *Proc. 7th SPIE Int. Symp. on Smart Structures and Materials (Newport Beach, CA)* pp 323–34

[43] Gorge G, Kirstein M and Erbel R 2001, Microgenerators for energy autarkic pacemakers and defibrillators: fact or fiction *Herz.*

[44] Shad Roudy PhD thesis, May 2003, Energy scavenging for wireless sensor nodes with a focus on vibration to electricity conversion, University of California at Berkeley, Berkeley CA

[45] Roundy, S., Wright, P. K., and Rabaye, J., 2003, "A study of low level vibrations as a power source for wireless sensor nodes", Computer Communications 26, pp. 1131-1144

[46] Glynne-Jones, P., Tudor, M.J., Beeby, S.P., and White, N.M., 2004, "An electromagnetic, vibration-powered generator for intelligent sensor systems", Sens. Actuators A110(1-3), pp. 344-349

[47] Von Buren, T., and Troster, G., 2007, "Design and optimisation of a linear vibration-driven electromagnetic micro-power generator", Sens. Actuators A 135, pp. 765-775

[48] Williams, C.B., and Yates, R.B., 1995, "Analysis of a micro-electric generator for microsystems", Transducers 95/Eurosensors IX, pp. 369-372

[49] Hadas Z, Kluge M, Singule V, Ondrusek C, 2007, "Electromagnetic vibration power generator", IEEE Int Symp Diagnostics for Electric Machines, Power Electronics and Drives: 451-455

[50] Bayrashev A, Robbins W P and Ziaie B 2004, Low frequency wireless powering of microsystrems using piezoelectric-magnetostrictive laminate composites, *Sensors Actuators* A **114** 244–9

[51] Jiles, David, 1991, Introduction to Magnetism and Magnetic Materials, Chapman and Hall, Chap. 1

[52] Franklin, Jerrold, 2005, Classical Electromagnetism, Pearson Addison Wesley, Chap. 3

[53] Lorrain, Paul, and Corson, Dale R., 1990, Electromagnetism: Principles and Applications, W. H. Freeman and company, Chap. 5

[54] Coey, J. M. D., 2010, Magnetism and Magnetic Materials, Cambridge University Press, Chap. 4

[55] Cheng, D. K., 1989, Field and Wave Electromagnetics, second edition, Addison-Wesley publishing company,Chap. 7

[56] Ida, Nathan, and Bastos, Joao, 1997, Electromagnetics and Calculation of Fields, second edition, Springer, Chap. 5

[57] Di Bartolo, Baldassare, 2004, Classical Theory of Electromagnetism, second edition, World Scientific, Chap. 2

[58] Knoepfel, Heinz, 2000, Magnetic Fields: a comprehensive theoretical treatise for practical use, Wiley-Interscience, John Wiley & sons, Inc., Chap. 1

[59] http://www.kjmagnetics.com/proddetail.asp?prod=RX8CC

[60] Khameneifar, F., and Arzanpour, S., 2008, “Energy Harvesting From Pneumatic Tires Using Piezoelectric Transducers,” ASME Conference Proceedings of SMASIS 2008, Paper No. 426, pp. 333–339